Department of Electrical and Computer Engineering

Wireless Information and Power Transfer in Beyond 5G IoT Networks

Eleni Goudeli

A Dissertation

Submitted in Partial Fulfillment of the

Requirements for the Degree of

Doctor of Philosophy

at the University of Cyprus

September, 2022

APPROVAL PAGE

Eleni Goudeli

Wireless Information and Power Transfer

in Beyond 5G IoT Networks

The present Doctorate Dissertation was submitted in partial fulfillment of the requirements for the Degree of Doctor of Philosophy in the Department of Electrical and Computer Engineering, and was approved on September 2, 2022 by the members of the Examination Committee.

Committee Chair _____
Prof. Georgios Ellinas

Research Supervisor _____
Prof. Ioannis Krikidis

Committee Member _____
Prof. Stelios Timotheou

Committee Member _____
Prof. Ghassan Kraidy

Committee Member _____
Prof. Vasos Vassiliou

DECLARATION OF DOCTORAL CANDIDATE

The present doctoral dissertation was submitted in partial fulfillment of the requirements for the degree of Doctor of Philosophy of the University of Cyprus. It is a product of original work of my own, unless otherwise mentioned through the references, notes, or any other statements.

.....[Full Name of Doctoral Candidate]

.....[Signature]

Περίληψη

Στη νέα εποχή του διαδικτύου των πραγμάτων και των ασύρματων δικτύων αισθητήρων, η ασύρματη μεταφορά ισχύος (ΑΜΙ) έχει αναγνωριστεί ως μια πολλά υποσχόμενη τεχνολογία για να ξεπεραστεί η κρίσιμη πρόκληση της εξ αποστάσεως και ασύρματης παροχής ενέργειας, σε ένα μεγάλο αριθμό συσκευών χαμηλής ισχύος. Συγκεκριμένα, τα σήματα ραδιοσυχνοτήτων θεωρούνται κατάλληλα για ΑΜΙ, επειδή έχουν την ικανότητα να ενεργοποιούν συσκευές σε μεγάλη απόσταση, ενώ χρησιμοποιούνται επίσης για ασύρματη μετάδοση πληροφοριών (ΑΜΠ). Αυτή η διατριβή ασχολείται με τεχνικές χαμηλής πολυπλοκότητας, που εφαρμόζονται σε τεχνολογίες όπως η οπισθοσκέδαση και η ταυτόχρονη ΑΜΙ και ΑΜΠ (ΑΜΙΠ), με στόχο τη βελτίωση της απόδοσης του συστήματος.

Ως εκ τούτου, πέρα από τα παραδοσιακά συστήματα επικοινωνίας οπισθοσκέδασης, προτείνουμε μια τοπολογία πολλαπλών κεραιών και μελετάμε εξελιγμένες τεχνικές χωρικής διαμόρφωσης, αξιοποιώντας τον χώρο και τον χρόνο για τη μετάδοση πληροφοριών. Επιπλέον, για την τεχνολογία ΑΜΙΠ μελετάμε τεχνικές χαμηλής πολυπλοκότητας για την ανίχνευση πληροφορίας και αποθήκευση ενέργειας, με διάφορες αρχιτεκτονικές. Συγκεκριμένα, διερευνούμε την αρχιτεκτονική του δέκτη και της ετικέτας οπισθοσκέδασης, μαζί με το κύκλωμα ανόρθωσης, τα μοντέλα αποκωδικοποίησης πληροφορίας και τα μοντέλα αποθήκευσης ενέργειας, ως μέσα για περαιτέρω βελτίωση της απόδοσης.

Οι προτεινόμενες λύσεις στοχεύουν τη βελτίωση των συστημάτων όσον αφορά το ποσοστό σφάλματος αποκωδικοποίησης και αποθήκευσης ενέργειας. Συγκεκριμένα, οι προτεινόμενες τοπολογίες χρησιμοποιούν εργαλεία από τη θεωρία επεξεργασίας σήματος, παρέχοντας μετρήσεις, όρια και ασυμπτωτικά αποτελέσματα. Έπειτα από την απαραίτητη ανάλυση, επιλέγουμε κρίσιμες παραμέτρους του συστήματος που επηρεάζουν τις επιδόσεις, όπως ο αριθμός των κεραιών, η ισχύς μετάδοσης, το σχήμα διαμόρφωσης που υιοθετείται, καθώς και η γνώση του καναλιού στην πλευρά του δέκτη.

Abstract

In the new era of the Internet of Things (IoT) and wireless sensor networks, wireless power transfer (WPT) has been recognized as a promising technology to overcome the critical challenge of supplying power, remotely and wirelessly, to an extensive number of low-power IoT devices. Specifically, radio-frequency (RF) signals are considered as a viable source for WPT, since they have the ability to energize devices over a long distance, while are also used for wireless information transmission (WIT). This thesis deals with low-complexity information and power transfer techniques, applied over wireless information and power transfer (WIPT) technologies, such as backscatter and simultaneous WIPT (SWIPT), targeting to enhance the system's performance.

As such, over traditional backscatter communication systems, we study a multiple antenna topology and propose sophisticated spatial-modulation based techniques, exploiting space and time domain for transmitting information. Furthermore, for SWIPT technology we study low-complexity energy detection schemes and propose solutions for an integrated SWIPT architecture. In this direction, we investigate the receiver's and backscatter tag's (BT) architecture, along with the rectifying circuits, decoding and energy harvesting (EH) models adopted, as means for further performance gains.

The proposed frameworks are provided to capture the systems' enhancement in terms of error rate and EH. Specifically, the proposed topologies utilize tools from communication and signal processing theory, providing metrics, bounds and asymptotical results for a thorough performance analysis. Through the analysis, we draw insights about critical system parameters that affect the performance, such as the number of antennas/rectennas, the transmit power, the modulation scheme applied and the knowledge of the channel state information (CSI) at the receiver's side.

Acknowledgments

This Ph.D. dissertation was performed under the supervision of Dr. Ioannis Krikidis, Associate Professor in the Department of Electrical and Computer Engineering at the University of Cyprus. I would like to express my deepest gratitude to my supervisor for giving me the opportunity to join his team, study and work on his side. His professional and wise guidance during my doctoral studies, was essential in achieving the goals of this thesis. Most of all, I would like to thank him for believing in me.

My special thanks goes to Dr. Constantinos Psomas for his valuable guidance and scientific insights during our collaboration. His forward thinking, positive disposition and consistent encouragement made this thesis possible. Moreover, I would like to thank all my committee members and especially Prof. Georgios Ellinas and Assist. Prof. Stelios Timotheou for their time to review and handle this Ph.D. dissertation.

I am also grateful to the administrative staff at the department of Electrical and Computer Engineering, Skevi Ioannou and Vasiliki Mousikou-Dimitriou, for their precious help and encouragement.

Last but not least, I would like to deeply thank and devote this thesis, to my beloved family for their unconditional love. Sharing this journey of Ph.D with them, was really demanding and challenging. Through their constant motivation, I managed to be passionate and confident about my research work. The completion of this dissertation would not have been possible without my husband's generous support and my children's smiles.

Publications

Published journal publications

1. E. Goudeli, C. Psomas, and I. Krikidis, "Spatial-modulation-based techniques for backscatter communication systems," *IEEE Internet of Things Journal* , vol. 7, no. 10, pp. 10623-10634, October 2020.

2. E. Goudeli, C. Psomas, and I. Krikidis, "A detection scheme for integrated SWIPT receivers with rectenna arrays," *IEEE Transactions on Green Communications and Networking*, May 2022.

Published conference proceedings

1. E. Goudeli, C. Psomas, and I. Krikidis, "Sequential decoding for simultaneous wireless information and power transfer," in *Proc. of International Conference on Telecommunications (ICT)*, Limassol, Cyprus, May 2017.

2. E. Goudeli, C. Psomas, and I. Krikidis, "An integrated SWIPT receiver using non-coherent detection schemes," in *Proc. of IEEE Global Communications Conference (GLOBECOM)*, Abu Dhabi, United Arab Emirates, December 2018.

3. E. Goudeli, C. Psomas, I. Krikidis, H. Kiani, D. Chatzichristodoulou, and S. Nikolaou, "Detection schemes for integrated SWIPT receivers with non-linear energy harvesting," in *Proc. of IEEE Vehicular Technology Conference*, Helsinki, Finland, 2022.

4. E. Goudeli, C. Psomas, and I. Krikidis, "SWIPT with diplexer-based multiple-antenna rectification," in *Proc. of IEEE International Mediterranean Conference on Communications and Networking (MeditCom)*, Athens, Greece, September 2022.

Contents

List of Figures

List of Tables

List of Abbreviations

3GPP	3rd generation partnership project
4G	Fourth generation
5G	Fifth generation
ADC	Analog-to digital converter
AM	Amplitude modulation
AR	Augmented reality
AS	Antenna switching
ASK	Amplitude shift keying
AWGN	Additive white Gaussian noise
BackCom	Backscatter communications
B5G	Beyond 5G
BPAM	Bipolar pulse amplitude modulation
BPSK	Binary phase shift keying
BT	Backscatter tag
CDF	Cumulative distribution function
CLC	Constant-linear-constant
CoR	Cooperative Relay
CSI	Channel state information
CW	Continuous wave
D2D	Device-to-device
DBC	Dyadic backscatter channel
DC	Direct current

DPS	Dynamically power splitting
EH	Energy harvesting
EM	Electromagnetic
EMG	Exponentially modified Gaussian
FAS	Fluid antenna system
FM	Frequency modulation
FS	Frequency splitting
FSK	Frequency shift keying
GFSK	Gaussian frequency shift keying
GHz	Gigahertz
GLRT-MLSD	Generalized likelihood ratio test-maximum likelihood sequence detection
GSC	Generalized selection combining
GSM	Generalized spatial modulation
GSMA	Generalized spatial modulation with Alamouti
IMT	International mobile telecommunications
ID	Information decoding
IoT	Internet of things
IRS	Intelligent reconfigurable surface
ITU-R	International telecommunication union radio communication sector
kHz	Kilohertz
LPF	Low pass filter
	LoS Line of sight
MHz	Megahertz
MIMO	Multiple-input multiple-output
MISO	Multiple-input single-output
ML	Maximum-likelihood

NOMA	Non-orthogonal multiple access
NLoS	Non-Line of sight
mmWave	Millimeter wave
OOK	On-off keying
OPS	Optimized symbol by symbol detection with sensitivity
OSBS	Optimized symbol by symbol detection
OSTBC	Orthogonal space-time coding
QAM	Quadrature amplitude modulation
QoS	Quality of service
QPSK	Quadrature phase shift keying
PAM	Pulse amplitude modulation
PAPR	Peak to average power ratio
pdf	Probability density function
PEM	Pulse energy modulation
PEP	Pairwise error probability
PPM	Pulse position modulation
PSK	Phase shift keying
RF	Radio frequency
RFID	Radio frequency identification
RN	Reader Node
SBS	Symbol by symbol
SDMA	Space division multiple access
SIC	Successive interference cancellation
SER	Symbol error rate
SM	Spatial modulation
SNR	Signal to noise ratio
SIMO	Single-input multiple-output
SISO	Single-input single-output

SS- ST	Selective store strategy
SWIPT	Simultaneous wireless information and power transfer
TDMA	Time division multiple access
TS	Time switching
WIPT	Wireless information and power transfer
WIT	Wireless information transfer
WPCN	Wireless powered communication network
WPT	Wireless power transfer

Chapter 1

Thesis Motivation and Contribution

In this thesis, we focus our interest on B5G IoT networks, due to the expected massive deployment of low power and sensor networks. Specifically, we recognize the importance of wireless information and power transfer (WIPT) in such networks and investigate how low-complexity information and power techniques, can be adopted in simultaneous WIPT (SWIPT) and backscatter communication (BackCom) solutions, in order to succeed enhanced information decoding (ID) and energy harvesting (EH).

1.1 Introduction

The current generation of cellular systems, referred to as the fifth Generation (5G) is undoubtedly more than just a new generation of wireless communications. It represents a fundamental change in the mobile ecosystem, unleashing a combination of enhanced speed, expanded bandwidth, low latency, and increased power efficiency. In particular, it is anticipated that 5G networks will connect at least 100 billion devices worldwide with approximately 7.6 billion mobile subscribers due to the tremendous popularity of smartphones, laptops, sensors, etc. [1].

It is evident that 5G spurs innovation across many industries and provides a platform enabling emergent technologies such as the IoT. In fact, the 3rd generation partnership project (3GPP) has incorporated IoT characteristics into the 5G specifications, confirming their long term status as part of future 5G standards [2]. Fig. 1.1 presents the key capabilities of International Mobile Telecommunications (IMT) Advanced standard (4th generation) compared to IMT-2020 (5th generation), according

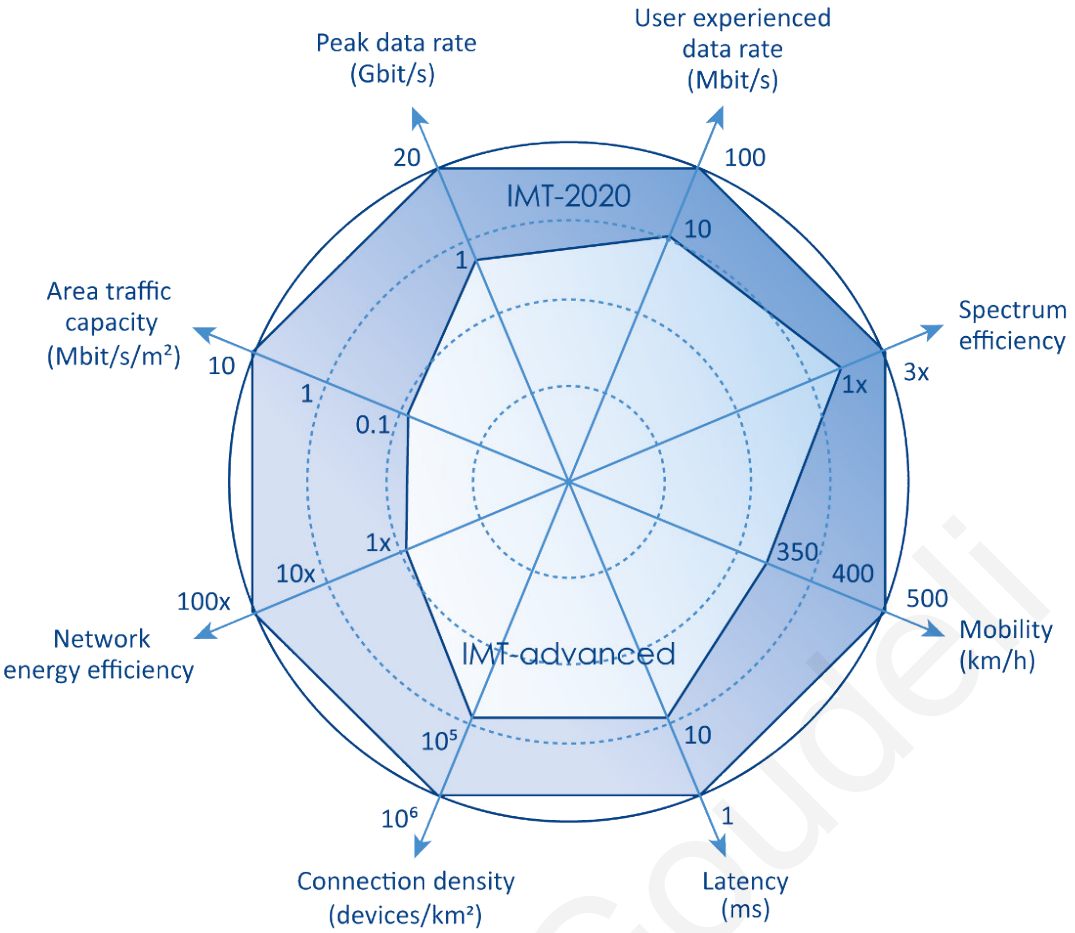

Figure 1.1: Key capabilities of IMT-Advanced compared to IMT-2020 according to ITU-R.

to International Telecommunication Union Radiocommunication Sector (ITU-R).

As seen in Fig. 1.1, 5G networks provide, among other targets, 1000 times larger mobile data volume per area, 10 to 100 times higher user data rate, and serve 10 to 100 times more connected devices than 4G cellular systems. However, the initial network deployments do not use all the capabilities currently defined for 5G IoT. While the optimization of networks and early 5G devices is an ongoing process, researchers have initiated discussions on what comes B5G IoT and leads to the next generation of wireless communications.

In the new era of B5G IoT, in order to fulfill the requirements of communication networks, various disruptive techniques, such as non-orthogonal multiple access (NOMA) [3], millimetre wave (mmWave) communications [4], and mobile-edge computing [5], have been proposed in the literature. On top of this, advanced signal processing algorithms have been developed to improve the energy efficiency of communication systems. Nevertheless, despite the potential system throughput

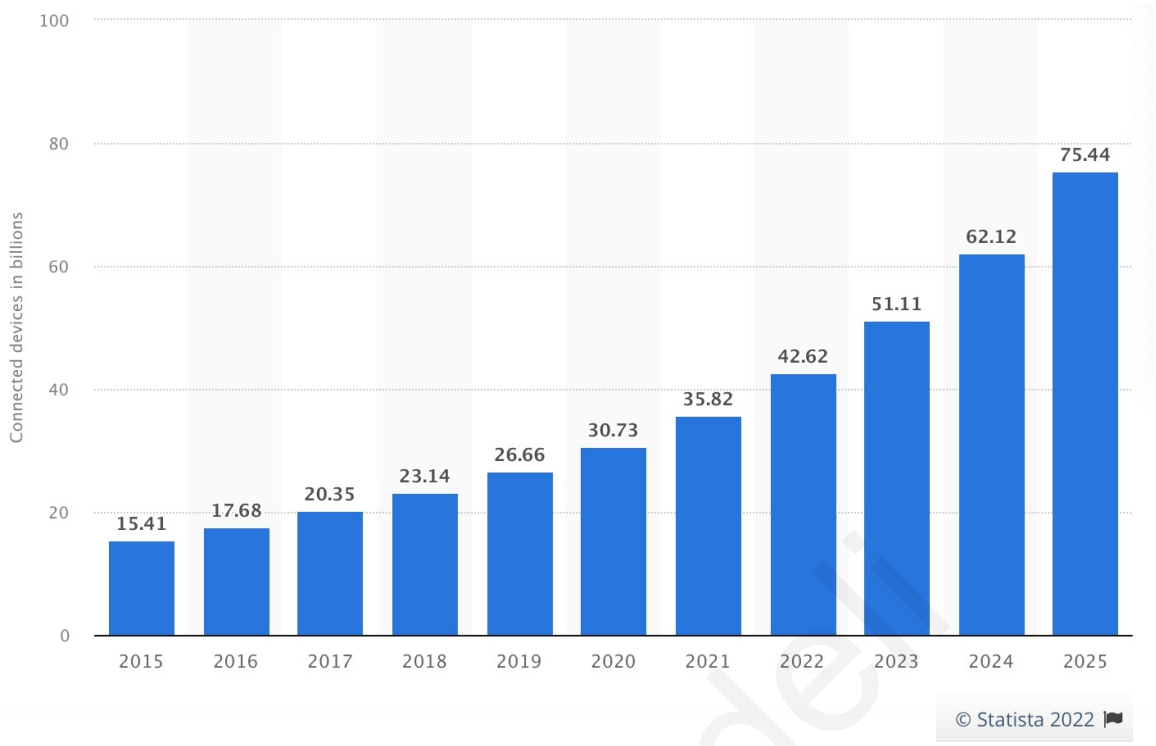

Figure 1.2: IoT connected devices installed base worldwide from 2015 to 2025 (in billions).

improvements and the reductions in consumed energy brought by these techniques, energy-limited communication devices with short life span still create a system performance bottleneck.

More specifically, from statistical point of view, in the following years we are expecting worldwide, billions of IoT connected devices (see Fig. 1.2). These small wireless sensor modules will be unobtrusively and invisibly integrated into clothing, walls, and vehicles at locations which are inaccessible for wired/manual recharging. Furthermore, battery-powered wireless communication devices have limited energy storage capacity and their frequent replacement can be costly or even impossible, which creates a serious performance barrier for realizing reliable and ubiquitous wireless communication networks.

A promising approach to prolong the lifetime of traditional wireless communication systems is to enable the wireless communication devices harvest energy from the environment. These energy sources can be easily accessed without any costs. In the context of wireless sensors, the use of solar cells for harvesting energy from the environment is a mature technique and is the most common mechanism used for prolonging the lifetime of the power supply [6], [7]. However solar power is uncon-

trollable, and the conversion efficiency is affected by the day-night cycle, seasonal changes, weather conditions, and temperature. On the other hand, electromagentic (EM) signals, between 3 kilohertz (kHz) and 300 gigahertz (GHz) of frequency spectrum, can be converted into electrical energy with the help of an antenna and a rectifier circuit, while are constantly present even throughout the night. As such, wireless power transfer (WPT), as a harvesting technology where the nodes charge their batteries from EM radiation, is nowadays one of the most widely used and favorable technology for facilitating efficient and sustainable communication networks, while serving energy-limited communication devices [8] - [10]. In Chapter 2, we delve into WPT and EH sources, with more details.

1.2 Motivation and Research Objectives

Motivated from the above, in the new era of wireless sensor networks, there is a critical need to cover energy sustainability for B5G IoT networks. At the same time, we need to take into consideration the ability for information flow in these networks. Therefore, radio-frequency (RF) WPT has been recognized as a promising technology to overcome not only the critical challenge of supplying power, remotely and wirelessly, to an extensive number of low-power IoT devices, but also to be used for wireless information transmission (WIT). RF signals are considered as a viable source for WPT and WIT, since they have the ability to energize low-power devices over a long distance and transfer information, at the same time.

Motivated by this, we co-design solutions for WIPT, targeting enhanced performance in terms of ID and EH, for B5G IoT networks. In order to achieve this, we herein identify the key technologies of WIPT and several of their system design parameters, that have high impact on the performance of WIPT and should be carefully chosen in order to optimize ID and EH.

1.2.1 Key Technologies of WIPT

WIPT can be categorized into three different types, as seen in Fig.1.3.

Simultaneous WIPT (SWIPT): Regarding the SWIPT concept, Varshney first proposed the idea of transmitting information and energy simultaneously in [11]. The term was coined in [12] and refers to scenarios where information and power are

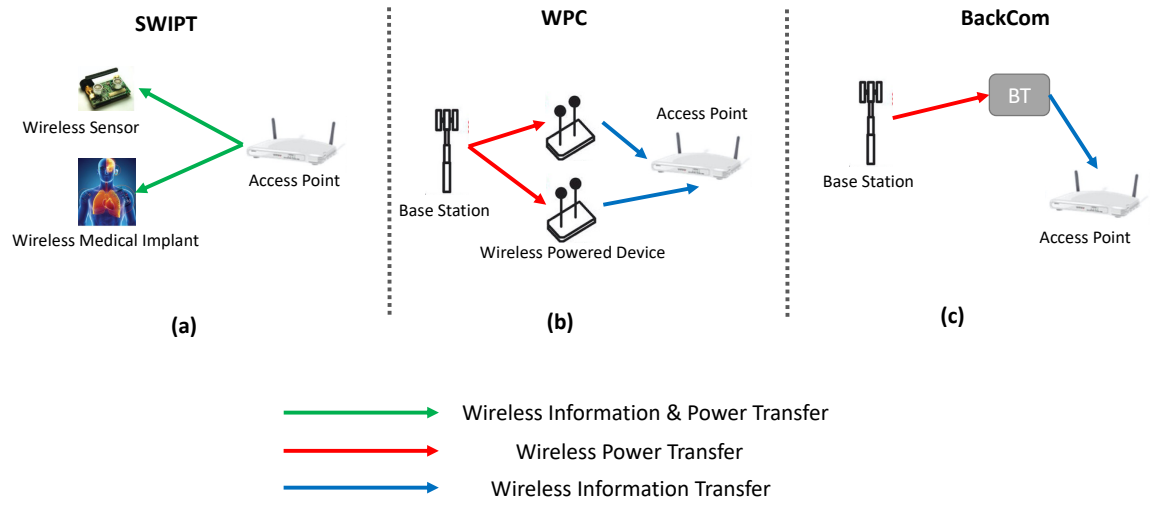

Figure 1.3: Key technologies for WIPT.

simultaneously sent from the transmitter(s) to the receiver(s) [13]. The information receiver(s) and energy harvester(s) can be collocated or separated as in Fig. 1.3 (a). With collocated receivers, a single (typically low-power) device equipped with an information receiver and energy harvester, simultaneously harvests energy and receives/transmits data. With separate receivers, these two operations are in different devices, with EH being processed by a low-power device being wirelessly powered and information receiver being a device receiving data.

Wirelessly Powered Communication Networks (WPCNs): Energy is transmitted in the downlink from a base station to a device, and information is transmitted in the uplink [14]. The device harvests energy in the downlink and uses the harvested energy to transmit data in the uplink. As seen in Fig. 1.3 (b), wireless-powered devices first harvest energy, either from a dedicated power station or from ambient RF signals, and then exploit the harvested energy to transmit information signals.

Wirelessly Powered Backscatter Communication (BackCom): As seen in Fig. 1.3 (c), the downlink is used to transmit energy to a device, and the uplink is used to transmit information using backscatter modulation from a backscatter tag (BT) to a reader node (RN), e.g. an access point, by reflecting and modulating the incoming RF signal [15]. BTs do not require oscillators to generate carrier signals, and power consumption can be decreased by several orders of magnitude compared to conventional wireless communications [16].

Moreover, a network could have a mixture of all of these types of transmissions with multiple collocated and/or distributed energy and information transmitter(s).

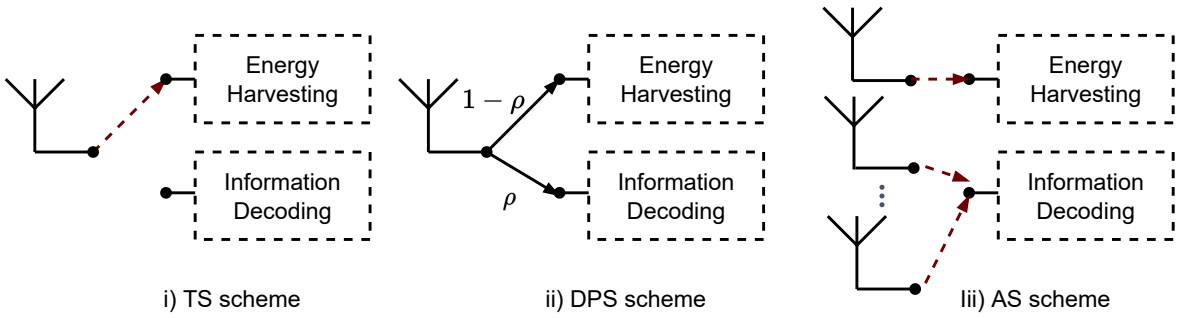

Figure 1.4: SWIPT architecture for separated receiver.

Among the different types of WIPT and its many indicated challenges, this dissertation focuses on the potential of SWIPT and BackCom, in B5G IoT networks.

1.2.2 Architectures of SWIPT

In practice, existing RF-based EH circuits harvest the energy of the received signal directly in the RF domain. In fact, the EH process destroys the modulated information (e.g., phase-embedded information) in the signal. In addition, conventional ID is performed in the digital baseband and the frequency down-converted signals cannot be used for EH. Despite the continuous advances in SWIPT technology, till recently in the literature of RF circuits, it was impossible to perform SWIPT from the same received signal by using one antenna [17]. As such, SWIPT was achieved through a separated receiver in time, power or spatial domain, where the received RF signal is split for ID and EH [18] or with the use of an integrated architecture. Recently, a scheme which achieves SWIPT without the split of the resources with the use of a diplexer at the receiver's side was proposed [19].

Separated receiver: Most studies in literature use the structure of a separated receiver. Specifically, since ID and EH cannot be performed on the same received signal, practical implementations split the received signal in two parts, where one part is used for information transfer and another part is used for power transfer. This signal split can be performed in time, power or spatial domain, as shown in Fig. 1.4. More details about time switching (TS), dynamically power splitting (DPS) and antenna switching (AS) schemes, are given in Appendix A.1.

Integrated receiver: In [20], a different type of SWIPT receiver, was introduced, characterized as integrated. The difference lies in that the ID and the EH circuits are integrated, as shown in Fig. 1.5. Specifically, the RF to baseband conversion

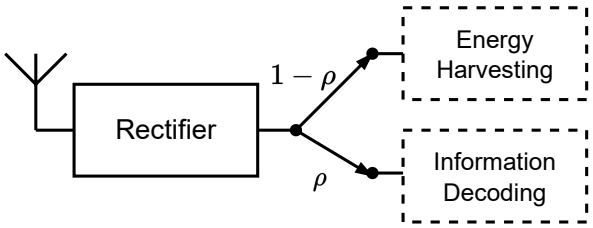

Figure 1.5: SWIPT architecture for integrated receiver.

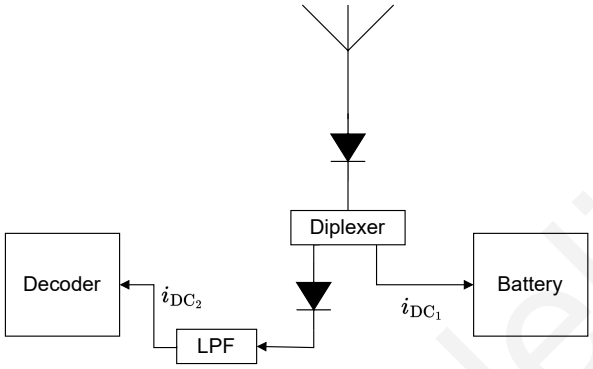

Figure 1.6: SWIPT architecture for diplexer-based receiver.

is replaced by a rectifying antenna (rectenna), which receives and converts the RF signal to direct current (DC) power that is used both for EH and ID. Taking into consideration that the rectification circuit and the low-pass filter (LPF) are passive devices, the energy consumption for the information decoder is really small. Thus, ID and EH cannot only be achieved by the same signal, but also result in a higher EH.

Diplexer-based receiver: Diplexers are passive devices that implement frequency-domain multiplexing. In particular, their ports are frequency-selective, while reversing their input and output, can be used for separating higher from lower frequency signals, at one receive antenna. As such, with the proposed circuit, as shown in Fig. 1.6 there is no need for a power splitter, since the low-pass band-pass diplexer allows the dual and continuous use of the same signal for SWIPT. More details about this architecture are given in Appendix A.2.

Targeting an enhanced performance in terms of ID and EH, this thesis focuses on the study of the integrated SWIPT receiver, where the conversion from RF to baseband has been replaced from a passive rectifier and LPF. Furthermore, the novel diplexer-based receiver is studied, where SWIPT is achieved without splitting the signal either in the RF or the DC domain.

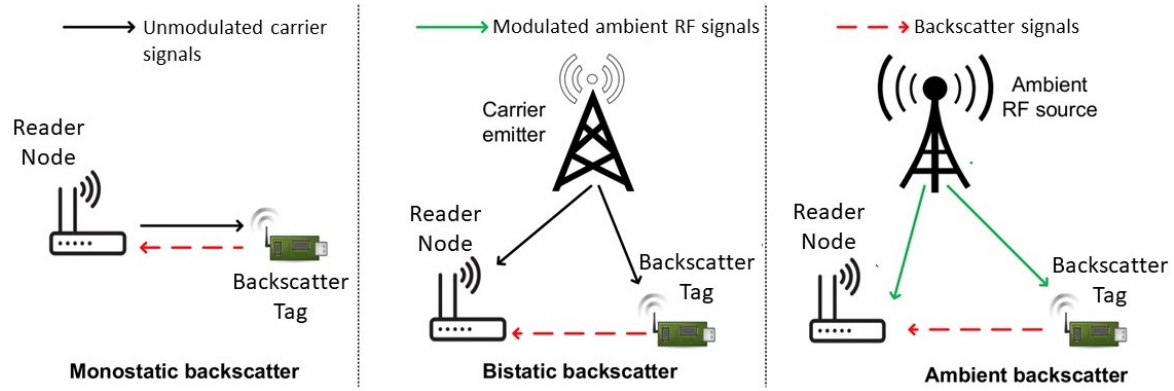

Figure 1.7: Backscatter architectures.

1.2.3 Architectures of Backscatter Communications

ff BackCom systems can be clasified into three major types based on their architecture: monostatic, bistatic and ambient BackCom systems [21].

Monostatic BackCom: In this architecture e.g. a RF identification (RFID) system, there are two main components: a BT and a RN as shown in Fig. 1.7. The RN consists of, in the same device, an RF source and a backscatter receiver. The RF source generates RF signals to activate the BT. Then, the BT modulates and reflects the RF signals sent from the RF source to transmit its data to the backscatter receiver. As the RF source and the backscatter receiver are placed on the same device, i.e., the RN, the modulated signals may suffer from a round-trip path loss [22], while the near-far problem may be one of this architecture's limitations. In addition, in case where the BT is located far from the RN, due to signal loss from the RF source, it experiences higher energy outage probability and degradation of the received modulated backscatter signal strength [23]. Thus, this architecture is mainly adopted for short-range RFID applications.

Bistatic BackCom: Conversely from monostatic BackCom, in the bistatic BackCom, the RF source, i.e., the carrier emitter, and the backscatter receiver are separated as shown in Fig. 1.7. As such, with this architecture we avoid the round-trip path loss. Additionally, the performance can be improved dramatically by placing the carrier emitter at an optimal location. Specifically, one centralized RN can be located in the field while multiple carrier emitters are well placed around BTs. Moreover, the doubly near-far problem can be mitigated as BTs can derive unmodulated RF signals sent from nearby carrier emitters to harvest energy and backscatter data [24]. Although carrier emitters are bulky and their deployment is costly, the manufac-

turing cost for carrier emitters and RNs of bistatic BackCom is cheaper than that of monostatic BackCom due to the simple design of the components [25].

Ambient BackCom: Similar to bistatic BackCom, carrier emitters in ambient architecture, are also separated from RNs. Different from bistatic BackCom, carrier emitters in ambient BackCom, are available ambient RF sources, e.g. TV towers and cellular base stations, instead of using dedicated RF sources. As a result, the ambient architecture has some advantages compared to the bistatic one. Firstly, there is no need to deploy and maintain dedicated RF sources, thereby reducing the cost. Secondly, by utilizing existing RF signals, there is no need to allocate new frequency spectrum [26]. However, because of using modulated ambient signals, there are some disadvantages. Modulated ambient RF signals are unpredictable, dynamic and opportunistic, acting as a direct interference to RNs, which largely limits the performance [27].

Motivated by the above, in this thesis we investigate BackCom with the use of a bistatic architecture. Specifically, this architecture is more appropriate, since we consider multiple antennas at the BT, in order to apply physical layer techniques and achieve enhanced ID. As such, the devoted RF sources are necessary for securing the uninterrupted power of the BT.

1.2.4 EH Model

To enable RF-based EH at a wireless communication receiver, a rectenna is usually deployed for the conversion of EM energy into DC signal. In practice, various rectifier technologies (Schottky diodes, complementary metal oxide semiconductors, backward tunnel diodes e.t.c.) and topologies (single and multiple diodes) are used. In general, an accurate EH model can be obtained by deriving mathematical equations to describe the input-output characteristic of an EH circuit based on its schematic. However, this might lead to complicated expressions which are intractable for performance analysis. In this section we present the most common EH models used in the literature.

Most previous studies on SWIPT systems assumed an ideal **linear energy harvester** [28], [20], [29], in which the RF-to-DC power conversion efficiency is modeled as a fixed constant independent of the input power. This was the most utilized model up to recent years and did not take into consideration harvester's sensitivity

and saturation levels. It is a single parameter model, where the harvested power is linearly increased with the input power. The input-output relation of this model is given by

$$P_{\mathrm{DC}} = \zeta P_{\mathrm{RF}}, \tag{1.1}$$

where P_{DC} is the output harvested DC power, P_{RF} is the RF power received by the antenna, and ζ is a constant power conversion efficiency that is less than 1. The linear EH model is simple allowing for further analysis of WPT systems, while avoiding complicated or intractable analysis for more sophisticated nonlinear EH models.

On the other hand, the rectifier circuit implemented with one or multiple diodes, imposes strong non-linearity on the power conversion. Considering the nonlinear rectification process (diode turn-on/reverse breakdown voltages, diode non-linearity, and saturation effects), the harvested power cannot be simply predicted by the conventional linear model. Thus, the power conversion efficiency is a function of not only the input power (e.g., the squared amplitude of the sine-wave), but also the shape of the input signal (e.g., the phase of the sine-wave). To address the nonlinear characteristics and to improve accuracy, **nonlinear EH models** are proposed in the literature and presented in Appendix A.3.

In this thesis, taking into consideration the analytical tractability and the fact that we do not consider the EH model for transmit signal design, we use the linear and piece-wise linear EH models.

1.2.5 Channel State Information

Wireless communications have witnessed several major theoretical advancements in the last few decades, although the baseband receiver design, has been based on a coherent detection, which has been adopted exclusively in nearly all the popular wireless communication standards. Such a solution relies on the availability of channel state information (CSI) at the receiver, resulting to a coherent decoding scheme. The coherent receiver design has stayed virtually unchanged throughout the evolution of wireless communication systems to date.

Coherent scheme: Coherent techniques are a challenging task, since the source needs to periodically send training symbols, which incurs an increased signaling overhead and processing burden [30]. In WPT systems, CSI at the receiver is not

needed since the received RF signal is directly converted to a DC signal without any signal processing [31]. However, it is worth mentioning that CSI at the receiver may be required if the transmit signal also conveys information WIPT. Especially for the EH receivers, the conventional methods for channel estimation in wireless communications [32] may not be directly applicable due to the energy and hardware limitations of EH receivers. To tackle this issue, there have been various channel acquisition methods that have been proposed for multi-antenna WPT systems [33]-[37]. However, regarding the BackCom coherent detection may be adopted especially in the bistatic architecture, since the RF sources are most of the time devoted transmitters, that may set no restrictions to communication range and at the same time increase the bit rate [38].

Non-coherent scheme: On the other hand, with the use of non-coherent techniques, the receiver's complexity is reduced at the expense of a decreased spectral efficiency. Taking into consideration though, their low-cost and low-power consumption, it makes them attractive for systems such as B5G networks. A work on SWIPT with the use of integrated receiver is presented in [39], where precoding on the energy patterns is used to overcome the non-coherent detection problem. In [41], authors study a splitting receiver, which involves joint processing of coherently and non-coherently received signals. Regarding the BackCom networks, non- coherent detection is mainly adopted in ambient backscatter communications [42], where the knowledge of CSI at the RN is a challenging task.

1.2.6 Multiple Antennas

Multiple-input multiple-output (MIMO) have largely been studied in the past years, especially for 5G networks. MIMO antennas exploit the spatial diversity of the propagation channel to increase the robustness or the throughput of the wireless communication link. Additionally, it was shown in [43] that 5G MIMO antenna can provide large benefits for low-power IoT devices. To this end, MIMO techniques are also studied in SWIPT and BackCom.

In the state-of-the-art, multiple antenna system models are traditionally considered as a common solution for enhanced performance either in terms of ID or EH. There are various studies conducted for exclusively EH technologies, trying to overcome the need of providing enough energy for a reliable EH operation [44], [45].

In addition, in the communication and signal processing literature, it is proven that multiple antenna systems demonstrate a great improvement of performance in terms of spectral efficiency and higher data rates, succeeding diversity or multiplexing gains [46]- [48]. Likewise, SWIPT has also been an area of research for attracting interest on multiple antennas. Specifically, in [49] the authors study a two-way relay system with multiple users and a multi-antenna relay employing SWIPT strategy, where splitting the received signal leads to a rate-energy trade-off. In [50], authors investigate SWIPT with a multi-antenna transmitter sending data and energy to single antenna receivers adopting a time switching circuit. Beamforming for energy transfer and information transmission is considered in [51], achieving the maximal energy efficiency.

Additionally, MIMO technology embeds various antennas either at the receiver, the BT or at both of them, when we are referring to BackCom. The multiple antenna tag channel was first studied in [52], providing details for the behavior of the MIMO RFID channel. Numerous studies in literature prove the added value of multiple antennas in a BackCom system, providing enhanced performance in terms of spectral efficiency, bit rate and error probability [53]. Specifically, in [54], an orthogonal space-time coding scheme (OSTBC) was studied, proving that when employed and implemented in a MIMO RFID scenario, full diversity may be achieved. At the same time, with the advances in printed antennas and RF micro-electronic technologies [55], multiple antennas can be integrated successfully into a device, while keeping the hardware cost low. It has to be noted, that the hardware request for a multiple antenna BT is currently a mature technology in terms of theoretical analysis and hardware implementation [56]. In addition, [57] showed that exists a space-time code for MIMO backscatter channels which not only reduces the tag circuit complexity considerably but also does not degrade the performance.

From this section, we note that the performance of WIPT is clearly affected and depends from the architecture design, the number of adopted antennas, the adopted EH model, as also the detection scheme based on CSI. **In this thesis, we are motivated to study several aspects of these points, in order to achieve enhanced performance in terms of ID and EH, upon SWIPT and BackCom proposed solutions.**

Table 1.1: Summary of techniques, schemes and detection methods.

Chapter	Technology	EH model	Receive Antennas	CSI
3	Integrated SWIPT	Linear	Single	Non-coherent
4	Integrated SWIPT	Pice-wise Linear	Multiple	Non-coherent
5	Bistatic BackCom	-	Multiple	Coherent
6	SWIPT with Diplexers	Linear	Multiple	Non-coherent

1.3 Thesis Outline

In particular, we focus on leveraging tools and techniques from communication theory, in order to provide solutions, that will result to enhanced performance both in terms of ID and EH. In Table 1.1, we summarize the different techniques, schemes and detection methods that are adopted in this thesis. The outline of the thesis, along with the publications supporting the contributions, is as follows.

In Chapter 2, we provide a foundation knowledge of WIPT, along with the background and state-of-the-art for the studied technologies and applied techniques.

The first technical part (Chapter 3) of the thesis, focuses on the integrated SWIPT receiver architecture and investigates a non-coherent detection that avoids signaling overhead and training complexity. A point-to-point system model is adopted, considering a linear EH model. A sophisticated sequential decoder is proposed which is based on the generalized likelihood ratio test-maximum likelihood sequence detection. With the use of Viterbi-type trellis-search algorithm, the proposed technique achieves decreased computational complexity in comparison to conventional sequential detection approaches. The content of this chapter is based on:

- E. Goudeli, C. Psomas, and I. Krikidis, "Sequential decoding for simultaneous wireless information and power transfer," in *Proc. of International Conference on Telecommunications (ICT)*, Limassol, Cyprus, May 2017.

- E. Goudeli, C. Psomas, and I. Krikidis, "An integrated SWIPT receiver using non-coherent detection schemes," in *Proc. of IEEE Global Communications Conference (GLOBECOM)*, Abu Dhabi, United Arab Emirates, December 2018.

The second technical part (Chapter 4), proposes a new rectenna architecture that employs multiple antenna elements with an appropriate combining (RF or DC combining) and processing. The proposed techniques overcome the saturation effect that limits the performance of conventional rectenna circuits, while non-coherent

energy detection is achieved. The new architecture is evaluated in terms of both ID and EH performance, by utilizing probability theory tools. The content of this chapter is based on:

- E. Goudeli, C. Psomas, I. Krikidis, H. Kiani, D. Chatzichristodoulou, and S. Nikolaou, "Detection schemes for integrated SWIPT receivers with non-linear energy harvesting," in *Proc. of IEEE Vehicular Technology Conference*, Helsinki, Finland, 2022.

- E. Goudeli, C. Psomas, and I. Krikidis, "A detection scheme for integrated SWIPT receivers with rectenna arrays," *IEEE Transactions on Green Communications and Networking*, May 2022.

In the third technical part (Chapter 5), a solution for multiple-antenna backscatter communications is studied. With the use of sophisticated physical layer tools (i.e., spatial-modulation, space-time coding), the proposed solution succeeds array gain as well as transmit diversity. The proposed technique is analyzed in terms of pairwise error probability while simple asymptotic results are derived. The content of this chapter is based on:

- E. Goudeli, C. Psomas, and I. Krikidis, "Spatial-modulation-based techniques for backscatter communication systems," *IEEE Internet of Things Journal* , vol. 7, no. 10, pp. 10623-10634, October 2020.

The fourth technical part of this thesis (Chapter 6), studies SWIPT by considering a diplexer-based receiver with multiple antennas. Specifically, with the use of multiple diplexers at the receiver side, SWIPT is achieved without splitting the received signal in the DC domain. A non-coherent detection is also proposed that provides enhanced performance in terms of both ID and EH. The content of this chapter is based on:

- E. Goudeli, C. Psomas, and I. Krikidis, "SWIPT with diplexer-based multiple-antenna rectification," in *Proc. of IEEE International Mediterranean Conference on Communications and Networking (MeditCom)*, Athens, Greece, September 2022.

Finally, in **Chapter 7**, we conclude this work and discuss possible directions for future works.

1.4 Thesis Contributions

This thesis deals with sophisticated low-complexity information and power transfer techniques, applied over WIPT technologies, such as backscatter and SWIPT. By adopting tools from communication theory and statistical signal processing, the thesis investigates WIPT solutions that achieve enhanced performance in terms of both ID and EH. The work is novel, important and timely for the design of B5G IoT networks. The main contributions of the thesis can be summarized as follows.

The thesis:

- Investigates a new single-rectenna SWIPT architecture that employs non-coherent information decoder at the output of the integrated receiver. By exploiting the coherence time of the wireless channel, a novel sequential decoder is proposed, which reduces the complexity of conventional counterparts and overcomes error floor phenomena.

- A SWIPT architecture consisting of multiple rectennas is also investigated. By exploiting two different combining schemes at the receiver's side, one in the DC domain and the other in the RF domain, a jointly enhanced ID and EH performance is achieved. The proposed architecture overcomes saturation effects and is appropriate for scenarios with high received energy. Simulation results along with theoretical analysis, illustrate that both schemes enhance the performance, while DC combining scheme outperforms RF. Special cases with reduced computation complexity are also investigated, providing fundamental performance bounds.

- Studies an innovative diplexer-based multiple-rectenna scheme that achieves SWIPT without splitting/orthogonalizing the received signal into ID/EH branches. An associated non-coherent energy detection is also proposed to reduce information transfer complexity and avoid channel state information. The proposed solution outperforms conventional integrated SWIPT receiver.

- Designs a backscatter communication system with multiple antennas at the backscatter tag. By using sophisticated physical-layer tools such as spatial modulation and space-time coding (i.e. Alamouti), the proposed scheme enhances the overall efficiency of the backscatter communication system and

ensures diversity and array gains. Analytical and asymptotic expressions are derived related to the pairwise error probability and the associated diversity gains, respectively.

Overall, this thesis is an important contribution to the fields of WIPT. The proposed solutions on the key technologies of SWIPT and backscatter, along with the sophisticated techniques applied and the thorough performance analysis that is provided, play an important role in the design of future B5G IoT networks.

Herein we provide a summary of the main notation used throughout this thesis.

Main Notation: $||x||$ denotes the Euclidean norm of $x \in \mathbb{C}$, $\hat{x}$ denotes the estimation of variable x, while $Q(x) = \frac{1}{\sqrt{2\pi}} \int_x^\infty \exp(-\frac{u^2}{2}) du$ denotes the Q-function and σ_x^2 denotes the variance of the variable x. Furthermore, $\mathfrak{R}\{x\}$ and $\mathfrak{I}\{x\}$ denote the real and imaginary parts of variable x, respectively, while with x^*, we denote the complex conjugate of x. We also use $\binom{n}{k}$, $\lfloor . \rfloor$ and $\lceil . \rceil$, for the binomial coefficient, the floor and the ceiling function of x, respectively. In addition, bold lower case letters are vectors, $\mathbb{E}[x]$ represents the expected value of x and $\lfloor x \rfloor_{2^p}$ is used in order to denote the largest integer less than or equal to x, that is an integer power of 2.

Chapter 2

Background and State-of-the-art

WIPT has been recognized as one of the promising technologies for handling the explosive growth of IoT in B5G networks. RF waves have traditionally been used for WIT or wireless communications. However, radio waves carry both energy and information. Due to the reduction in the power consumption of electronics and the increasing need to energize a massive number of low-power autonomous devices, WPT has attracted attention as a feasible and promising power supply technology for remotely energizing low-power devices, such as sensors, RFID tags, and consumer electronic. In addition, WPT can be integrated with WIT, so as to exploit radio waves for the dual purpose of communicating and energizing. **In this chapter, we provide a foundation of knowledge regarding WPT and its main module of rectenna. Furthermore, we introduce the concept of WIPT communications, the associated technologies, challenges and state-of-the-art.**

2.1 Wireless Power Transfer

The main EH sources studied in the literature as categorized as shown in Fig. 2.1. Specifically, these sources can be divided into renewable and EM waves [58]. However, these conventional natural energy sources (solar and wind) are usually climate and location dependent, making their use for EH in wireless communication systems, where providing a continuous and stable quality of service (QoS) is of paramount importance, challenging. Specifically, EM signals are the main energy sources that are naturally (ambient RF) or artificially (WPT) always present in the environment and can be considered in making self-powered devices for the B5G IoT ecosystem.

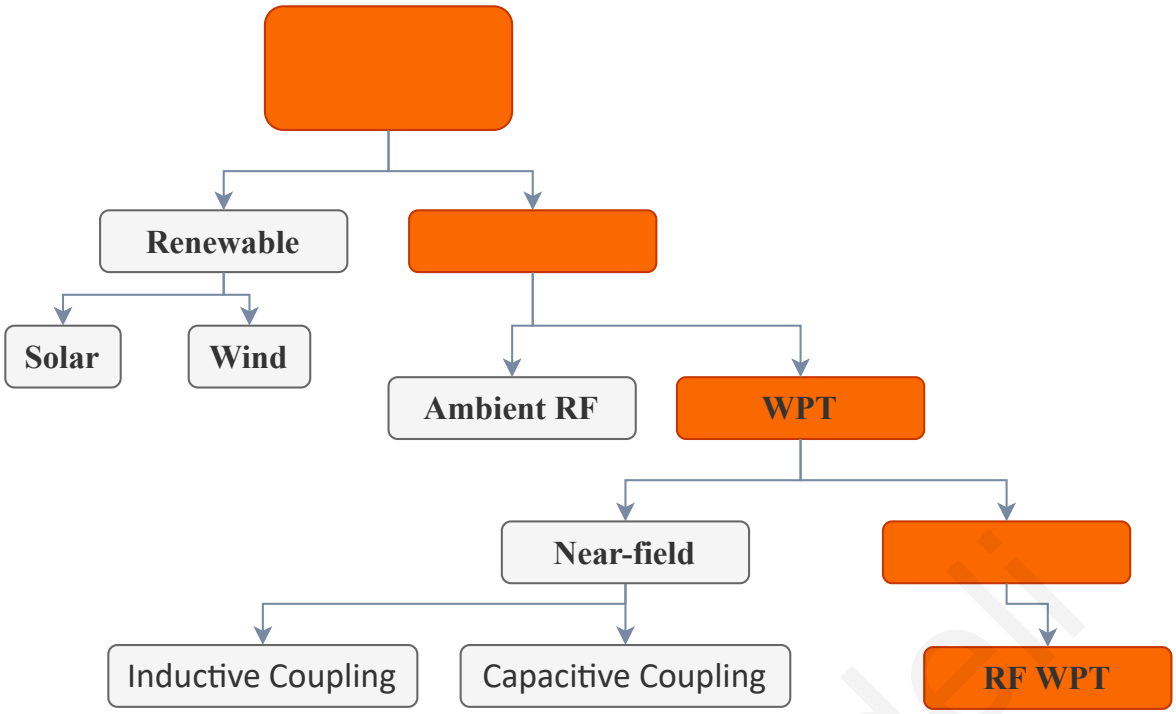

Figure 2.1: EH sources.

WPT is an innovative concept that was originally introduced by Nikola Tesla in the 1890s. WPT refers to the transmission of electrical energy from a power source by means of EM fields, to an electrical component without the aid of wired interconnections. A WPT system contains a transmitter connected to the main power source, which transforms the power to an EM field and one or more receiver devices to receive and harvest energy from the EM field. The existing WPT technologies can be categorized into two regions, non-radiative (near-field) and radiative (far-field).

2.1.1 Near-Field WPT

In the near-field region, power is transferred over short distances by magnetic fields using inductive coupling between coils of wire, or by electric fields using capacitive coupling between metal electrodes [59]. In particular, power is transmitted only when there is a receiver or any absorbing materials within the wavelength, which depends on the shape and size of the antenna on the transmitter. Therefore, if the distance between transmitter and receiver is larger than the wavelength of transmission medium, very little power can be harvested.

- **Inductive Coupling:** In inductive coupling, electrical energy is transferred via coils by means of a magnetic field and high efficiency can be achieved

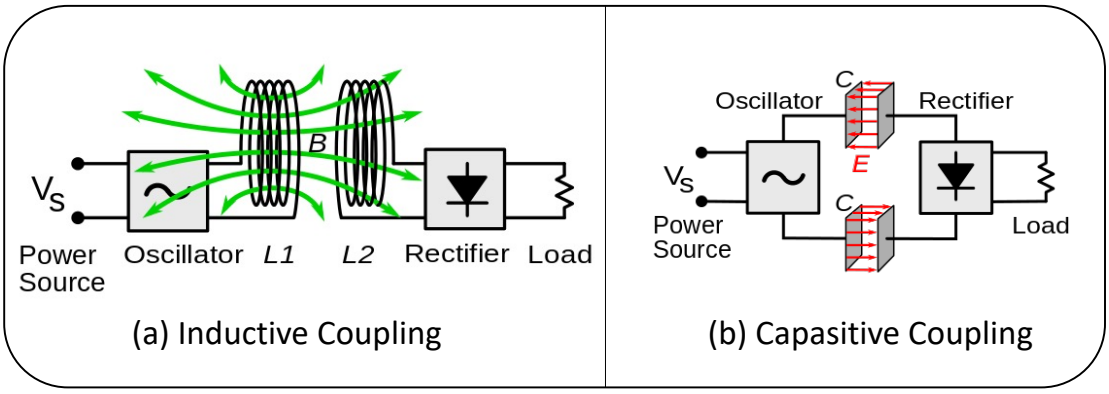

Figure 2.2: Near-Field WPT technologies.

when the coils are very close to each-other [60]. This technique is currently used in wireless charging for consumer electronic devices such as laptops, cellular phones and other portable devices, and also used to charge electric automobiles [61].

- **Capasitive Coupling:** Capacitive coupling is another near-field technology used to transfer power by using electric fields between electrodes like metal plates [62]. Capacitive coupling has only been used practically in a few low power applications, because the very high voltages on the electrodes that is required to transmit significant power can be hazardous. In contrast to magnetic fields, electric fields interact strongly with most materials, including the human body.

Inductive coupling is the most widely used wireless technology; its applications include charging handheld devices like phones and electric toothbrushes, RFID tags, induction cooking, and wirelessly charging or continuous WPT in implantable medical devices like artificial cardiac pacemakers, or electric vehicles.

2.1.2 Far-Field WPT

Far-field region describes the area where the distance is much larger than the diameter of the transmit antenna. Roughly 60 years ago, far-field WPT regained momentum and interest in high-power WPT, including the developments of the microwave-powered helicopter [63] and point-to-point long-distance WPT [64]. Despite those

successful field experiments, high-power WPT saw limited practical applications considering its high cost, bulky size, system efficiency, and safety issues. Therefore, intensive research efforts nowadays focus on low-power far-field wireless power harvesting technology tailored to sensing and communication [65], [18].

Far-field wireless power harvesting has two fundamental application scenarios depending on how RF power is transmitted to rectennas (rectifying antennas). In the first application, rectennas harvest pervasive RF power that is broadcasted by various sources in the environment, such as digital TV broadcasting towers, Wi-Fi access points, and cellular base stations [66]. RF power is transmitted omnidirectionally to ensure maximum coverage. In the second scenario, wireless power tranfer between power sources and rectennas utilizes beam technology [67]. By controlling the direction and width of beams, far-field wireless power harvesting becomes more efficient at the cost of system complexity. With the rollout of 5G, where beamforming techniques are massively used, far-field wireless power harvesting is believed to fully utilize them [68]. Due to transmission loss and safety concerns, RF power density in free space is normally limited, further resulting in the low rectifying efficiency of rectennas, which has a direct impact on system efficiency and applicability. Hence, the ultimate goal for rectenna design is to maximize rectifying efficiency and DC output.

Concluding this section, the near-field technology relies on near-field EM waves, which cannot support any mobility to energy-limited wireless communication devices due to the limited wireless charging distances (a few meters). In contrast, far-field WPT can enable the transmission of RF power over longer distances, while harvesting supports two different real-world application scenarios. Ambient RF energy harvesting is suitable for low-power and low-duty-cycle IoT sensing and communication applications. Such battery-free and maintenance-free applications are effective supplements for sustainable smart cities and similar applications. Directive RF WPT based on beamforming technology offers more flexibility and opportunities to support emerging wearable electronics, smart homes, and remote healthcare monitoring applications [69]. Moreover, it has to be noticed that the broadcast nature of wireless channels facilitates one-to-many wireless charging, which is crucial for wireless networks with large numbers of energy-limited devices, as in B5G IoT networks.

2.2 Rectenna

A rectenna is a device that captures EM waves, rectifies and filters them via a LPF and is commonly used in WIPT solutions.

2.2.1 Rectenna Structure

In this section, we introduce some basic knowledge on rectenna structure, in order to understand how the circuit design influences the WPT performance and system design. The receiver in Fig.2.3 illustrates the schematic diagram of a typical rectenna. In order to power the low-power device, a rectifier circuit is required to convert the received RF signal to DC. The recovered DC power then either powers a low-power device directly, or is stored in a battery for higher power low duty-cycle operations. Maximizing the efficiency of each part can be an effective strategy to obtain an enhanced total efficiency of the rectenna.

Antenna: An antenna is responsible for capturing RF signals. RF antennas receive energy from a variety of sources such as mobile phones (900-950 MHz), local area networks (2.4 GHz – 5.8 GHz), Wi-Fi signals and broadcast ultra high frequency television signals. Miniaturised size and high antenna gain are the main aims of antenna technology, while maximizing antenna efficiency means harnessing as much RF energy in free space as possible. In order to succeed this, several characteristics are taken into consideration. Firstly, the relative low-power spectral density in single bands makes multiband or broadband antennas desirable for RF EH [70]. Furthermore, since the receiving power of an antenna is directly associated with its physical size, the array technique is an efficient solution to acquire more RF power by increasing the effective antenna aperture [71]. Additionally, antenna polarization mismatch between RF sources and rectennas results in reduced RF power reception and thus less DC output from rectennas. The best possible way to target ambient RF sources whose polarization is unknown, is to employ an all-polarization technique; while for the beamforming directive wireless power harvesting, where multiple moving rectennas may exist, circular polarization is often introduced due to its rotation independence between transmitter and receiver [72].

Matching Network: The main function of a matching network is to increase input voltage of the rectifier and to minimize the transmission loss from the antenna to the rectifier. When impedance of the loads and impedance at the antenna output

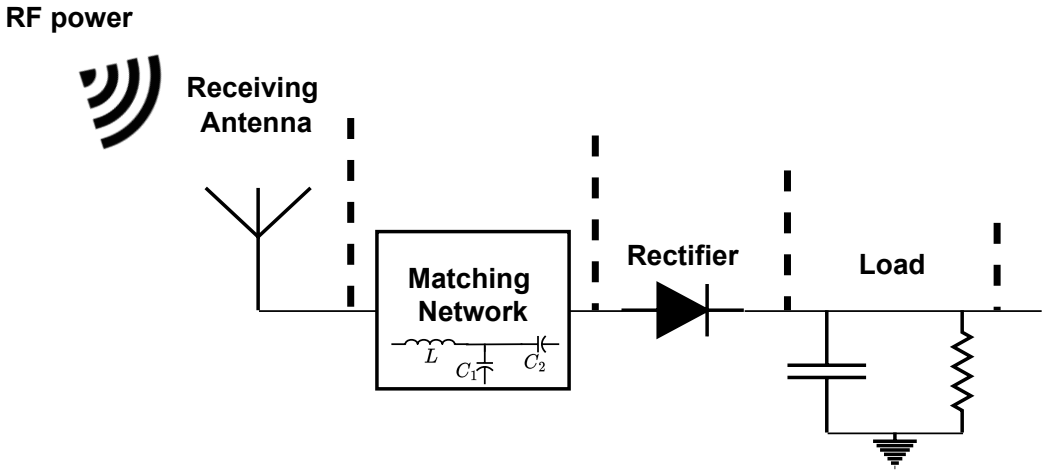

Figure 2.3: Schematic diagram of the rectenna.

are matched together, the maximum power transfer can be achieved, and is known as impedance matching. Matching network design in rectennas becomes challenging due to the wide variations of diode input impedance, which is sensitive to both frequency and input power.

To overcome the impedance variations due to the change of diode operation conditions, a tunable matching network can be employed [73]. Hence, it is possible to maintain a low insertion loss in matching networks in a wide dynamic range of operating frequency and input power. For example, an ultrawideband rectenna achieves an operation frequency range from 0.9 to 3 GHz through a complementary matching stub [74]. Another solution is to design the receiving antenna to match the diode directly, which can remove the matching network [75]. As the diode mainly shows the capacitive component, designing an inductive antenna can match the diode's impedance conjugately. In [76], a 4×4 cross-dipole array is developed, to directly match the rectifying circuit at the dipole plane. Experiments show that this design has enhanced the available power for each diode and thereby increased the efficiency.

Rectifier: The function of a rectifier is to convert the input RF signals captured by an antenna into DC voltage, mostly using semiconductor elements due to their low-cost and small form factor [77]. RF to DC conversion efficiency is determined by the diode in the circuit of the rectifier, which is the main component [78]. Details regarding the diode's main circuit parameters, are described in Appendix A.4. Multiple measures can be introduced to leverage diode conversion efficiency. One of those is to increase the RF input power. To increase the available power, one

solution is to combine with other energy sources, such as solar [79], thermal [80], and vibration energy [81].

Another characteristic that may be taken into consideration for the increase of DC output voltage is operating temperature of the diode. For Schottky diodes that are dependent on thermionic emission, a lower operating temperature helps to leverage the conversion efficiency of junction resistance. Temperature variations have an influence on diode behaviors, therefore an optimum operating temperature exits at each input power level [82]. Thus, the thermal factor should be taken into consideration for maintaining good performance in a practical situation.

Furthermore, the nonlinear resistance of Schottky diodes can be characterized by an exponential $I - V$ relationship [20], resulting in higher rectifying efficiency, when specially designed signal waveforms are used. With the popular trend of developing SWIPT systems, the significance of accounting for the nonlinearity of rectifiers is highlighted for waveform design and optimization in [83]. Various strategies and signal waveforms exist in literature [84], [85] that take into account the nonlinearity of the rectification circuit. Similar findings, demonstrate that waveforms with high peak-to-average-power-ratio (PAPR) e.g., multi-sine, chaotic signals etc, boost the wireless energy transfer efficiency [86], [87].

2.2.2 Rectenna Architectures

Additionally, conversion efficiency may be enhanced with the use of appropriate rectenna architectures. Specifically, there are two basic schemes in the literature: i) DC combining, where each antenna branch incorporates its own rectifier to separately harvest power, and ii) RF combining, where all the antennas are arranged to channel the RF power to a single rectifier.

RF combining strategy is based on multiple antennas, which results in a higher efficiency due to more power fed to one single rectifier [88], [89]. On the other hand, in DC combining, each antenna branch incorporates its own rectifier to separately harvest power, which results in lower conversion efficiency compared to RF combining scheme, since the rectifiers must individually rectify low RF powers [90]. Furthermore, there are also some studies trying to succeed a hybrid solution. The authors in [91], adopt the beamforming matrix in a hybrid power combining rectenna array. While, in [92] authors consider a single-input multiple-output (SIMO) topology,

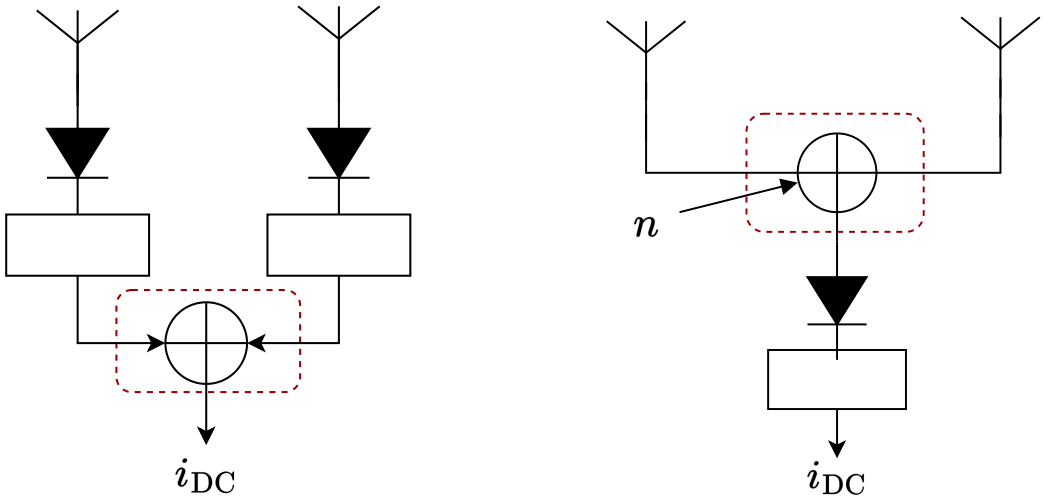

Figure 2.4: Rectenna architectures.

where each receive antenna is connected to multiple rectifiers.

2.3 Challenges of WIPT

Despite the conveniences introduced by the WPT technology, its integration into communication networks also introduces many challenges. In practice, there is the need to strike a balance in the trade-off between information and power transfer, leading to significantly different resource allocation algorithms, system models, receiver architectures and interference management schemes, compared to conventional wireless data communications. Hence, the development of novel design theories, hardware circuit architectures, and signal processing techniques to unlock the potential of WIPT networks, is crucial.

The main challenges of WIPT are [93]: *Range:* Delivery of wireless power at distances of 5-100 meters for indoor/outdoor charging of low-power devices. *Efficiency:* Boosting the end-to-end power transfer efficiency, or equivalently the DC power level at the output of the rectenna(s) for a given transmit power. *Non-line-of-sight (NLoS):* Support of LoS and NLoS to widen the practical applications of WIPT networks. *Mobility support:* All mobile users, or at least users at low speeds, should be supported. *Ubiquitous accessibility:* Support of ubiquitous power accessibility within the network coverage area. *Safety and health:* Resolving the safety and health issues of RF systems and compliance with the regulations. *Energy consumption:* Limitation

of the energy consumption of energy-constrained RF powered devices. Solutions to tackle these challenges are being researched and have been discussed extensively in [94]- [98]. They cover a wide range of areas spanning from sensors and IoT devices, RF communication, to signal and system designs for WPT.

2.4 SWIPT and BackCom in B5G IoT

IoT networks are going to enable an increasingly intelligent world with ambient-assisted living, smart controlling, and real-time data monitoring. This will need the pervasive connectivity of trillions of low-power wireless sensors, actuators, and small computing devices to formulate cost- effective and self-sustainable wireless sensor networks. Therefore, SWIPT and BackCom, under the umbrella of WIPT, are important enablers for B5G IoT networks, where devices and sensors could be continuously powered using energy sources, simultaneously targeting to improve the data rate and communication range. In this section, we present the state-of-the-art for SWIPT and BackCom in B5G IoT networks.

2.4.1 SWIPT

One of the main deployment challenges in B5G IoT is the maintenance of a reliable communication with the use of low cost and limited energy in devices. Devices such as sensors in IoT are small and, usually, placed in hazardous or remote areas where human access is limited. Therefore, replacing the batteries and supplying a stable power source is an issue for B5G IoT wireless sensor networks.

Currently SWIPT is a key technology for the emerging B5G IoT networks, considering that is applied in solutions that require energy efficiency, low-cost, low-power and low hardware complexity. Compared to systems performing WIT and WPT separately, SWIPT systems are more spectrally and energy efficient since they utilize the same bandwidth and power for the dual purpose of WIT and WPT. SWIPT systems are of particular interest for low-power devices which have no access to a fixed power supply and therefore are interested in receiving not only information but also energy.

The authors in [99] apply SWIPT to cooperative clustered wireless sensor networks, where energy-constrained relay nodes harvest the ambient RF signal and use

the harvested energy to forward the packets from sources to destinations. Specifically, a power splitting spectrum sharing protocol and hybrid time switching scheme for EH wireless sensor nodes, is proposed. In [100], authors investigate optimal resource allocation for SWIPT in the downlink of wireless powered sensor networks, targeting and succeeding to maximize the uplink sum rate while guaranteeing the QoS (i.e., satisfying the downlink rate constraint) at the key sensor node. Two scenarios with space division multiple access (SDMA) and time division multiple access (TDMA) in the uplink are considered.

In [101], a novel SWIPT scheme for IoT is proposed. Different from the conventional power splitting and time switching schemes, the proposed scheme sends the wireless power via the unmodulated high-power continuous wave (CW) and transmits information by using a small modulated signal in order to reduce the interference and to enhance the power amplifier efficiency. The core contribution of this work is the design and analysis of a receiver circuit that is suitable for IoT devices and is able to simultaneously extract power and data in the proposed SWIPT signal. While the authors in [102], propose a novel SWIPT scheme, which separates the power and data signals in the frequency domain. Namely the frequency-splitting (FS) SWIPT, which separates the power and data signals in the frequency domain. The proposed FS SWIPT scheme is advantageous in that it can maximize the efficiency of the high power amplifier in consideration of its nonlinearity. They show that the proposed FS SWIPT greatly outperforms the power-splitting SWIPT in terms of the harvested power and SNR.

2.4.2 BackCom

Backscatter is a passive communication technology that can effectively address communication and energy efficiency problems for low-power communications systems such as sensor networks [103]. This is due to the simplicity of the BT and the ability to minimize the usage of batteries or even completely eliminate them, by taking advantage of WPT, as well as EH. Modulated backscatter techniques were first introduced by Stockman in 1948 [104] and quickly became the key technology for low-power wireless communication systems. BackCom has found many useful applications in practice such as smart homes and cities [105], biomedical field [106], environmental monitoring systems [107], vehicle monitoring [108] and sensor networks [109].

Specifically, an RF tag is illuminated by an RF source and transmits a binary message to a RN. In particular, the BT modulates a part of the received signal with the desired information, and then transmits "1" or "0" back to the RN, by backscattering or not the RF waves, without the need to generate RF signals by itself [110] - [112]. The tag changes its state by switching the load impedance connected to its antenna. The state of the tag can be detected by a simple energy detector reader. The rest of the received signal from the RF source, is used by the BT for harvesting energy, thus making it possible to operate exclusively its own integrated circuit or partially support it, in terms of energy required. Since no oscillators are needed at the tags to generate carrier signals, BackCom generally entail orders-of-magnitude lower power consumption than conventional radio communications. As such backscatter is an appealing solution for B5G IoT networks, while emerging works from the state-of-the-art follow in the next paragraphs.

In [113], a hybrid backscatter system is proposed as a promising scheme for green IoT. They develop a novel hybrid scheme that integrates the backscatter communication and the harvest-then-transmit protocol. Numerical results validate that the proposed scheme improves the performance of the secondary system evidently compared with benchmark methods. The authors in [114] developed a BackCom assisted WPCN, which consists of multiple energy-constrained sensor nodes, powered by a dedicated power source and the data access point. In the proposed system, power source performs CSI and energy beamforming that helps the sensor nodes to achieve energy harvesting and information backscattering. Numerical results showed that, compared to conventional WPCNs, the proposed model achieved better throughput performance with an advantage of reduced system hardware complexity.

Considering a realistic backscatter communication and wireless sensing network, multiple numbers of radio transmitters, receivers, and backscatter tags will be needed to formulate the wireless links and decent network coverage. The joint beamforming and waveform design was proposed in [115] for a multiple-input–single-output WPT scenario; it has been verified that the output DC power can be greatly improved due to the waveform and beamforming strategies. Furthermore, it has to be noticed that the tag as long as harvests energy from the incident carrier waves, reflects no signals during this period. As such, the tag has a duty cycle behavior, therefore the duty cycle performance of the backscatter space-time code should be considered in practice for the coding design. Motivated by this, authors in [116]

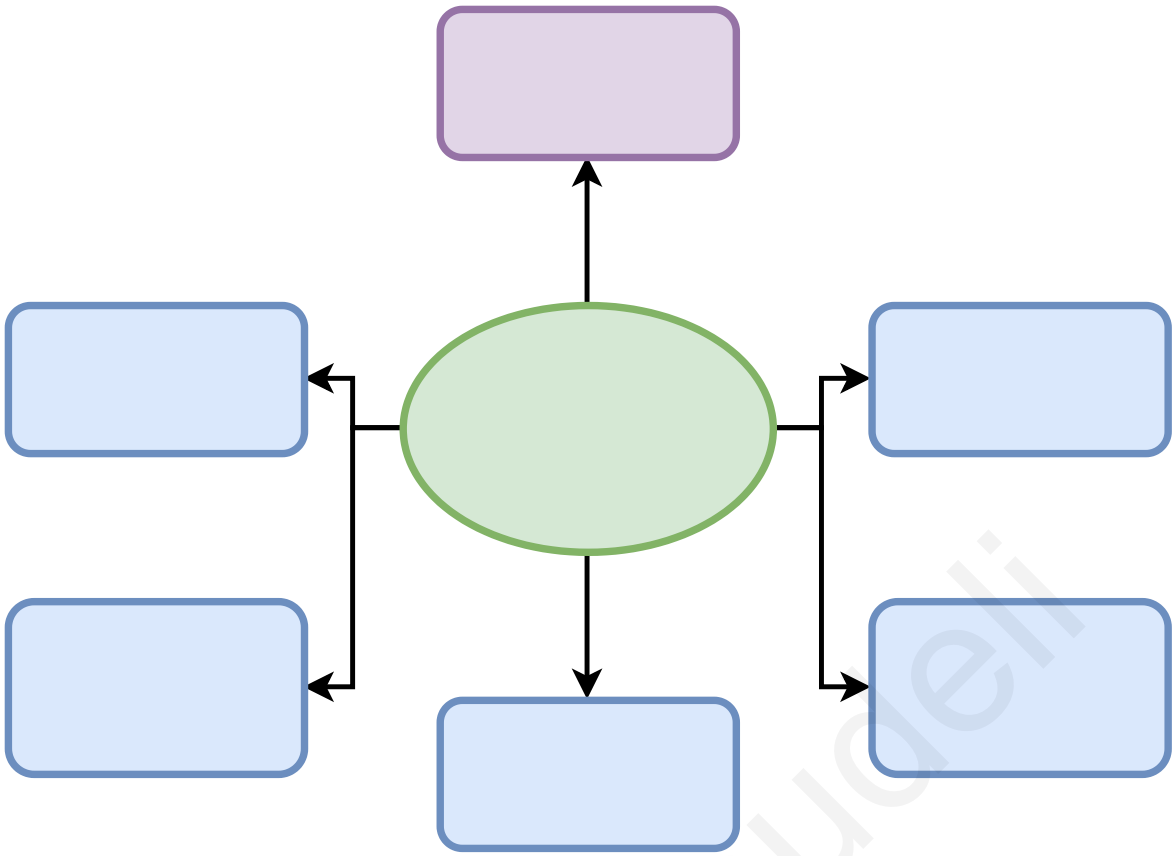

Figure 2.5: Emerging communication technologies in SWIPT and BackCom.

propose a 2×2 orthogonal space-time block code for backscatter communications in terms of the duty cycle and error performance. It is shown than the duty cycle of the proposed code is considerably higher than that of Alamouti code for both linear and nonlinear EH model, and prove that the symbol error rate (SER) of the proposed code is same as, or even better than that of Alamouti code in MIMO backscatter channel under various power transmission schemes. Therefore, the outage capacity, as the overall performance, of the proposed code, is better than that of Alamouti code.

2.5 SWIPT and BackCom in other B5G technologies

In this section we present other emerging technologies associated with SWIPT and BackCom in B5G networks. In Fig.2.5, we illustrate all of the emerging technologies along with the relative literature.

2.5.1 Massive MIMO

Massive MIMO is a key enabling technology for B5G wireless communication networks. Many advantages, such as efficient power transmission, strong energy directivity, high spatial resolution, and strong robustness make massive MIMO systems attractive to be combined with SWIPT to enhance the system transfer efficiency [117]. The authors in [118] investigate the downlink transmission of a single-cell massive MIMO SWIPT-enabled system with the power-splitting technique, maximizing the system's energy efficiency. Furthermore, the authors in [119] present and evaluate the performance of an ambient backscatter system equipped with a massive MIMO antenna at the reader side, demonstrating that the performance is significantly improved by the massive MIMO reader.

2.5.2 Cooperative Relaying Network

The concept of relay was first introduced in [120]. Cooperative relay (CoR) is a technique in which nodes are cooperating for their communication. CoR ameliorates the effects of fading, path loss, shadowing, small coverage, and low signal-to-noise ratio (SNR) [121] in order to increase bandwidth availability and spectral utilization [122]. The motivation of using SWIPT and CoR is to provide energy and spectral efficiency next generation wireless networks. Comprehensive reviews of SWIPT technology that enables the use of CoR networks for 5G and B5G mobile networks including the significance, technologies, and protocols which can be applied are studied in [123], [124], [125].

Intelligent reconfigurable surfaces (IRS) have swayed the research community recently, primarily becoming a potential candidate technology for B5G wireless networks. An IRS is composed of a set of reflecting units which are reconfigurable, and their phase shifts can be controlled according to the changes in reflection from the wireless communication environment. As a matter of fact, IRS can suitably reflect RF signals transmitted from transmitters to desired directions, such that the received signal power can be effectively enhanced at the intended destinations while suppressing interference at undesired receivers [126].

In [127], authors exploit the cooperative transmission as a new energy supply to support BackCom, where there are multiple decode-and-forward relays and only one relay is selected in the cooperative system. Authors in [128] propose a system

that integrates ambient BackCom with IRS technology to overcome the fundamental coverage limitation of conventional backscatter communications. Specifically, they replace the antenna-switching tag with such IRS elements.

2.5.3 NOMA

The baseline idea of NOMA is to serve multiple users using the same resource in terms of time, frequency, and space. NOMA uses superposition coding at the transmitter such that the successive interference cancellation (SIC) receiver can separate the users both in the uplink and in the downlink channels. Furthermore, it is possible to separate the high level signals and cancel them out to retain a low level signal at the receiver [129]. Cooperative NOMA in 5G systems with SWIPT has been considered in [130] using a network model with one base station and two user groups. SWIPT, BackCom and NOMA are potential spectral and energy efficiency improving technologies for the B5G wireless networks. Applying such technologies will not only boost the system performance, but also showcase that they can be operated in tandem in future networks.

Authors in [130] propose a novel NOMA assisted cooperative spectrum-sharing network, where the SWIPT technique is utilized by the secondary transmitter to harvest the primary signal's energy. Furthermore, a cooperative network where a source node communicates with two NOMA users through an EH based relay is analyzed in [131] to investigate the impact of power allocation policies in NOMA-SWIPT networks. Joint power allocation and time switching control for energy efficiency optimization in a time splitting-based NOMA-SWIPT system is proposed in [132]. Authors in [133] show that the proposed scheme can enhance the transmission reliability without impairing the spectrum efficiency, which makes backscattering an appealing solution to cooperative NOMA downlinks.

2.5.4 mmWave Communication

MmWave communication is a key technology for 5G communication networks that can provide ultra-high data rates as a result of relatively high frequencies (between 30 and 300 GHz) of large spectrum resources. In [134], it is shown that mmWave is a prominent technology for WPT due to factors such as high frequencies, narrow beams, larger array gains and dense networks, etc. The work in [135], provides a

manageable framework to characterize performance of SWIPT assisted large scale mmWave communication network. In [136], authors develop a joint design of transmit power allocation, beamforming, and receive power splitting for SWIPT downlink systems in wideband mmWave channel. Authors in [137], propose a method of communicating between two vehicles in mmWave area, with a use of a radar and a modulated BT.

2.5.5 D2D Communication

Device-to-Device (D2D) communications enable communication between devices located in a given range without the involvement of a base station. It helps to improve the network capacity and resource utilization [138]. D2D communications have been used for relaying transmission to increase the communication reliability [139]. SWIPT enabled D2D communication in large scale cognitive networks has been studied in [130]. In [140], authors address the issue of D2D power allocation with SWIPT. Additionally, in [141] authors introduce a hybrid D2D communication paradigm by integrating ambient backscattering with wireless-powered communications.

Concluding this chapter, we note that in the state-of-the-art, several aspects of SWIPT and BackCom are examined, in order to succeed an enhanced performance for B5G networks. From the characterization of the fundamental trade-off between how much information and how much energy can be delivered in a wireless network, how signals should be designed to achieve the best possible trade-off between them, to the systems' design such that the RF radiation and the RF spectrum are exploited in the most efficient manner to deliver information and/or energy. In this thesis, we focus on low-complexity solutions for B5G IoT, utilizing tools from communication and signal processing theory, though the proposed topologies and derived performance analysis could be extended to other emerging technologies as well.

Chapter 3

Integrated SWIPT receiver with non-coherent detection schemes

In this chapter we achieve SWIPT using an integrated receiver with non-coherent ID and we succeed an enhanced performance in terms of SER and EH. Specifically, we propose an innovative single rectenna sequential decoder, which reduces the complexity of conventional counterparts and overcomes error floor phenomena. In the state-of-the-art, similar solutions are adopted in different contexts and not for the implementation of SWIPT. In our study we compare our proposed integrated sequential SWIPT decoder to a conventional power-splitting receiver.

3.1 Introduction

SWIPT is a fundamental architecture in wireless powered communications, where RF signals simultaneously convey data and energy to devices. Due to practical constraints, SWIPT cannot be performed from the same received signal without losses, so practical implementations split the received signal in two parts, where one part is used for information transfer and another part is used for power transfer [18]. In the new era of IoT and machine type communications, there will be a need for massive deployment of smart devices and vast amount of information exchange, making it impractical, even impossible, to individually recharge/control all these devices on a regular basis [142]. Towards this technological evolution, SWIPT technology is of significant importance for energy supply and information exchange.

Regarding the SWIPT concept, Varshney first proposed the idea of transmitting information and energy simultaneously in [11]. In [13], Grover and Sahai extended the work to frequency-selective channels with AWGN. In [20], a novel design of a SWIPT receiver was proposed, in which the information decoding and the energy harvesting circuits are integrated. The replacement of the active RF to baseband conversion with a passive rectifier operation, has as a direct result the reduction of the energy cost for ID. Given the nature of the integrated architecture, decoding of the transmitted information is succeeded, by detecting the power variation in the received signal.

In [39], a SWIPT solution with the use of integrated receiver and precoding on the energy patterns is presented. However, such a solution relies on the availability of CSI at the receiver, resulting to a coherent decoding scheme. Coherent techniques are a challenging task. In the literature, but in different contexts, there are studies for non-coherent detection techniques, which can result in an enhanced SER [143], [144], without profoundly increasing the decoding complexity at the receiver side. Such techniques are generalized likelihood ratio test-maximum likelihood sequence detection (GLRT-MLSD), Viterbi-type trellis-search algorithm and selective store strategy (SS-ST).

To the best of our knowledge, there has not been a similar study in SWIPT literature. The available studies, focus on the use of a separated receiver architecture for the achievement of SWIPT and on coherent detection techniques. Two popular SWIPT schemes, power splitting (PS) and time switching (TS), and their integrations with various wireless technologies have extensively been studied (e.g., [20]). We propose a novel solution based on the integrated SWIPT receiver architecture and apply non-coherent detection. The existing works and our proposed new single-rectenna SWIPT architecture can be viewed as the pursuit to the same goal of the optimized SWIPT, but with different architecture at the receiver side and adopted decoding techniques. To this end

- We study the architecture of an integrated receiver, where the RF to baseband conversion is replaced with a passive rectifier, while we adopt a non-coherent detection scheme, avoiding the signaling overhead and processing burden of training symbols.

- First, we analyze the symbol by symbol (SBS) detection, based on an equi-

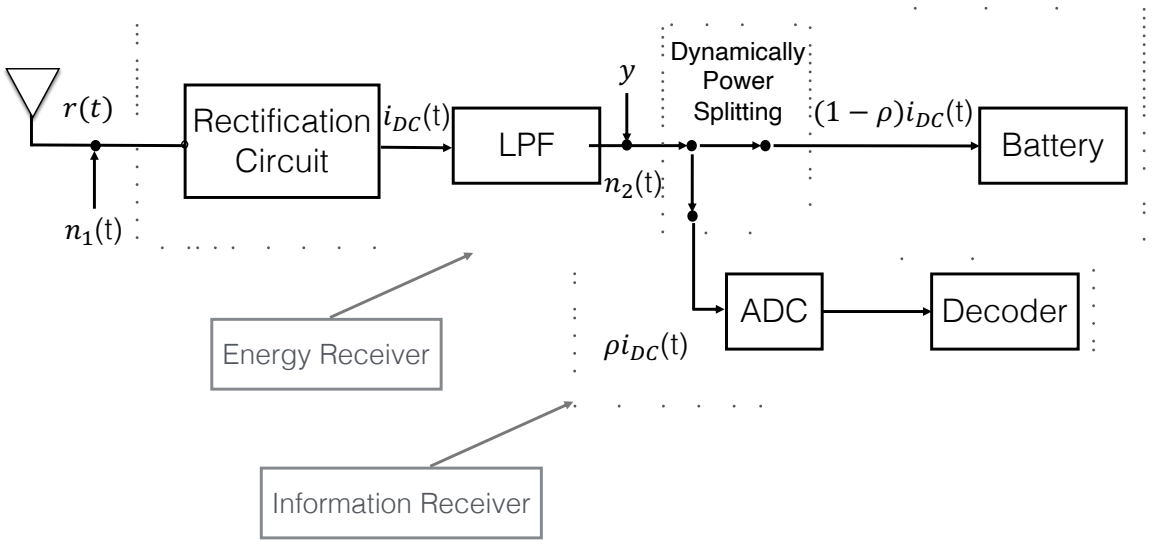

Figure 3.1: Architecture of the integrated receiver.

spaced pulse energy modulation (PEM) scheme [39]. In addition, we optimize the pattern of the transmitted energy pulses with and without a level of power sensitivity at the side of the receiver [40].

- Following this, we enhance the SER performance, by proposing a sophisticated sequential decoding scheme. More specifically, with the use of GLRT-MLSD and Viterbi-type trellis-search algorithm [143] (see Appendix A.5), we manage to diminish the computational complexity originating from the sequential detection and finally propose a simplified decision rule.

- Furthermore, we show that with the use of SS- ST, our proposed integrated decoder, denoted as integrated SEQ-MLSD, can overcome the error floor problem.

- Simulation results match the theoretical ones, thus validating our study on an innovative sequential and non-coherent decoder, which enables low values of SER and high EH.

3.2 System Model

We consider an integrated information and energy receiver, as shown in Fig. 3.1, for a single input single output wireless link. At the transmitter side a baseband signal $x(t)$ is transmitted, with $\mathbb{E}[x^2(t)] = 1$. The modulation scheme used by the transmitter is PEM, with M energy levels. We design our energy pulse based symbol

alphabet, based on equi-spaced amplitudes as in [39]. Specifically, we assume that a set of M symbols $x_i \in \{1d, 2d, \ldots, Md\}$, are mapped to each energy level, where d is the distance between the energy pulse based symbols. Therefore, we have

$$\mathbb{E}[x^2(t)] = \frac{1}{M}\sum_{i=1}^{M} x_i^2 = \frac{d^2}{6}(M+1)(2M+1) = 1, \tag{3.1}$$

which results in

$$d = \sqrt{\frac{6}{(M+1)(2M+1)}}. \tag{3.2}$$

The baseband signal is then up-converted to generate an RF signal, which is transmitted over a Rayleigh fading channel. The received complex signal $r(t)$ is given by [20]

$$r(t) = \sqrt{E_{\text{ave}}h}x(t) + n_1(t), \tag{3.3}$$

where E_{ave} is the average transmitted power, $\sqrt{h}$ is the channel coefficient, modeled as complex Gaussian random variable with zero mean and unit variance. We assume that CSI is not available at the receiver and non-coherent detection is applied. Finally, $n_1(t)$ is the noise modeled as an additive white Gaussian noise (AWGN) with unit variance.

At the integrated receiver, the received RF signal $r(t)$ is converted to a DC signal $i_{\text{DC}}(t)$ by a rectification circuit. This signal is dynamically split, into two streams with power ratio $1-\rho(t)$ for energy harvesting and $\rho(t)$ is sampled and digitalized by an analog-to-digital converter (ADC) for further information decoding, where $0 < \rho(t) < 1$. Then, the DC output of the LPF[1] is [39]

$$i_{\text{DC}}(t) = \left|\sqrt{E_{\text{ave}}h}x(t) + n_1(t)\right|^2 + n_2(t), \tag{3.4}$$

where $n_2(t)$ is the noise added from the rectifier, modeled as an AWGN with unit variance. In order to reduce the energy requirements for information decoding and jointly maximize the power split for energy harvesting, we consider $\rho(t) \to 0$ [20]. Furthermore, in practice, the antenna noise power is much smaller than the rectifier noise power, thus it can be omitted ($n_1 \to 0$). Assuming that the symbol period is one and by normalizing $n_2(t)$, the channel at the information decoder can be equivalently viewed as a power signal and is given by

$$y = E_{\text{ave}}hx^2 + n_2, \tag{3.5}$$

[1]For reasons of simplification, we assumed a linear model for the energy harvested. Non-linear models were considered in future work.

where x denotes the signal power, y the channel output, h the power gain of the channel and n_2 the rectifier noise.

The harvested energy denoted by Q in Joule is given by [20]

$$\begin{aligned} Q = \zeta \mathbb{E}[i_{\mathrm{DC}}(t)] = \zeta \mathbb{E}[E_{\mathrm{ave}} h x^2] &= \zeta \int_{E_{\mathrm{sens}}}^{\infty} \frac{h}{E_{\mathrm{ave}}} \exp\left(-\frac{h}{E_{\mathrm{ave}}}\right) dh \\ &= \zeta (E_{\mathrm{ave}} + E_{\mathrm{sens}}) \exp\left(-\frac{E_{\mathrm{sens}}}{E_{\mathrm{ave}}}\right), \end{aligned} \tag{3.6}$$

which follows from the fact that h is exponentially distributed with mean E_{ave}; E_{sens} denotes the level of power sensitivity at the receiver and $0 < \zeta \leq 1$ is the conversion efficiency, which we assume throughout this work $\zeta = 1$. Here we ignore the energy from the noise assuming that it is negligible. In the case, where we do not apply a level of power sensitivity at the receiver side, i.e. $E_{\mathrm{sens}} = 0$, the harvested energy from (3.6) results in $Q = E_{\mathrm{ave}}$.

3.3 SBS Decoding

In this section, we study SBS detection with the use of maximum likelihood estimation. Integral forms for the SER of all the considered schemes are derived.

3.3.1 Performance Analysis

The total pairwise error probability regarding adjacent symbols, can be calculated considering two independent events A and B. The event A is characterized by the fact that the received signal y is negative. In such a case, the integrated receiver does not proceed neither with information decoding nor with energy harvesting. As a consequence, we have an outage no matter what was the trasmitted symbol.

Thus, the pairwise error probability given that the event A holds, equals the probability of $E_{\mathrm{ave}} h x_i^2 + n_2 \leq 0$ for all x_i, given by

$$P_{\mathrm{pair}}(A) = \frac{1}{M} \sum_{i=1}^{M} P(n_2 \leq -E_{\mathrm{ave}} h x_i^2) = \frac{1}{M} \int_0^{\infty} \frac{1}{2} \exp(-h) \left(M + \sum_{i=1}^{M} \mathrm{erf}(-E_{\mathrm{ave}} h x_i^2) \right) dh, \tag{3.7}$$

which follows by substituting the cumulative distribution function of the AWGN term n_2 [145, Eq. (2.3-11)] and integrating for all the possible values of h.

Respectively, the event B is characterized by the fact that the received signal y is positive. Given this and in contrast to the event A, we are not always in outage.

More specifically, the pairwise error probability for adjacent symbols given that the event B holds and assuming that symbol x_i was transmitted, is defined by

$$P_{\text{pair}}(B) = \frac{1}{MP(B)} \sum_{i=1}^{M} P(e_{x_i}), \tag{3.8}$$

where $P(e_{x_i})$ is the probability of error, that the receiver wrongly decides on x_{i+1} or x_{i-1} symbol, while x_i was transmitted. Thus,

$$\sum_{i=1}^{M} P(e_{x_i}) = \sum_{i=1}^{M} \Big[P(e_{i\to i+1}) + P(e_{i\to i-1}) \Big], \tag{3.9}$$

where $P(e_{i\to i+1})$ and $P(e_{i\to i-1})$, denote the pairwise error probability on deciding symbol x_{i+1} or x_{i-1}, respectively, when symbol x_i was transmitted and are given in the Appendix B.1.

Furthermore, $P(B)$ represents the probability that the received signal y is positive, i.e. $E_{\text{ave}} h x_i^2 + n_2 > 0$, for any trasmitted $x_i \in \{1d, 2d, \ldots, Md\}$. Following the steps for the calculation of $P_{\text{pair}}(A)$ in (3.7), we can similarly estimate

$$P(B) = \frac{1}{M} \int_0^{\infty} \frac{1}{2} \exp(-h) \left(M - \sum_{x_i=1}^{M} \text{erf}(-E_{\text{ave}} h x_i^2) \right) dh. \tag{3.10}$$

By substituting (3.9) and (3.10) in (3.8), we can derive the total pairwise error for the integrated receiver, referring to a SBS detection as

$$P_{\text{SER\_sbs}} = P_{\text{pair}}(A) + P_{\text{pair}}(B). \tag{3.11}$$

3.3.2 Optimized Performance Analysis

In this subsection, we study the optimization of the integrated SBS decoder (OSBS), targeting the minimization of $P_{\text{SER\_sbs}}$. In order to achieve this, we consider that our energy pulse based symbol alphabet is no longer based on equi-spaced amplitudes. We thus define a new constrained non linear optimization problem. We set an objective function that we need to minimize, subject to specific non linear equalities and linear inequalities expressed as

$$P_{\text{OSBS}} = \min_{x_i} P_{\text{SER\_sbs}}$$

$$\text{subject to } \mathbb{E}[x^2] = 1,$$

$$f_Y(y_{x_i}) = f_Y(y_{x_i+1}), \quad i \in \{1, \ldots, M-1\},$$

$$x_i \leq x_{i+1}, \quad i \in \{1, \ldots, M-1\}, \tag{3.12}$$

where $f_Y(y_{x_i})$ denotes the probability density function (pdf) of the received signal y when x_i is transmitted, $f_Y(y_{x_{i+1}})$ denotes the pdf of the received signal y, when x_{i+1} is transmitted and are given in the Appendix B.1. Such an optimization problem, can be solved reliably and efficiently with existing numerical tools, such as *fmincon* in Matlab [146], which employs the interior-point method.

3.3.3 Optimized Performance Analysis with Power Sensitivity

Applying a level of power sensitivity in the integrated receiver, we target a more sophisticated scenario of the SBS detection (OPS). The integrated receiver proceeds to information decoding and energy harvesting, if and only if the received power of the DC signal is higher than a given sensitivity level. Such an assumption, results in two new events A' and B'; A' is characterized by the fact that $E_{\text{ave}} h x_i^2 + n_2 \leq E_{\text{sens}}$, and B' from the fact that $E_{\text{ave}} h x_i^2 + n_2 > E_{\text{sens}}$. Following the steps which are analytically described in Section 3.3.1, we can calculate the new SER of the system.

3.4 Sequential Decoding

In this section, we exploit the coherence time of the channel over N transmitted energy pulses, and study sequential detection. With the use of such a detection scheme, the performance of the integrated SWIPT receiver is enhanced, in terms of SER. However, in order to keep a low computational complexity, our study focuses in more sophisticated techniques. Specifically:

- Our first step is focused on detecting a subsequence of the transmitted energy pulses, with the use of GLRT-MLSD. In this way, we derive a simple decision rule for information decoding, that is independent of the channel gain, succeeding non-coherent detection.
- Secondly, with the use of Viterbi-type trellis-search algorithm, we manage to reduce the search complexity of the proposed decision metric.
- Finally, with the use of SS-ST, we eliminate the error floor.

At the end of this section, we provide integral forms for the upper bounds derived, regarding the SER performance of our proposed integrated SEQ-MLSD decoder and the conventional power-splitting SWIPT receiver.

3.4.1 Sequence Detection

We consider a subsequence of L immediate past symbols, out of the entire transmitted sequence with coherence length N. At time t, the transmitted data subsequence is denoted by $\mathbf{x}(t,L) = [x(t-L+1), \ldots, x(t)]$, where $x(t) \in \{1d, 2d, \ldots, Md\}$ for any time t. Similarly, $\mathbf{y}(t,L) = [y(t-L+1), \ldots, y(t)]$ and $\mathbf{n}_2(t,L) = [n_2(t-L+1), \ldots, n_2(t)]$ are used to denote the corresponding received signal subsequence and noise subsequence, respectively. For the sake of simplicity, we drop the index terms t and L and denote the vectors $\mathbf{x}$, $\mathbf{y}$ and $\mathbf{n}_2$. Thus, the received signal is modeled as

$$\mathbf{y} = E_{\text{ave}} h \mathbf{x} + \mathbf{n}_2. \tag{3.13}$$

Having defined our subsequence, we target on a detection scheme that will be independent from the channel gain h. A GLRT-MLSD decoder is used, in order to jointly decide on h and $\mathbf{x}$, that maximize $p(\mathbf{y}|\mathbf{x},h)$, which is the conditional pdf of $\mathbf{y}$. With the use of maximum likelihood, h is estimated conditioned on a hypothesized data subsequence $\mathbf{x}$. Then, with the proper substitutions and computations, the desicion rule is further simplified and finally reduced to [143, sec.IV]

$$\tilde{\mathbf{x}} = \arg\max_{\mathbf{x}} \frac{(\mathbf{y} \cdot \mathbf{x})^2}{||\mathbf{x}||^2}, \tag{3.14}$$

where $\tilde{\mathbf{x}}$ denotes the detection result on subsequence $\mathbf{x}$. We notice that the CSI is not required, something that is crucial to our proposed approach.

3.4.2 The Viterbi-Type Trellis-Search Algorithm

In principle, to implement the above metric, one has to compare M^L possible subsequences and choose the one with the higher metric value. With the use of Viterbi-type trellis-search algorithm, the search complexity can be reduced to a very low level that is independent of the observation window length L [143]. As can be seen from Fig. 3.2, at each time t, the algorithm with the use of (3.14):

- computes the metrics of all the hypothesized sequences arriving at a node,

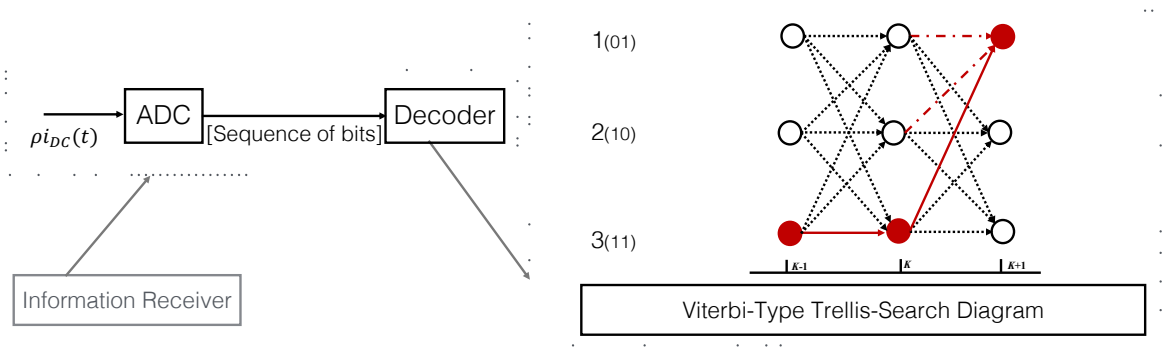

Figure 3.2: Viterbi-type trellis-search diagram for integrated SEQ-MLSD decoder.

- saves the sequence with the higher metric value,
- discards the sequence with the lower metric value.

This is repeated for all paths entering the same node, and the path with the largest metric is saved as the survivor one. As shown with the red solid line in Fig. 3.2, the decision on a symbol is made only when the tails of all survivors have merged at a node. The entire trellis-search algorithm works in the same way as the Viterbi algorithm. Since at each node, only one survivor exists, and at each time point, only M nodes exist, the receiver is required to store the M survivor paths. Furthermore, the received signal is required in order to compute the metric, so the receiver must also store y. Inside the receiver we need to define $M + 1$ memory arrays $P_x^1, P_x^2, \ldots, P_x^M$ and P_y. Arrays $P_x^1, P_x^2, \ldots, P_x^M$ are used to store the M survivor paths, which are sequences of numbers that belong to A. The array P_y is used to store the L most recent received signals, which is a sequence of positive numbers. Another notation used in our implementation is k^*, to denote the time location of the most recent node. Thus, the distance from current time k to the last merge node is $(k - k^*)$. Obviously, $(k - k^*)$ is a random number and from simulation observations, it has been noticed that its mean value is not larger that 3. We can observe that the Viterbi-type trellis-search algorithm can reduce the search complexity to a very low level that is independent of the observation window length L. On the other hand, we find that the search complexity increases significantly while M grows. Specifically, for each symbol detection, one has to compute the decision metrics of all M^2 paths, given that if M power levels used, there are M nodes at each time point and M paths entering each node.

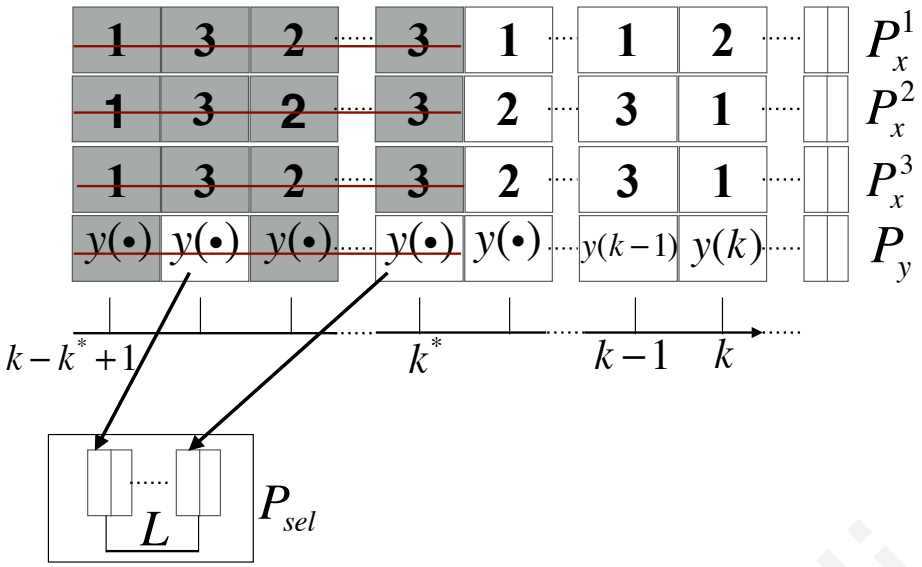

Figure 3.3: Memory arrays with the use of selective-store strategy.

3.4.3 The SS-ST Method

With the use of SS-ST, we enhance our integrated SEQ-MLSD decoder, by overcoming the error floor problem which exists in values of $M > 2$ [144].

As can be seen in Fig. 3.3, we define another array P_{sel}, where we store the L most recent received signals that have been detected to carry the symbol Md, before the last merge node. At each time k, we have $M+1$ arrays $P_x^1, P_x^2, \ldots, P_x^M$ and P_y, which are used to store respectively the M survivor paths and their received signals, for the time space $(k-k^*)$, where k^* denotes the time location of the most recent node, that a decision on a symbol was made. In each survivor path, $(k-k^*)$ ongoing symbols exist. Totally, we denote this length as L_{total}. Now, from equation (3.14), we use the decision metric

$$m(\mathbf{x}(k, L_{\text{total}})) = \frac{(\mathbf{y}(k, L_{\text{total}}) \cdot \mathbf{x}(k, L_{\text{total}}))^2}{||\mathbf{x}(k, L_{\text{total}})||^2}. \tag{3.15}$$

This implementation is called the selective-store strategy. Arrays $P_x^1, P_x^2, \ldots, P_x^M$ and P_y must have the same length and they are only used to save the survivor paths and their received signals after the last merge node. Each decision metric can be divided into two parts. The part before k^* is called the detected part and similarly the part after the k^* is called the ongoing part.

The square root of the numerator of $m(\mathbf{x})$, can be calculated as $(\mathbf{y} \cdot \mathbf{x})_{\text{detected}} + (\mathbf{y} \cdot \mathbf{x})_{\text{ongoing}}$. Where $(\mathbf{y} \cdot \mathbf{x})_{\text{detected}} = (\mathbf{y})_{\text{detected}} \cdot Md$ and $(\mathbf{y})_{\text{detected}}$ is consisted of the most recent L received signals that are stored in P_{sel} and are detected to carry symbol Md before time k^*. Once the M survivor paths merge at some node, we examine

from our decision metric what is the detected symbol. If the detected symbol is the Md, then $(\mathbf{y})_{\text{detected}}$ is refreshed by adding the received signal of time k in array P_{sel}, while at the same time we subtract the oldest one. If not, then we do store the detected symbols but do not add them to P_{sel} array. Both ways, $(\mathbf{y} \cdot \mathbf{x})_{\text{ongoing}}$ is refreshed by substracting the decided symbols. If the two survivor paths have not merged, $(\mathbf{y} \cdot \mathbf{x})_{\text{ongoing}}$ is refreshed by adding the product of the hypothesized symbol and the received signal. Similarly, the denominator can be calculated as $||\mathbf{x}||^2 = ||\mathbf{x}_{\text{detected}}||^2 + ||\mathbf{x}_{\text{ongoing}}||^2$.

In SS-ST the decision metric selectively uses the L most recent received signals that have been detected to carry symbol Md, before the last merge node. Using signals with the highest power to estimate the channel state [143], defines SS-ST as a high efficient technique. Alternatively, without the use of SS-ST, the decision rule is based on the last L immediate received signals. The possibility that a decision on a symbol has not been made, in other words the tails of all survivors have not merged at a node, causes an error floor.

3.4.4 Performance Analysis

The pairwise error probability of a GLRT-MLSD decoder when $L \to \infty$, is given by [143, Eq. (34)]. Specifically, we define the pairwise error probability as the probability of the event that the receiver decides in favour of $\mathbf{x}_j$ given that $\mathbf{x}_i$ is transmitted, $\mathbf{x}_j$ is the only other alternative sequence and for a given channel gain h. This is given by [143]

$$\lim_{L\to\infty} \mathbb{P}(e \mid \mathbf{x} = \mathbf{x}_i, h) = \frac{1}{2}\text{erfc}\left(\frac{hE_{\text{ave}}\sqrt{d}}{2\sqrt{2}\sigma^2}\right). \tag{3.16}$$

In order to proceed with an integration over all the possible values of h, the average pairwise error for adjacent symbols is given by

$$P_{\text{SER\_pair}} = \mathbb{E}\left[\frac{1}{2}\text{erfc}\left(\frac{hE_{\text{ave}}\sqrt{d}}{2\sqrt{2}\sigma^2}\right)\right] = \int_0^\infty \frac{1}{2}\text{erfc}\left(\frac{hE_{\text{ave}}\sqrt{d}}{2\sqrt{2}\sigma^2}\right)\exp(-h)dh. \tag{3.17}$$

As the transmitted symbols and consequently the energy levels M, increase to more than 2, the probability that y will be closer to some other x_j than to x_i, is upper bounded by the sum of the pairwise error probabilities to all the other signals $x_j \neq x_i$. We herein, define the upper bound of the probability of a union of events [145]

$$P_{\text{SER\_seq}} = \frac{1}{M}\sum_{x_i \in A} P(e_{x_i}) \leq \frac{2(M-1)}{M} P_{\text{SER\_pair}}, \tag{3.18}$$

where $P(e_{x_i})$ is the probability of error given that x_i was transmitted.

Conventional Power-Splitting SWIPT Receiver

For the sake of comparison, we additionally provide a SWIPT solution with the use of a separated architecture (conventional decoder) [147]. In this case, the received signal is split in two portions before being converted to a DC signal, while still is in the RF band. The transmitted signal uses PAM, with M constellation points $x_i \in \{\pm\frac{1}{2}d_{\min}, \ldots, \pm\frac{M-1}{2}d_{\min}\}$, where $d_{\min}$ is the minimum distance between two symbols as referred in [145, Ch. 4.3-1]. The average energy per bit transmitted is E_{bavg}, while at the transmitter side a baseband signal $x(t)$ is transmitted as in the case of the integrated receiver. The RF signal is then transmitted over a Rayleigh fading channel with gain h. At the receiver side, a power ratio ρ of the signal, is used for SBS decoding with the use of maximum likelihood. The remaining $1-\rho$ portion is led to an energy receiver, which proceeds to a DC conversion as described in [148] and EH. As in the case of integrated SEQ-MLSD decoder, the noise power from the antenna is omitted. Thus, the average SER over all possible values of h is [145, Eq. (4.3-5)]

$$P_{\text{SER\_PAM}} = \frac{(M-1)}{M}\int_0^{\infty} \text{erfc}\left(\sqrt{\frac{3\log_2 M}{M^2-1}\frac{\rho E_{\text{ave}} h E_{\text{bavg}}}{\sqrt{2}}}\right)\exp(-h)dh,$$

Taking into account the $(1-\rho)$ factor and with the use of (3.6), the energy harvested can be expressed as

$$Q_{\text{PAM}} = (1-\rho)E_{\text{ave}}. \tag{3.19}$$

It is clear that the energy harvested from a conventional decoder (Q_{PAM}) is always less than the energy harvested in a SBS detection scheme with $E_{\text{sens}} = 0$; equality holds for $\rho \to 0$. In the following sections, analysis and simulation results are presented as a benchmark to our proposed integrated SEQ-MLSD decoder.

3.5 Numerical Results

Computer simulations are carried out in order to evaluate the performance of an integrated receiver achieving SWIPT, for the aforementioned non-coherent detection schemes. Specifically, Monte-Carlo simulations are carried out and all the outcomes

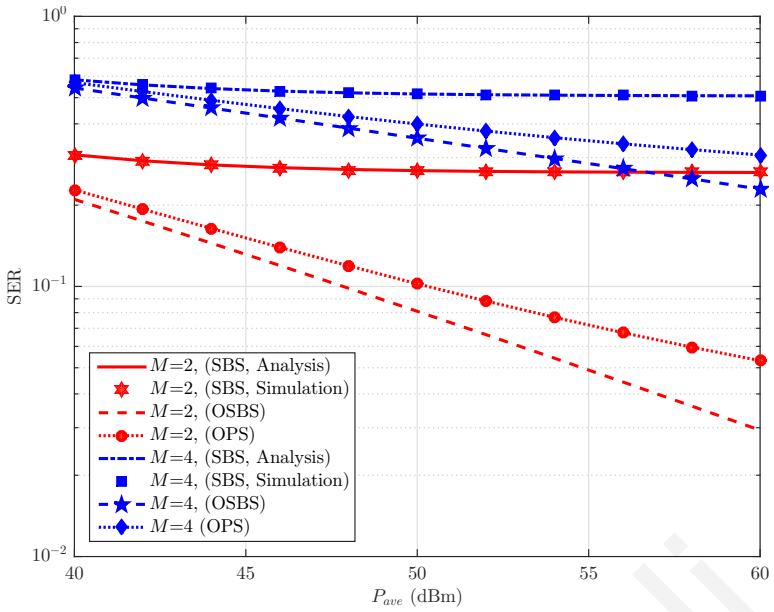

Figure 3.4: Performance of integrated receiver over different number of energy levels M, for all considered schemes; SBS, OSBS and OPS with an indicative example of $E_{\text{sens}} = 0.5E_{\text{ave}}$.

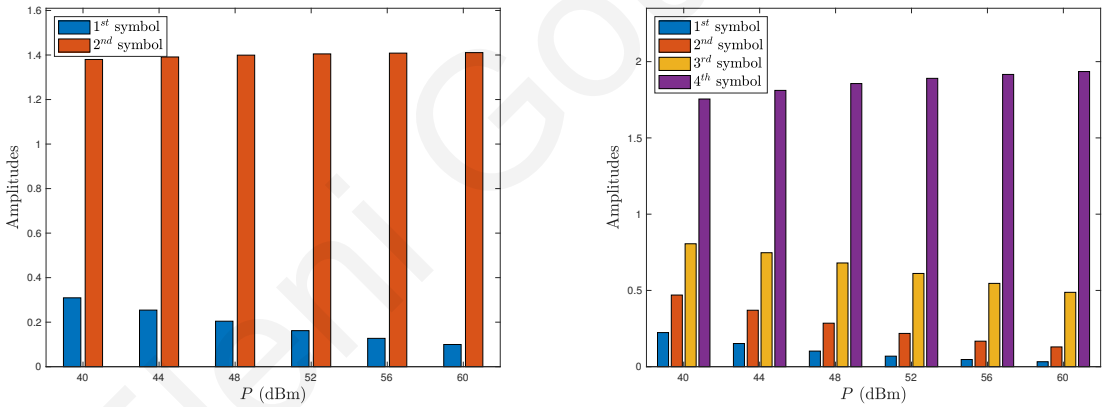

$M = 2$ $M = 4$

Figure 3.5: Amplitude of energy pulses for OSBS.

presented are calculated for 10^5 iterations, while for sequential decoding we assume a coherence length of $N = 500$.

In Fig. 3.4, we present the behavior of SER regarding SBS detection, OSBS, where the pattern of the transmitted energy pulses is optimized and OPS, where a level of power sensitivity is applied at the receiver. As expected, with the increase of E_{ave} and the optimization, the performance of SER is enhanced, while by applying a level of power sensitivity at the receiver, the performance of SER deteriorates.

In Fig. 3.5, we depict the solution of the proposed optimization scheme, OSBS,

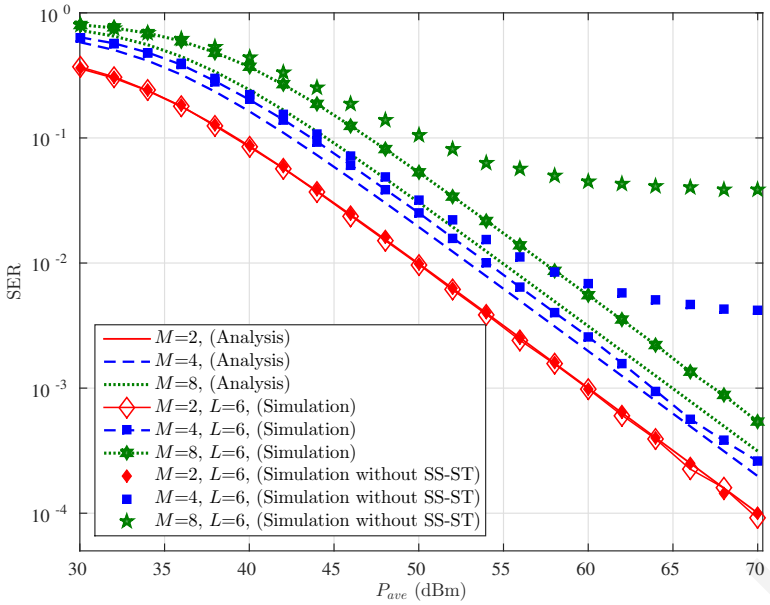

Figure 3.6: Performance of our proposed integrated SEQ-MLSD decoder over different number of energy levels M, sequence length $L = 6$, with and without the use of SS-ST.

for different settings. Specifically, we illustrate the behavior of the energy pulse amplitudes, for $M = 2$ and $M = 4$, as the average transmitted power is increased. It is clearly noticed, that as E_{ave} increases, the distance between the energy pulses also increases, resulting in a reduced pairwise error probability.

In Fig. 3.6, we study the performance of SEQ-MLSD decoder, for a variety of energy levels, with the use of SS-ST and $L = 6$. These results, are compared to a similar system model without the use of SS-ST and to the union bound of the pairwise error probability, as this is described in (3.18). In comparison to the SBS detection in Fig. 3.4, the SER follows the same behavior when E_{ave} and M increase, but with remarkably lower values. One more key observation, is the fact that with the use of SS-ST, the SER is enhanced for the same M energy levels, while at the same time the error floor is eliminated. Furthermore, as the number of energy pulses M increases, due to the existence of more than one pairwise error, the simulation results are compared to the union bound, resulting thus to a higher divergence between simulation and numerical results.

In Figs. 3.7 and 3.8, we compare the performance of our proposed integrated SEQ-MLSD decoder with the conventional one. It can be noticed that for higher values of the average transmitted power e.g. $E_{\text{ave}} = 50$ dBm, our proposed integrated SEQ-MLSD decoder improves remarkably its SER performance. Also, in both figures, it

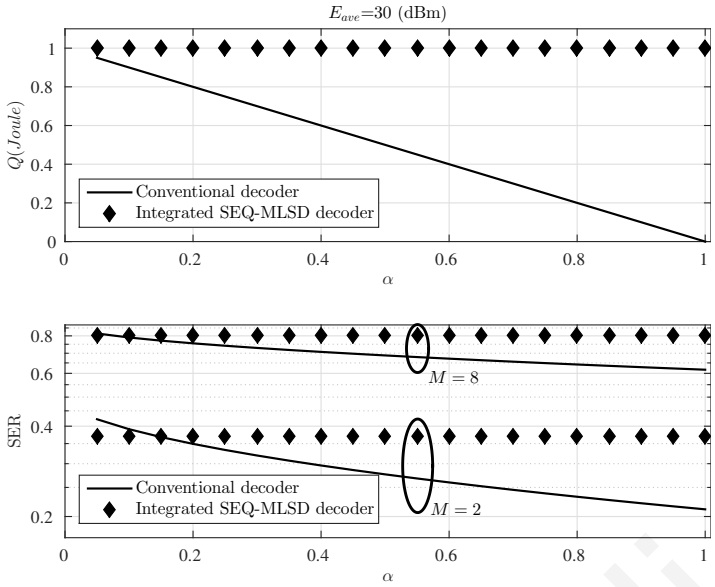

Figure 3.7: Energy harvested and SER versus ρ, for E_{ave} = 30 dBm.

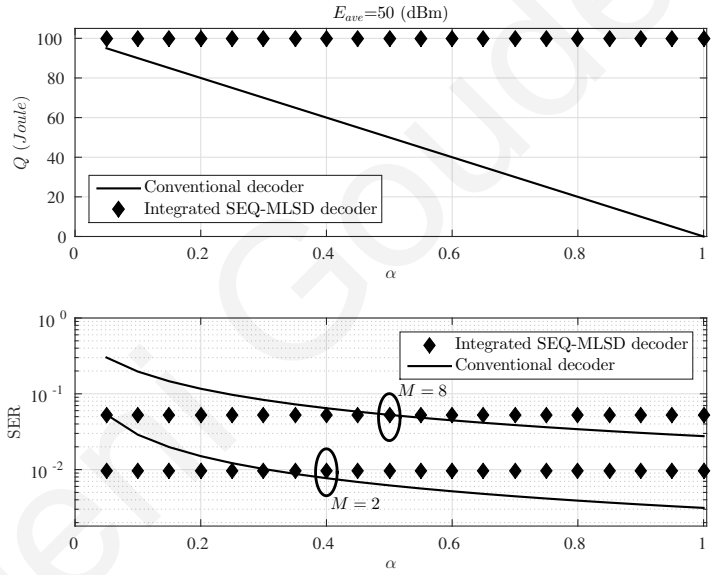

Figure 3.8: Energy harvested and SER versus ρ, for E_{ave} = 50 dBm.

is clear that the conventional decoder achieves a better SER performance than our proposed integrated SEQ-MLSD, for values of $\rho \geq 0.1$, having as a direct consequence the severe degradation of the energy harvested. For values of $\rho < 0.1$, our proposal outperforms the conventional one both in terms of SER and energy harvested.

Furthermore, in Fig. 3.9 we present the behavior of SER related to the sequence length L. It is observed that for low M, the increase of L is not critical, in contrast to higher M values where the increase of L affects positively the SER. It is important to notice that after a point the increase of L does not affect dramatically the results. The value of L should be obtained accordingly to other parameters that affect our

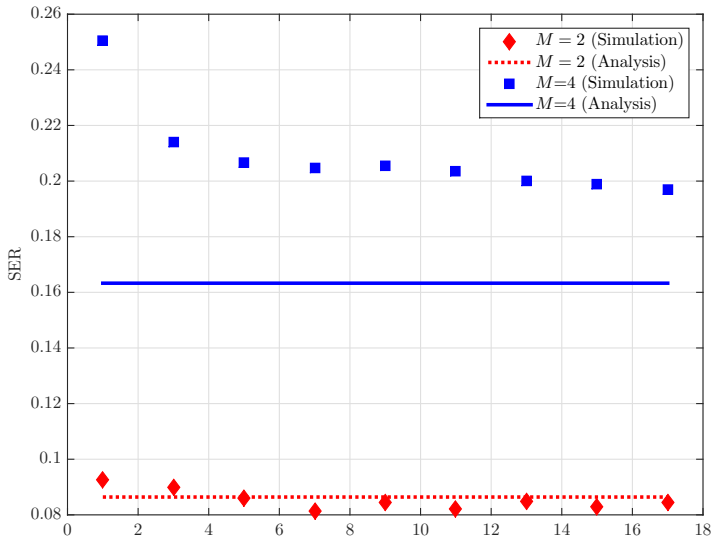

Figure 3.9: Performance of the sequence receiver over different values of L, for P_{ave} = 40dBm.

system, such as the number of energy levels M, the number of symbols transmitted over the channel with coherence length N and the targeted SER for our system.

3.6 Conclusion

In this chapter, we study an integrated SWIPT receiver, with the use of non-coherent detection schemes. We investigate the performance in terms of SER, while with the use of sophisticated techniques we succeed to enhance it without deteriorating the energy harvested. First, we examine a SBS detection scheme; optimization on the pattern of the transmitted energy pulses is carried out, with and without a level of power sensitivity at the receiver. In addition, relying on the coherence time of the channel over N transmitted energy pulses, we exploit sequential detection and propose our integrated SEQ-MLSD decoder. With the use of Viterbi-type trellis search algorithm, we simplify the search complexity of our proposed sequential decoder, while with SS-ST we overcome the error floor problem. Simulation and theoretical results are consistent, corroborating our proposed solution. Our SEQ-MLSD decoder succeeds enhanced SER without degrading the energy harvested, compared to a SBS integrated decoder and a conventional power-splitting SWIPT receiver.

Chapter 4

A Detection Scheme for Integrated SWIPT Receivers with Rectenna Arrays

In this chapter we study SWIPT with the use of an integrated receiver with rectenna arrays. Simulation results along with theoretical analysis, validate the enhanced performance both in terms of ID and EH. The proposed schemes of DC and RF combining at the receiver's side, jointly enhance the performance in terms of ID and EH, while overcome saturation effects. Non-coherent detection is achieved at the same time, differentiating our proposed solutions from the state-of-the-art.

4.1 Introduction

In the new era of the IoT and wireless sensor networks, WPT has been recognized as a promising technology to overcome the critical challenge of supplying power, remotely and wirelessly, to an extensive number of low-power IoT devices [149]. Additionally, a SWIPT system, where RF signals simultaneously convey data and energy, is considered an appealing solution for networks with low-power devices [150]. Some challenges that may provide a practical limitation to SWIPT receivers are distance constraints, EH efficiency, maintaining field strength within safety limits, use of a high frequency for energy transmission and mobility of the sensor nodes [69].

Nonetheless, SWIPT has attracted significant interests in the communication literature. Considering that the rectifying process from RF to DC is similar to an

envelope detection process, there are numerous studies, in order to achieve enhanced performance for simultaneous power and information transfer. Therefore, from the rectified signal at the receiver, several different parameters are detected and exploited. In particular, the authors in [151] study the intermodulation of multi-frequency transmission signal by exploiting both the amplitude and the phase. In [197], a pulse position modulation, where information is encoded in the position of the pulse, is investigated. Finally, in [152] and [153], ID is achieved by detecting the power variations in the received signal adopting a tone-index multisine modulation or enhanced biased amplitude-shift keying, respectively. In the same context, this chapter focuses on how the rectified signal may succeed enhanced ID performance, by exploiting the architecture of the receiver at a basic SWIPT system.

A SWIPT system has two fundamental architectures [17] regarding the receiver. In the first one, the received RF signal is split into two parts, either in the time or in the power domain. One part of the RF signal, is used for information transfer and another part for EH. In the second architecture, an integrated ID and EH circuit is adopted, which as already explained in previous chapters, it can significantly reduce the power consumption of a SWIPT receiver. As such, considering low-power IoT solutions, we herein adopt the architecture of the integrated SWIPT receiver.

Furthermore, targeting enhanced performance for ID and EH, we herein examine two different topologies, with multiple antennas and rectifiers at the receiver's side. In the state-of-the-art, multiple antenna system models are traditionally considered as a common solution for enhanced performance either in terms of ID or EH. There are various studies conducted for exclusively EH technologies, trying to overcome the need of providing enough energy for a reliable EH operation [44], [45]. In addition, in the communication and signal processing literature, it is proven that multiple antenna systems demonstrate a great improvement of performance in terms of spectral efficiency and higher data rates, succeeding diversity or multiplexing gains [154]- [156]. Samewise, SWIPT has also been an area of research for attracting interest on multiple antennas. Several works, as already mentioned in Section 1.2.6, investigate multi-antenna solutions achieving enhanced performances.

In addition, we focus our interest on the rectenna architectures of DC and RF combining. In DC combining, the rectifiers must individually rectify low RF powers, resulting in low conversion efficiency [90]. On the other hand, RF combining channels the combined signal to a single rectifier, which therefore operates on higher

input power levels and achieves higher conversion efficiencies [88]. As such, while the DC combining scheme in most cases surpasses the RF combining scheme, there are operation scenarios where RF scheme is superior. We herein, study both DC and RF combining schemes, differentiating this way from the conventional rectennas solutions.

At the same time, we take into consideration an important area of SWIPT, that the vast majority of research in the RF literature has been devoted to. Specifically, we refer to the design of efficient energy harvesters, so as to increase the RF-to-DC conversion efficiency [157] - [159]. The appropriate choice of models in order to describe the input-output characteristic of a rectenna, is another challenge in the SWIPT technology. Earlier works on SWIPT have been characterized under simplifying assumptions for the rectenna models. Targeting the most realistic approach several models have been proposed, driven by a trade-off between accuracy and tractability [93]. It has been shown, that linear models do not take explicitly into account the effects of rectifier's important characteristics, such as the fact that the RF-to-DC conversion efficiency is a non-linear function of its input signal shape and power. Thus, non-linear EH models are considered as an appropriate choice for a realistic approach. In our study, we adopt a piece-wise linear model [160], which although simple, approximates with accuracy the performance of the RF EH model.

Finally, regarding the ID, since RF to DC rectifying process is similar to envelope detection, we apply non-coherent energy detection technique, where the use of CSI is not required [161]. For the detection of the received signals, there are plenty of mechanisms proposed in the literature. The differences depend on the architecture applied and the modulation scheme adopted. Coherent techniques are a challenging task, since the source needs to periodically send training symbols, which results in increased signaling overhead and processing burden [162]. On the other hand, with the use of non-coherent techniques, such as the one that we adopt, the receiver's complexity is reduced. Specifically, we succeed this with the use of a maximum likelihood-based (ML-based) soft decoder (see Appendix A.6). At the same time, in order to assure low power consumption and modest complexity, a straightforward choice for the modulation scheme, that we also adopt, is binary on-off keying (OOK) [163], [164], which can also serve as a guideline for other modulation schemes.

Overall, in this chapter we study SWIPT and we address the critical issue of enhanced performance in terms of ID and EH, simultaneously. In contrast to the

aforementioned works, we adopt an integrated SWIPT receiver architecture, thus avoiding the RF to baseband conversion, while at the same time exploiting the received rectified DC power signal, both for ID and EH. Differentiating from the traditional rectennas, we adopt multiple receive antennas N, while connecting each one of them to multiple rectifiers, K. By exploiting two different combining schemes at the receiver's side, one in the DC domain and the other in the RF domain, we study the systems' performance, providing enhanced results both in terms of ID and EH. At the same time, we investigate and analyze the effects from the variations of sensitivity and saturation characteristics of rectifiers. Finally, with the use of ML-based soft decoding, we succeed energy detection without the use of CSI [144]. It has to be noticed that our proposed integrated SWIPT receiver with rectenna arrays, could be applied to numerous IoT applications [165], like wearable or implantable devices, RFID bags, wireless sensor nodes etc. [166]. The main contributions of our study are as follows:

- We show that DC combining scheme surpasses the RF combining, in terms of ID. Though, it has to be noticed that the decoding complexity in the DC combining scheme is exponentially increasing with the number of receive antennas, $(2K+1)^N$, while in the RF combining scheme is proportional to the number of rectifiers, which is equal to $2K+1$. On the other hand, the RF combining scheme is superior to the DC, regarding the EH, specifically when referring to low power regime. Furthermore, as the number of antennas and rectifiers increases, the performance is enhanced for both schemes in terms of ID and EH as expected.

- In addition, by considering some special cases of the proposed schemes, we explore the system behavior. Specifically, for the simple case of multiple antennas and only one rectifier, i.e. $N, K = 1$, it is shown that DC combining scheme lags behind in terms of SER for ID, compared to RF combining. This is specifically referring to low ranges of average transmitted power, while it is eliminated as the average transmitted power increases.

- Furthermore, comparing the case of one receive antenna with multiple rectifiers, i.e. $N = 1, K$, towards the case of multiple antennas with one rectifier i.e. $N, K = 1$, we show that the increase in the number of antennas enhances more the system performance in terms of EH, compared to the increase of the

Table 4.1: Summary of Notation for Chapter 4

Notation	Description	Notation	Description
N	Total number of antennas at the receiver	P	Average transmitted power
K	Number of activated rectifiers at antenna i	x	OOK symbol
$k_i/k \in [1, K]$	Number of activated rectifiers at DC/RF scheme	h_i	Channel coefficient of antenna i
$u_{\min}$	Sensitivity power level	n_i	Additive white Gaussian noise to antenna i
$u_{\max}$	Saturation power level	$u_i^{\mathrm{DC}}/u^{\mathrm{RF}}$	Received power signal for DC/RF scheme
N_{sen}	Number of antennas in the sensitivity area	$y(u_i^{\mathrm{DC}})/y(u^{\mathrm{RF}})$	Output from k_i/k activated rectifier at DC/RF scheme
α	Conversion efficiency from RF to DC	ρ	Split power ratio for ID
N_{L}	Number of antennas in the linear area	$f(u_i^{\mathrm{DC}})/f(u^{\mathrm{RF}})$	Probability density function of $u_i^{\mathrm{DC}}/u^{\mathrm{RF}}$
N_{sat1}	Number of antennas in the saturation area	$\lambda_x^{\mathrm{DC}}/\lambda_x^{\mathrm{RF}}$	Rate parameter of exponentially distributed $u_i^{\mathrm{DC}}/u^{\mathrm{RF}}$
N_{sat2}	Number of antennas in the saturation area for $s_i = K$	z	Sum of u_{l_i}'s
L	Set of antennas in linear area with $l_i \in [1, K]$	C_m	Combinations of antennas based on their ordering
S	Set of antennas in saturation area with $s_i \in [1, K-1]$	M	Number of tuples whose sum equals to N

rectifiers, both for DC and RF combining scheme. The same applies for the performance of the ID in terms of SER, for low ranges of P. Though, as the average transmitted power increases the two schemes differentiate. Specifically, in DC combining the performance is the same, either if we increase N or K, while for the RF scheme the performance is bounded by the number of rectifiers.

- Finally, we present numerical results that validate our analysis, while we examine the behavior of our proposed solutions as the sensitivity and saturation levels variate. It is interesting that in low power regime, the RF combining scheme surpasses the DC scheme in terms of ID even for high saturation levels. Furthermore, in RF scheme the variations on the sensitivity and saturation levels do not affect so intensively the SER performance compared to the DC scheme. An asymptotic analysis in high average transmitted power regime is carried out, providing upper and lower bounds for ID and EH, respectively.

4.2 System Model

4.2.1 Integrated Receiver Architecture

We consider a SWIPT system, with a single antenna transmitter at the source, that transmits a baseband signal $x(t)$ with $\mathbb{E}[|x(t)|^2] = 1$. Symbols $x \in [0, 1]$ are transmitted with equal probability. It is herein noted, that the derivations of our analysis could be extended to other modulation schemes suitable for energy detection such as PEM [39]. On the contrary, we herein note that conventional bipolar pulse-amplitude

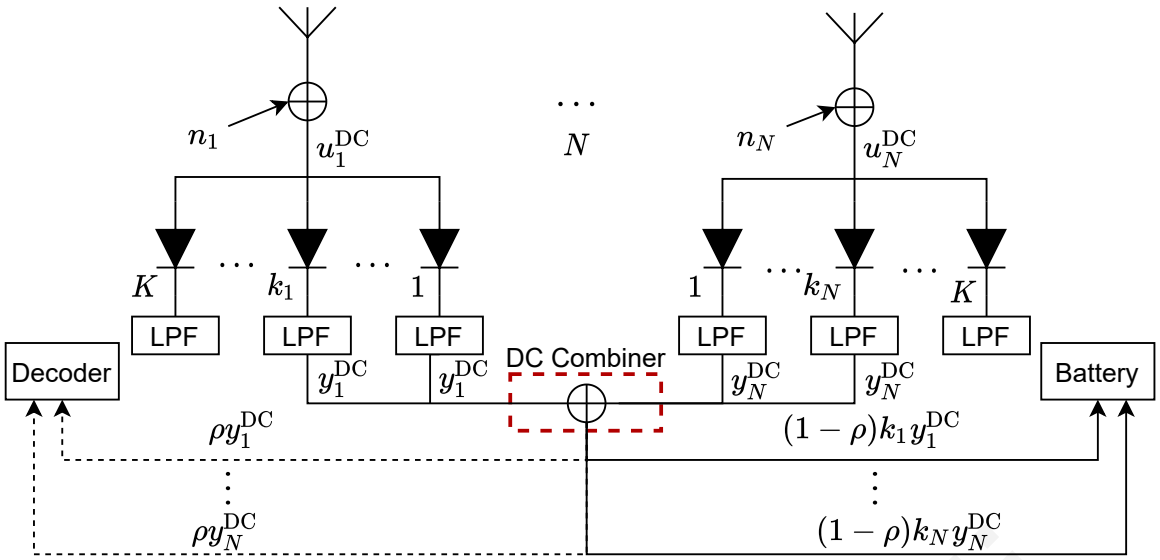

Figure 4.1: Integrated SWIPT receiver, with N receive antennas and K rectifiers, DC combining.

modulation (BPAM) can not be readily used, since transmitted symbols convey the same energy and therefore cannot be distinguished by the integrated receiver.

The baseband signal is then up-converted to generate an RF signal, which is transmitted over a Rayleigh fading channel, with a transmitted power P. At the receiver's side we adopt an integrated SWIPT receiver [20], which consists of multiple receive antennas and rectifiers, N and K, respectively.

The first topology, as seen in Fig. 4.1, proposes a solution with the use of a DC combiner [167]. Specifically, each receive antenna $i \in [1, N]$ is connected to K rectifiers. Therefore, the received RF power signal at each antenna i is calculated as

$$u_i^{\mathrm{DC}} = |\sqrt{P} h_i x + n_i|^2, \tag{4.1}$$

where h_i is the channel coefficient at the i-th antenna, which is modeled as a complex Gaussian random variable with zero mean and unit variance. Furthermore, n_i models the noise as an AWGN with unit variance. From (4.1), we notice that the received RF power signal is exponentially distributed with pdf

$$f(u_i^{\mathrm{DC}}) = \lambda_x^{\mathrm{DC}} e^{-\lambda_x^{\mathrm{DC}} u_i^{\mathrm{DC}}}, \tag{4.2}$$

where λ_x^{DC} denotes the rate parameter and is calculated from

$$\lambda_x^{\mathrm{DC}} = 1/\mathbb{E}(u_i^{\mathrm{DC}}) = 1/(Px^2 + 1). \tag{4.3}$$

As such we herein define $\lambda_0^{\mathrm{DC}} = 1$ and $\lambda_1^{\mathrm{DC}} = 1/(P+1)$, that are used throughout the paper.

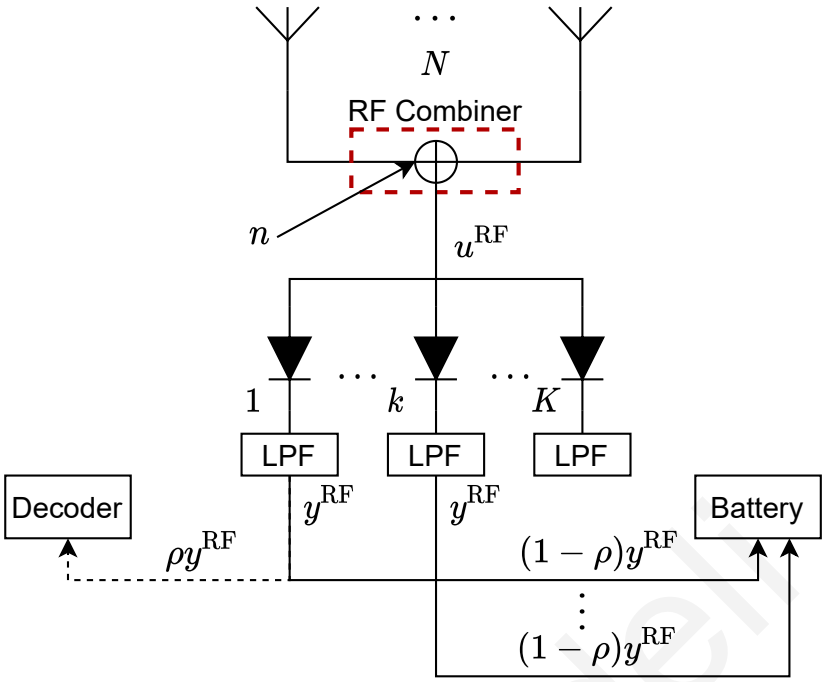

Figure 4.2: Integrated SWIPT receiver, with N receive antennas and K rectifiers, RF combining.

The second topology, as seen in Fig. 4.2, proposes a solution with the use of an RF combiner [168]. We still consider a SIMO solution with an integrated SWIPT receiver. Similarly, we assume N receive antennas, while the difference is that the received signals are combined in the RF domain and not in the DC. Specifically, the received RF signals from the N antennas are summed with the use of an RF combiner and then channeled to K rectifiers. The relative power signal is calculated as

$$u^{\mathrm{RF}} = \left| \sqrt{P} \sum_{i=1}^{N} h_i x + n \right|^2, \tag{4.4}$$

where n models the AWGN with unit variance. From (4.4), we notice that the received power signal u^{RF} is exponentially distributed with pdf

$$f(u^{\mathrm{RF}}) = \lambda_x^{\mathrm{RF}} e^{-\lambda_x^{\mathrm{RF}} u^{\mathrm{RF}}}, \tag{4.5}$$

where λ_x^{RF} denotes the rate parameter and is calculated from

$$\lambda_x^{\mathrm{RF}} = 1/\mathbb{E}(u^{\mathrm{RF}}) = 1/(PNx^2 + 1). \tag{4.6}$$

As such we herein define $\lambda_0^{\mathrm{RF}} = 1$ and $\lambda_1^{\mathrm{RF}} = 1/(PN + 1)$.

4.2.2 RF-to-DC Rectenna Model

For both proposed topologies, we assume that all the rectifiers exhibit the same characteristics. Specifically, we consider two power levels, $u_{\min}$ and $u_{\max}$, that denote the sensitivity and saturation level of each rectifier, respectively. In case the RF power signal channeled to a rectifier is less than $u_{\min}$, then the rectification circuit is not activated. On the other hand, if it is higher than $u_{\max}$, then it reaches the saturation area, where the DC output is maximized. Over the interval $u_{\min}$ and $u_{\max}$, the activated rectifier is in the linear region, where the DC output is linearly increased with the input power. The model adopted, in order to describe the above non-linearity between the RF power signal and the DC output, is the constant-linear-constant (CLC) model [160].

With the use of multiple rectifiers, for both proposed schemes, we target to enhance the output DC signal. Specifically, by taking into consideration the proposed solution in Fig. 4.1, the received RF signal at each antenna i, u_i^{DC}, is led to the K rectifiers. Depending on the power of the received signal, an optimum number of rectifiers, k_i, is activated, thus overcoming the saturation effect and harvesting more energy, compared to a single rectenna solution. Based on the CLC model adopted, the DC output might be in the sensitivity, linear or saturation area, and is calculated respectively as

$$y_i^{\mathrm{DC}} = 0, \tag{4.7}$$

$$y_i^{\mathrm{DC}} = \alpha\left(\frac{u_i^{\mathrm{DC}}}{k_i} - u_{\min}\right), \tag{4.8}$$

$$y_i^{\mathrm{DC}} = y_{sat}, \tag{4.9}$$

where parameter α denotes the conversion efficiency and ranges between $(0, 1]$, while $y_{sat} = \alpha(u_{\max} - u_{\min})$.

Following the same steps as described above and by considering the second proposed solution with the RF combiner, Fig. 4.2, we calculate accordingly the relevant DC output. Specifically, we denote it as y^{RF} and is given from (4.7), (4.8) and (4.9), by substituting the received power signal u_i^{DC} with u^{RF}, as calculated in (4.4). Finally, for this scheme we denote the activated rectifiers with $k \in [0, 1]$.

4.2.3 Decoding Model

In the conventional SWIPT architecture schemes, the received RF signal is firstly split into the power or time domain and then channeled for ID and EH. On the contrary, in the integrated SWIPT architecture that we adopt, the received signal is fully converted from RF to DC and then split into two streams for ID and EH. Specifically, the split power ratio is ρ for ID and $1-\rho$ for EH. Furthermore, in order to reduce the energy requirements for the symbol detection and jointly maximize the power split for EH, we consider that $\rho \to 0$ [20]. As such, since it takes an infinitely small value, we do not consider it in the analysis of SER and EH in the following sections of this chapter.

4.2.3.1 DC Combiner

As seen in Fig. 4.1, the DC outputs from the activated rectifiers at each antenna i, i.e. $k_i y_i^{\mathrm{DC}}$, are channeled to the DC combiner. Afterwards, the decoder in order to optimally combine and decide on the transmitted symbol x, samples a small portion of the DC output from one activated rectifier at each antenna i, i.e. ρy_i^{DC}. This is due to the fact that the received RF signal at each antenna i is equally split to the rectifiers, which exhibit the same characteristics. Therefore, the k_i DC outputs from an antenna i are identical. At the same time, the battery is charged with the remaining DC outputs from all the activated rectifiers k_i, at each antenna i. i.e. $\sum_{i=1}^{N}(1-\rho)k_i y_i^{\mathrm{DC}}$.

The optimum decision of the decoder is based on energy detection, avoiding the knowledge of CSI and is calculated with the use of a ML-based soft decoder. In contrary to a hard decision decoder, the optimum decision is taken by considering the DC outputs from all N antennas and finally deciding based on the overall maximum likelihood of the transmitted symbol x. On the other hand, with the use of a hard decoder, the decision on the transmitted symbol is estimated independently, with the use of ML, at the output of each antenna and the final decision rule is based on the majority of estimated symbols $\tilde{x}$.

Therefore, in this chapter the optimum decision rule, which is calculated with the use of a ML-based soft decoder, is based on the observation vector $\mathbf{y}^{\mathrm{DC}}$ and the symbol that yields the maximum conditioned density $f(\mathbf{y}|x)$ is selected

$$\tilde{x} = \underset{x\in(0,1)}{\operatorname{argmax}}\, f(\mathbf{y}|x), \tag{4.10}$$

where $\mathbf{y}$ is a $N \times 1$ vector, denoting the DC outputs from all the N receive antennas, given that x is transmitted. Since noise is independent between different receive antennas, the distribution $f(\mathbf{y}|x)$ can be factored like

$$f(\mathbf{y}|x) = \prod_{i=1}^{N} f\left(y_i^{\mathrm{DC}}|x\right), \tag{4.11}$$

where for $f\left(y_i^{\mathrm{DC}}|x\right)$ we recognize the following cases.

Firstly, for the sensitivity area where $y_i^{\mathrm{DC}} = 0$ and $k_i = 0$, with the use of (4.2) and (4.7), we have

$$f(y_i^{\mathrm{DC}}) = \left(1 - e^{-\lambda_x^{\mathrm{DC}} u_{\min}}\right)\delta(y_i^{\mathrm{DC}}). \tag{4.12}$$

Secondly, for the linear area, where $0 < y_i^{\mathrm{DC}} < y_{sat}$ and $k_i \in [1, K]$, with the use of (4.2) and (4.8), we have

$$f(y_i^{\mathrm{DC}}) = \lambda_x^{\mathrm{DC}} e^{-\lambda_x^{\mathrm{DC}} k_i \left(\frac{y_i^{\mathrm{DC}}}{\alpha} + u_{\min}\right)}. \tag{4.13}$$

Furthermore, for the saturation area where $y_i^{\mathrm{DC}} = y_{sat}$ with the use of (4.2) and (4.9), we consider two cases depending on the number of activated rectifiers

$$f(y_i^{\mathrm{DC}}) = \begin{cases} e^{-\lambda_x^{\mathrm{DC}} k_i u_{\max}}(1 - e^{-\lambda_x^{\mathrm{DC}} u_{\min}})\delta\left(y_i^{\mathrm{DC}} - y_{sat}\right), & \text{if } k_i \in [1, K), \\ e^{-\lambda_x^{\mathrm{DC}} K u_{\max}}\delta\left(y_i^{\mathrm{DC}} - y_{sat}\right), & \text{if } k_i = K. \end{cases} \tag{4.14}$$

Therefore, the final decision on the transmitted symbol is based on the following criterion

$$\prod_{i=1}^{N} f\left(y_i^{\mathrm{DC}}|0\right) \underset{\tilde{x}=1}{\overset{\tilde{x}=0}{\gtrless}} \prod_{i=1}^{N} f\left(y_i^{\mathrm{DC}}|1\right). \tag{4.15}$$

4.2.3.2 RF Combiner

As seen in Fig. 4.2, the decoding complexity for the RF combiner is lower, since the decoder needs to sample only a small portion of the DC output from only one activated rectifier. On the other hand, the battery is charged with the remaining DC outputs from all the activated rectifiers, i.e. $(1-\rho)ky^{\mathrm{RF}}$. Similarly to the DC combining scheme, by following the same steps, the optimum decision rule is calculated as

$$f(y^{\mathrm{RF}}|0) \underset{\tilde{x}=1}{\overset{\tilde{x}=0}{\gtrless}} f(y^{\mathrm{RF}}|1), \tag{4.16}$$

where $f(y^{\mathrm{RF}}|x)$ can be easily derived from (4.5), (4.7), (4.8) and (4.9) considering the same methodology as in DC combiner.

4.3 Symbol Error Rate Analysis

In this section, we study the performance of the integrated SWIPT receiver for the ID, in terms of SER.

4.3.1 DC Combiner

In order to proceed with the analysis, we have to take into consideration that the number of activated rectifiers depends on the received RF power signal. As such, we herein calculate the optimum number of the activated rectifiers for the DC combiner at each receive antenna i, following the steps from [169].

Firstly, taking into consideration that k_i is the optimum number of activated rectifiers, the received RF power signal, u_i^{DC}, should overpass the sensitivity level, $u_{\min}$, for all of them i.e.

$$u_i^{\mathrm{DC}} > k_i u_{\min}. \tag{4.17}$$

Furthermore, having k_i activated rectifiers should result in increased DC output, compared to the maximum DC output that can be achieved by $k_i - 1$ activated rectifiers, i.e. when in the saturation area. Therefore

$$k_i \alpha\left(\frac{u_i^{\mathrm{DC}}}{k_i} - u_{\min}\right) > (k_i - 1) y_{sat}. \tag{4.18}$$

On the other hand, in order to avoid activating more than k_i rectifiers, we should also consider the following condition. The maximum DC output that can be achieved by k_i activated rectifiers, i.e. when in the saturation area, should be higher compared to the DC output of having $k_i + 1$ activated rectifiers. As such

$$k_i y_{sat} \geq (k_i + 1)\alpha\left(\frac{u_i^{\mathrm{DC}}}{k_i + 1} - u_{\min}\right). \tag{4.19}$$

Consequently, the optimum number of activated rectifiers, is given by

$$k_i = \left\lceil \frac{u_i^{\mathrm{DC}} - u_{\min}}{u_{\max}} \right\rceil. \tag{4.20}$$

From the above and by taking into consideration the topology in Fig. 4.1, as well as (4.7), (4.8) and (4.9), we conclude that the received power signal at each antenna i, activates k_i rectifiers, whose DC output is either in the sensitivity, the linear or the saturation area.

Considering that the proposed system model consists of N antennas each one connected to K rectifiers, we herein make the following assumption. We accept that

the received power signal at N_{sen} out of N antennas, is less than the sensitivity level, thus not activating any rectifiers, i.e. $k_i = 0$. On the other hand, at N_{L} out of N antennas the received power signal results in activating $k_{l_i} \in [1, K]$ rectifiers, with DC output belonging in the linear area. Finally, N_{sat1} and N_{sat2} out of N antennas, have $k_{s_i} \in [1, K-1]$ and $k_{s_i} = K$ activated rectifiers, respectively, in the saturation area. Therefore, in the following Theorem we calculate the relative probability, given that x was transmitted and considering that the DC outputs from the N antennas are independent to each other.

Theorem 1. *The probability regarding the DC outputs from N receive antennas, given that x was transmitted, is given as*

$$P_N(x) = e^{-\lambda_x^{\text{DC}} u_{\max}\left(KN_{\text{sat2}} + \sum_{l_i}^{N_{\text{L}}} k_{l_i} + \sum_{s_i=1}^{N_{\text{sat1}}} k_{s_i}\right)} \times \left(e^{-\lambda_x^{\text{DC}}(u_{\min} - u_{\max})} - 1\right)\left(1 - e^{-\lambda_x^{\text{DC}} u_{\min}}\right)^{(N_{\text{sen}}+1)}, \quad (4.21)$$

where λ_x^{DC} *is given from* (4.3).

Proof. See Appendix B.2. □

In order to calculate the total probability of DC outputs from the N antennas and K rectifiers, we need also to take into consideration the ordering of the antennas whose DC outputs belong to the sensitivity, linear and saturation areas. As such, we herein introduce the antenna set $L = (l_1, l_2, \cdots, l_{N_{\text{L}}})$, which indicates the N_{L} out of the N antennas, whose DC outputs are in the linear area with $k_{l_i} \in [1, K]$ activated rectifiers. Likewise, $S = (s_1, s_2, \cdots, s_{N_{\text{sat1}}})$ indicates the antenna set for the N_{sat1} out of the N antennas that their DC outputs are in the saturation area, with $k_{s_i} \in [1, K)$ activated rectifiers. Therefore, we herein calculate variable C_m as follows

$$C_m = \binom{N}{N_{\text{sen}}}\binom{N - N_{\text{sen}}}{N_{\text{L}}}\binom{N - N_{\text{sen}} - N_{\text{L}}}{N_{sat1}}\binom{N - N_{\text{sen}} - N_{\text{L}} - N_{\text{sat1}}}{N_{\text{sat2}}}. \quad (4.22)$$

Furthermore, we need to consider all possible combinations of N_{sen}, N_{L}, N_{sat1} and N_{sat2}, given that their sum is equal to N and N_{sen}, N_{L}, N_{sat1}, $N_{\text{sat2}} \in [0, N]$. This is derived by applying the mathematical technique of stars and bars [170] for the pair of N antennas and K rectifiers as follows

$$M = \binom{N + 2K}{2K} = \frac{(N + 2K)!}{N!(2K)!}. \quad (4.23)$$

In order to proceed our analysis with the derivation of the total probability or error, we herein need to consider the ML criterion in (4.15). Therefore, with the

appropriate calculations we have

$$\left(\lambda_1^{\mathrm{DC}}-\lambda_0^{\mathrm{DC}}\right)\sum_{l_i=1}^{N_{\mathrm{L}}}u_{l_i}^{\mathrm{DC}}\underset{\tilde{x}=1}{\overset{\tilde{x}=0}{\gtrless}}+\left(\lambda_0^{\mathrm{DC}}-\lambda_1^{\mathrm{DC}}\right)u_{\max}\sum_{k_{s_i}=1}^{N\mathrm{sat1}}k_{s_i}+\left(\lambda_0^{\mathrm{DC}}-\lambda_1^{\mathrm{DC}}\right)u_{\max}KN_{\mathrm{sat2}}+\ln\left(\frac{\lambda_1^{\mathrm{DC}}}{\lambda_0^{\mathrm{DC}}}\right)^{N_{\mathrm{L}}}$$
$$+(N_{\mathrm{sen}}+N_{\mathrm{sat1}})\ln\left(\frac{1-e^{-\lambda_1^{\mathrm{DC}}u_{\min}}}{1-e^{-\lambda_0^{\mathrm{DC}}u_{\min}}}\right). \tag{4.24}$$

Dividing both parts of the inequality with $\lambda_1^{\mathrm{DC}}-\lambda_0^{\mathrm{DC}}$, while taking into consideration that $\lambda_1^{\mathrm{DC}}<\lambda_0^{\mathrm{DC}}$, the ML criterion is expressed as

$$z\underset{\tilde{x}=0}{\overset{\tilde{x}=1}{\gtrless}}t, \tag{4.25}$$

where $z=\sum_{l_i=1}^{N_{\mathrm{L}}}u_{l_i}^{\mathrm{DC}}$ and t equals to the right part of inequality. As such with the use of Theorem 1, (4.22), (4.23) and (4.25) we derive the total probability of error at the following Theorem.

Theorem 2. *The total probability of error for DC combining is calculated as*

$$P_e^{\mathrm{DC}}=\frac{1}{2}\sum_{m=1}^{M}C_m\sum_{x\in(0,1)}\left[P_{e,z}(x)\left(1-e^{-\lambda_x^{\mathrm{DC}}u_{\min}}\right)^{(N_{\mathrm{sen}}+1)}e^{-\lambda_x^{\mathrm{DC}}u_{\max}\left(KN_{\mathrm{sat2}}+\sum_{s_i=1}^{N_{\mathrm{sat1}}}k_{s_i}\right)}\right], \tag{4.26}$$

where

- *if* $z_{\min}<t\leq z_k$*:*

$$P_{e,z}(0)=\frac{e^{-t}}{\Gamma(N_{\mathrm{L}})}\gamma(N_{\mathrm{L}},z_k-t)+\frac{e^{-z_{\max}}}{\Gamma(N_{\mathrm{L}})}\gamma(N_{\mathrm{L}},z_{\max}-z_k), \tag{4.27}$$

and

$$P_{e,z}(1)=\frac{e^{-\lambda_1^{\mathrm{DC}}z_{\min}}}{\Gamma(N_{\mathrm{L}})}\gamma\left(N_{\mathrm{L}},\lambda_1^{\mathrm{DC}}(t-z_{\min})\right), \tag{4.28}$$

- *if* $z_k<t\leq z_{\max}$*:*

$$P_{e,z}(0)=\frac{e^{-z_{\max}}}{\Gamma(N_{\mathrm{L}})}\gamma(N_{\mathrm{L}},z_{\max}-t), \tag{4.29}$$

and

$$P_{e,z}(1)=\frac{e^{-\lambda_1^{\mathrm{DC}}z_{\min}}}{\Gamma(N_{\mathrm{L}})}\gamma\left(N_{\mathrm{L}},\lambda_1^{\mathrm{DC}}(z_k-z_{\min})\right)+\frac{e^{-\lambda_1^{\mathrm{DC}}t}}{\Gamma(N_{\mathrm{L}})}\gamma\left(N_{\mathrm{L}},\lambda_1^{\mathrm{DC}}(t-z_k)\right). \tag{4.30}$$

.

Proof. See Appendix B.3. □

One can easily note, that the decoding complexity is equal to $(2K+1)^N$, since the output from an antenna i, might belong either to the sensitivity area or the linear area

with $k_{l_i} \in [1, K]$ activated rectifiers or the saturation area with $k_{s_i} \in [1, K]$ activated rectifiers, while we have to consider N such outputs from all the receive antennas. In order to minimize the complexity, at the general context of critical IoT services, we herein examine two simple scenarios regarding the proposed solution.

First of all, we assume that the system model as seen in Fig. 4.1, consists of N antennas, each one connected only to one rectifier i.e. $K = 1$. Specifically, the decoder samples and optimally combines with the use of ML, the DC outputs from N rectennas. The DC output from each rectenna might be either in the sensitivity, in the linear or the saturation area. Therefore, by considering all the possible combinations for the N rectennas, the decoding complexity is equal to 3^N, which is exponentially increased with the number of antennas. Furthermore, the probability of error is given from Theorem 2, considering that $K = 1$ and $N_{sat1} = 0$.

The second simple scenario that we examine, is the multiple rectifiers scenario. Specifically, we assume that the proposed system model as seen in Fig. 4.1, has only one receive antenna, i.e. $N = 1$, which is connected to multiple, K, rectifiers. As such, the decoder in order to estimate the transmitted symbol x, considers only one DC output. By taking into account that it might be either in the sensitivity, in the linear or the saturation area, the decoding complexity is equal to $2K + 1$, which is linearly increased with the number of rectifiers. The probability of error is given from (2), considering $N = 1$.

4.3.2 RF Combiner

We recall that in this scheme, all the received RF signals from the N antennas are combined and then channeled to the K rectifiers, in order to be converted to DC signal. As seen in Fig. 4.2, the received power signal u^{RF}, is then equally split to K rectifiers. The optimal number of activated rectifiers is denoted as k and is calculated following the exact same methodology as in RF combining scheme. Similarly to the DC combining scenario, the DC output might be either in the sensitivity, the linear or the saturation area.

In order to proceed our analysis with the calculation of the probability of error in terms of SER, we have to consider the ML criterion from (4.16). With the appropriate substitutions and calculations, the ML decision rule follows

$$u^{\mathrm{RF}} \underset{\tilde{x}=0}{\overset{\tilde{x}=1}{\gtrless}} \frac{PN+1}{PN} \ln(PN+1), \tag{4.31}$$

where we set the right part of the inequality equal to z_{RF}. As such, the relative probability of error, follows in the next Theorem.

Theorem 3. *The total probability of error for the proposed system model of RF combining is*

$$P_e^{\mathrm{RF}} = \frac{1}{2}\Bigg[1 - e^{-\lambda_1^{\mathrm{RF}} u_{\min}} + e^{-\lambda_0^{\mathrm{RF}} K u_{\max}} + \sum_{k=1}^{K-1} e^{-\lambda_{\tilde{x}'}^{\mathrm{RF}} k u_{\max}} \left(1 - e^{-\lambda_{\tilde{x}'}^{\mathrm{RF}} u_{\min}}\right) + \sum_{k=1}^{K} e^{-\lambda_0^{\mathrm{RF}} \left(u_{\min} + (k-1) u_{\max}\right)} - K e^{-\lambda_0^{\mathrm{RF}} z_{\mathrm{RF}}} - \sum_{k=1}^{K-1} e^{-\lambda_1^{\mathrm{RF}} k u_{\max}} + (K-1) e^{-\lambda_1^{\mathrm{RF}} z_{\mathrm{RF}}}\Bigg], \tag{4.32}$$

where $\tilde{x}'$ denotes the symbol that was not estimated.

Proof. See Appendix B.4. □

Herein, one can easily notice that the decoding complexity is equal to $2K+1$, since we take into consideration the DC output from one rectifiers, where its output might be either in the sensitivity, the linear or saturation area with $k \in [1, K]$ activated rectifiers. At this point we introduce the simplest solution for the proposed RF combining scheme. In this scenario, we assume that the system model as seen in Fig. 4.2, consists of N antennas, where after combining the received signals in the RF domain, the power signal is channeled to $K = 1$ rectifier. Herein, the decoding complexity is equal to three, which is independent from the number of antennas N. Clearly, the decoding complexity in this scenario is less than the corresponding scenario in DC combining, where the two proposed system models consist of the same number of antennas and rectifiers i.e. N and $K = 1$. The probability of error is given from Theorem 3, considering $K = 1$.

The second simplest scenario that we examine is by assuming that the proposed system model as seen in Fig. 4.2, has only one receive antenna, i.e. $N = 1$ and is connected to multiple, K, rectifiers. One can easily notice, that this scenario is the same with the corresponding scenario of the DC combining scheme. Therefore, this scenario is common for the DC and RF combining schemes.

4.4 Average Energy Harvesting

In this section, we present the average EH, denoted by Q and measured in Joule, for both schemes. The average EH from an antenna i, given that x is transmitted, is calculated by the sum of expected values of the DC outputs, for all the K activated

rectifiers. Therefore

$$Q = \sum_{x\in(0,1)} \mathbb{P}(x)\mathbb{E}[y_i(u_i)] = \frac{1}{2}\sum_{x\in(0,1)} \int_{u_{\min}}^{\infty} y_i(u_i) f(u_i) du_i, \tag{4.33}$$

where we note that the power of AWGN is too weak to be harvested, as such it is omitted. As such in the following two Propositions we calculate the average EH for the DC and RF combining scheme, respectively.

Proposition 1. *For the DC combining scheme the average EH is calculated as*

$$\begin{aligned} Q^{\mathrm{DC}} = \frac{N}{2}\sum_{x\in(0,1)} \Bigg[& K y_{sat} e^{-\lambda_x^{\mathrm{DC}} K u_{\max}} + y_{sat}\Big(1 - e^{-\lambda_x^{\mathrm{DC}} u_{\min}}\Big) \sum_{s_i=1}^{K-1} k_{s_i} e^{-\lambda_x^{\mathrm{DC}} k_{s_i} u_{\max}} \\ & + \frac{1}{\lambda_x^{\mathrm{DC}}} \sum_{l_i=1}^{K} e^{-\lambda_x^{\mathrm{DC}} k_{l_i} u_{\max}} \Big(- \alpha - \lambda_x^{\mathrm{DC}} k_{l_i} y_{sat} - e^{\lambda_x^{\mathrm{DC}}(u_{\max}-u_{\min})}\Big(\lambda_x^{\mathrm{DC}} y_{sat}\Big(1-k_{l_i}\Big) - \alpha\Big)\Big)\Bigg], \end{aligned} \tag{4.34}$$

where we recall that $y_{sat} = \alpha(u_{\max} - u_{\min})$.

Proof. For the DC combining scheme and the calculation of the average EH, we should consider the DC outputs from N antennas. Therefore, by substituting in (4.33) the values of y_i^{DC} from (4.7), (4.8), (4.9) and $f(y_i^{\mathrm{DC}})$ from (4.12), (4.13), (4.14) respectively, (4.34) is proven with the appropriate calculations. □

Proposition 2. *For the RF combining scheme the average EH is calculated as*

$$\begin{aligned} Q^{\mathrm{RF}} = \frac{1}{2}\sum_{x\in(0,1)} \Bigg[& K y_{sat} e^{-\lambda_x^{\mathrm{RF}} K u_{\max}} + y_{sat}\Big(1 - e^{-\lambda_x^{\mathrm{RF}} u_{\min}}\Big) \sum_{s_i=1}^{K-1} k_1 e^{-\lambda_x^{\mathrm{RF}} k_{s_i} u_{\max}} \\ & + \frac{1}{\lambda_x^{\mathrm{RF}}} \sum_{l_i=1}^{K} e^{-\lambda_x^{\mathrm{RF}} k_{l_i} u_{\max}} \Big(- \alpha - \lambda_x^{\mathrm{RF}} k_{l_i} y_{sat} - e^{\lambda_x^{\mathrm{RF}}(u_{\max}-u_{\min})}\Big(\lambda_x^{\mathrm{RF}} y_{sat}\Big(1-k_{l_i}\Big) - \alpha\Big)\Big)\Bigg]. \end{aligned} \tag{4.35}$$

The above proposition is derived similarly to Proposition 1 and so we omit the proof. Furthermore, the average EH for the proposed simple scenarios is given from (4.34) and (4.35), considering that $K = 1$ and $N_{sat1} = 0$ or $N = 1$, accordingly.

4.5 Asymptotic Analysis

In this paragraph, we examine the behavior of our system models asymptotically, in high average transmitted power regime, considering an infinite number of receive antennas N and a large number of rectifiers K.

4.5.1 DC combining

When $P \to \infty$, a lower bound, in terms of SER, is calculated as expressed in the following Corollary.

Corollary 1. *A lower bound, in terms of SER, for the DC combining scheme is derived as follows*

$$\lim_{P\to\infty} P_e^{\mathrm{DC}} = \frac{1}{2} e^{-NKu_{\max}}. \tag{4.36}$$

Proof. For really high values of P, all the available K rectifiers at an antenna i will be activated and reached the saturation area, with probability equal to $\mathbb{P}(Ku_{\max} \leq u_i^{\mathrm{DC}})$, as given from (B.8) in Appendix B.2. This applies for the DC outputs from all N receive antennas. Therefore, $N_{\mathrm{sat2}} = N$, while $N_{\mathrm{sen}} = N_{\mathrm{L}} = N_{\mathrm{sat1}} = 0$ and Theorem 1 results in

$$P_N(x) = \left(\mathbb{P}(Ku_{\max} \leq u_i^{\mathrm{DC}})\right)^N = e^{-\lambda_x^{\mathrm{DC}} Ku_{\max} N}. \tag{4.37}$$

Considering the ML condition from (4.24), with the appropriate substitutions and calculations we see that the estimated transmitted symbol, will always be equal to $\tilde{x} = 1$. As such, the bound for the relative probability of error is

$$\lim_{P\to\infty} P_e^{\mathrm{DC}} = \frac{1}{2} e^{-\lambda_0^{\mathrm{DC}} NKu_{\max}}. \tag{4.38}$$

Considering that $\lambda_0^{\mathrm{DC}} = 1$, the result in (4.36) follows. □

Regarding the EH, for high values of P, we derive an upper bound as expressed in the following Proposition.

Proposition 3. *An upper bound regarding the EH and the DC combining scheme is derived as follows*

$$\begin{aligned}\lim_{P\to\infty} Q^{\mathrm{DC}} = \frac{N}{2}\Bigg[& Ky_{sat}(1 + e^{-Ku_{\max}}) + y_{sat}\Big(1 - e^{-u_{\min}}\Big)\sum_{s_i=1}^{K-1} k_{s_i} e^{-k_{s_i} u_{\max}} \\ & - \sum_{l_i=1}^{K} e^{-k_{l_i} u_{\max}}\Big(\alpha + k_{l_i} y_{sat} + e^{(u_{\max}-u_{\min})}\Big(y_{sat}\Big(1 - k_{l_i}\Big) - \alpha\Big)\Big)\Bigg].\end{aligned} \tag{4.39}$$

Proof. For $P \to \infty$, the rate parameter given that $x = 1$, results in $\lambda_1^{\mathrm{DC}} = 0$. By taking into consideration the property that for small values of x applies that $\exp(-x) \approx 1 - x$, then (4.39) is derived directly from (4.34). □

The relative bounds for the simple scenarios of $N = 1$ and $K = 1$, are obtained from (4.36) and from (4.39), by considering $N = 1$ and $K = 1$, respectively.

Furthermore, we herein note, that when the number of receive antennas N, tends asymptotically to infinity, the performance of ID and EH, will asymptotically tend to zero and infinity, respectively. This can be easily derived from Theorem 2 and Proposition 1, considering that for $N \to \infty$, then also N_{sen}, N_{L}, N_{sat1} and N_{sat2} tend asymptotically to infinity. Finally, considering a large number of K rectifiers at each receive antenna, will result in a DC output that will never reach the saturation area. As such, the ID could be calculated from Theorem 2, considering $N_{\text{sat2}} = 0$. Similarly, the EH could be calculated from Proposition 1, by omitting the term of $Ky_{\text{sat}}e^{-\lambda_x^{\text{DC}} K u_{\max}}$.

4.5.2 RF combining

For high values of P, as in the DC combining scheme, a lower bound in terms of SER is calculated, while for the EH an upper bound is derived.

Remark 1: For $P \to \infty$, the total probability of error, in terms of SER, for the RF combining scheme converges to

$$\lim_{P\to\infty} P_e^{\text{RF}} = \frac{1}{2} e^{-K u_{\max}}. \tag{4.40}$$

Proof. As in the DC combining scheme, due to the high average received power, all the available K rectifiers will be activated in the saturation area. Therefore, following the same steps as in Corollary 1, (4.40) results directly from (4.36) by susbtituting $N = 1$. □

One can easily note, that the performance of the RF combining scheme in terms of SER, increases as the number of rectifiers K increase and is independent from the number of receive antennas N.

Remark 2: For $P \to \infty$, the average EH for the RF combining scheme converges to

$$\begin{aligned} Q_{bnd}^{\text{RF}} = \frac{1}{2}\Bigg[& K y_{sat}(1 + e^{-K u_{\max}}) + y_{sat}\Big(1 - e^{-u_{\min}}\Big) \sum_{k=1}^{K-1} k e^{-k u_{\max}} \\ & - \sum_{k=1}^{K} e^{-k u_{\max}} \Big(\alpha + k y_{sat} + e^{(u_{\max} - u_{\min})} \Big(y_{sat}\Big(1 - k\Big) - \alpha \Big) \Big) \Bigg], \end{aligned} \tag{4.41}$$

where result follows from (4.35), considering that $\lambda_1^{\text{DC}} = 0$ and following the same steps as in Proposition 3.

Table 4.2: Simulation Parameters

Description	**Notation & Value**	**Description**	**Notation & Value**
Sensitivity power level	$u_{\min} = 0.1$	Saturation power level	$u_{\max} = 2$
Conversion efficiency from RF to DC	$\alpha = 0.7$ [171]	Monte-Carlo	10^6 iterations
Number of receive antennas	$N = 2$	Number of rectifiers	$K = 2$

From (4.39) and (4.41), we can easily notice that

$$Q_{bnd}^{\mathrm{RF}} = \frac{Q_{bnd}^{\mathrm{DC}}}{N}. \tag{4.42}$$

The relative bounds for the scenarios of $K = 1$ and $N = 1$, are obtained from (4.40) and from (4.41), by considering $K = 1$ and $N = 1$, respectively.

Furthermore, we herein note that considering an infinite number of receive antennas results in the same asymptotic analysis as if $P \to \infty$, both for ID and EH. Finally, for a large number of rectifiers, K, the DC output will never reach the saturation area. Therefore, from Theorem 3 we could calculate the ID, by omitting the term of $\mathbb{P}(u^{\mathrm{RF}} > Ku_{\max}|x = 0) = e^{-\lambda_0^{\mathrm{RF}} Ku_{\max}}$. Following the same approach, the EH could be calculated from Proposition 2, by omitting the term of $Ky_{\mathrm{sat}}e^{-\lambda_x^{\mathrm{RF}} Ku_{\max}}$.

4.6 Numerical Results

In this section, we provide numerical results and illustrate the performance of our system model. Monte-Carlo simulations are carried out and all the outcomes presented are calculated for 10^6 iterations. The main simulation parameters used in the paper, are summarized in Table 4.2.

Fig. 4.3, presents the performance of the integrated SWIPT receiver in terms of SER, considering $N = K = 2$, for DC and RF combining. Furthermore, we illustrate their performance for $N = K = 1$, as the solution with the simplest complexity. Finally, we present the lower bound as calculated from the asymptotic analysis, considering $P \to \infty$. Clearly, enhanced decoding performance is succeeded by increasing N and K. Specifically, when referring to DC combining scheme this results in more samples per symbol, but still the complexity of sampling is not so high with the current state-of-the-art of ADCs [172]. Furthermore, DC combining has an enhanced performance compared to RF combining, for the same number of receive antennas, N, and rectifiers, K.

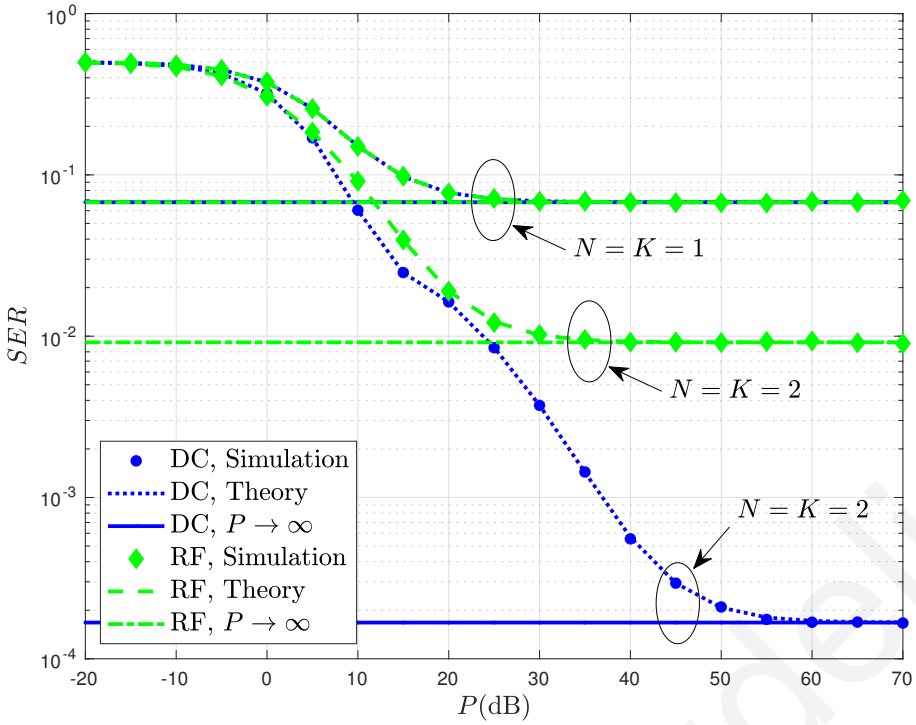

Figure 4.3: SER of the integrated SWIPT receiver, for $N = K = 2$ and $N = 1, K = 1$, for DC and RF combining.

In Fig. 4.4, we illustrate the performance of the system model in terms of EH, for $N = K = 2$, as well as for $N = K = 1$. We notice that the proposed solution for DC combining increases the EH and offers enhanced results compared to RF combining, when referring to high power regime, while this inverses at low power. Furthermore, we see that the EH in the DC combining is $N = 2$ times higher than the EH in the RF combining, for the same number of rectifiers $K = 2$, as asymptotically $P \to \infty$.

In Fig. 4.5 and 4.6, we present the performance of the simple case scenarios, in terms of SER and EH. From Fig. 4.5, one can easily note that the best performance in terms of SER, when $K = 1$, is for the RF scenario with the least decoding complexity, specifically when referring to the low range of transmitted power P, while this is reverted as P increases. On the other hand, for the case of $N = 1$, both RF and DC combining schemes have exactly the same behavior, since the two proposed topologies are the same. Furthemore, for the DC combining scheme we see that the increase in the number of antennas $N = 2, K = 1$, compared to the increase in the number of rectifiers i.e $N = 1, K = 2$, results in better performance in low power regime, while asymptotically perform the same.

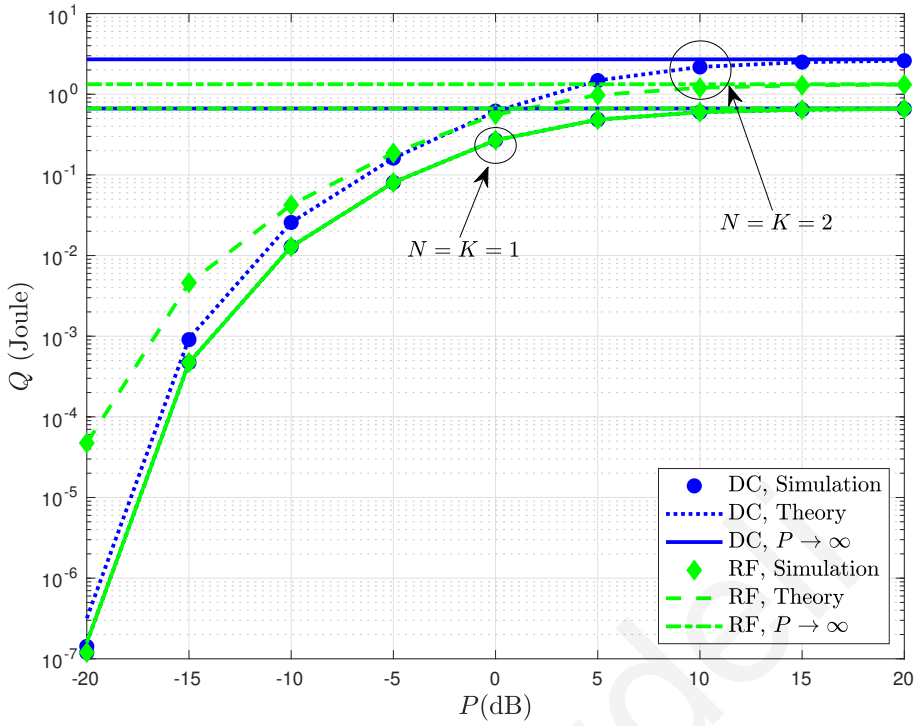

Figure 4.4: EH of the integrated SWIPT receiver, for $N = K = 2$ and $N = 1, K = 1$, for DC and RF combining.

Fig. 4.6 highlights the enhanced performance of the DC combining scheme in terms of EH, when we increase the number of antennas $N = 2, K = 1$ compared to the increase in the number of rectifiers $N = 1, K = 2$, specifically referring to the low power regime. We notice that in the scenario of $N = 2, K = 1$, the EH increases linearly with the number of rectennas, while this is not the case for the case of $N = 1, K = 2$. Furthermore, we observe that the case of $N = 2, K = 1$ in the RF combining scheme has the better performance in low power regime and it is upper bounded by the performance of DC combining, considering $N = K = 1$.

In Fig. 4.7 we illustrate the performance in terms of SER for the DC and RF combining scheme, as per transmitted average power P and power levels $u_{\min}$ and $u_{\max}$. It is interesting that for the DC combining scheme, the SER deteriorates with the increase of sensitivity power level when in low power regime. On the other hand, as P increases and we reach the lower bound of SER, the variation of $u_{\min}$ does not affect the performance. Regarding the variations in the $u_{\max}$, we notice that there is a small range that maximizes the SER, while after that any increase deteriorates the performance, till it reaches the saturation area. For the RF combining scheme, we observe that the variations in $u_{\min}$ and $u_{\max}$ hardly affect the performance of SER. This

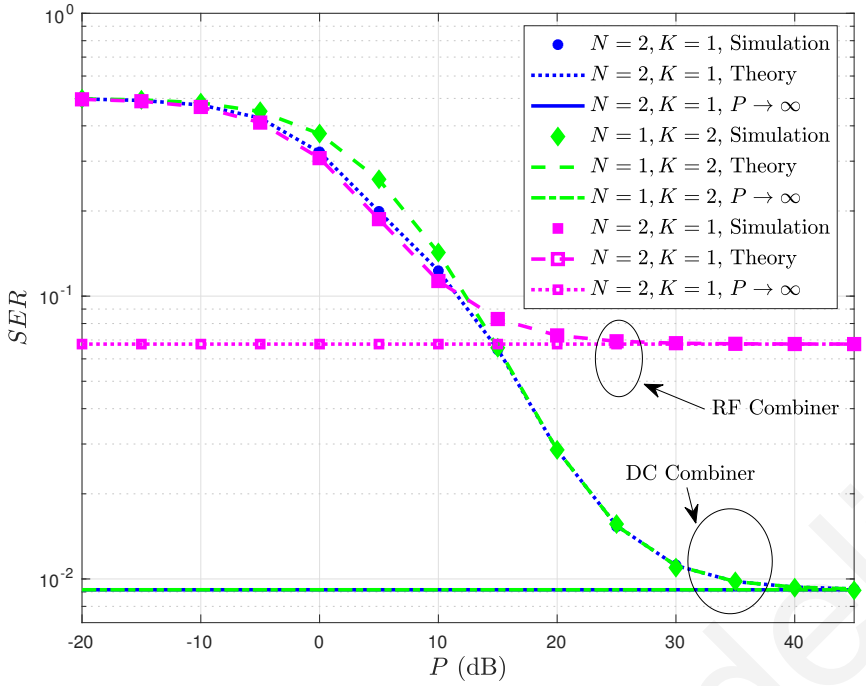

Figure 4.5: SER of the integrated SWIPT receiver, for the simple cases of $N = 1, K = 2$ and $N = 2, K = 1$.

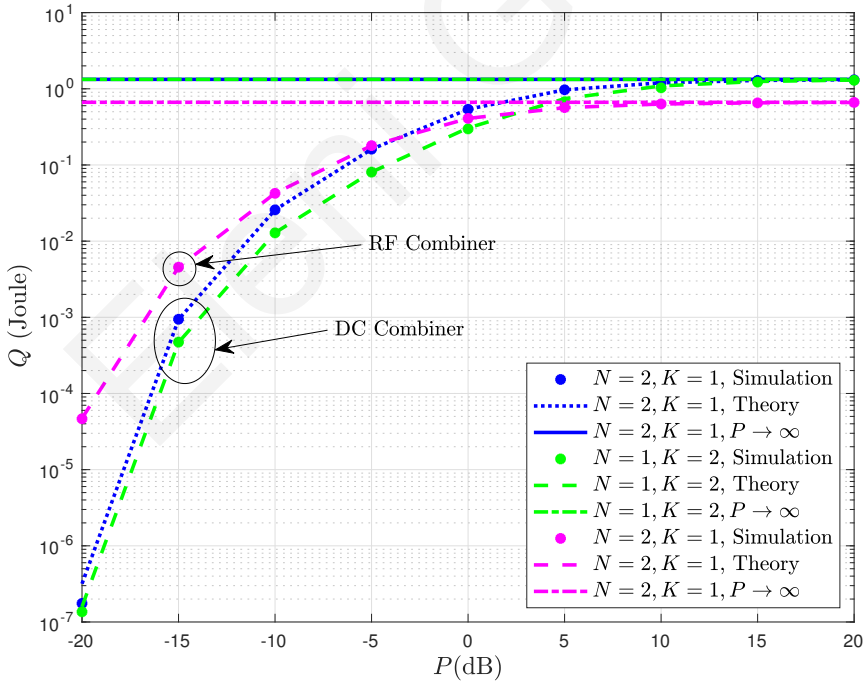

Figure 4.6: EH of the integrated SWIPT receiver, for the simple cases of $N = 1, K = 2$ and $N = 2, K = 1$.

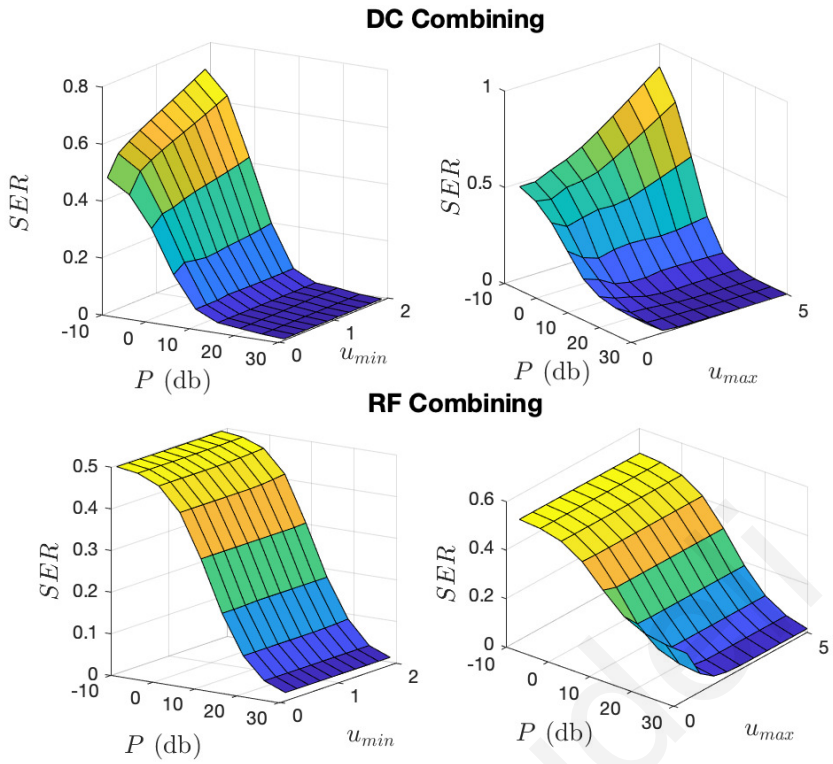

Figure 4.7: Performance DC and RF combining for $N = K = 2$, in terms of SER, P, $u_{\min}$ and $u_{\max}$.

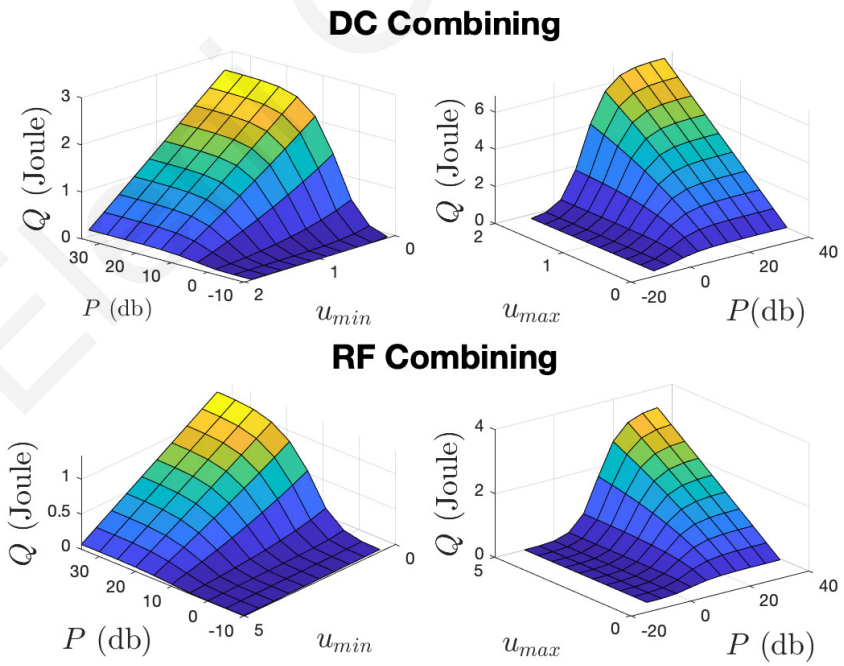

Figure 4.8: Performance DC and RF combining for $N = K = 2$, in terms of Q, P, $u_{\min}$ and $u_{\max}$.

is due to the fact, that the received RF power signal is summed from the N antennas and then channeled to the rectifiers. Finally, compared to the DC combining scheme and for the same power levels, specifically referring to the low regime, it is noticed that for high values of sensitivity and saturation levels the RF combining scheme surpasses the DC combining scheme.

In Fig. 4.8 we present the performance of DC and RF combining scheme, in terms of EH and how this is affected by variation of P, $u_{\min}$ and $u_{\max}$. We can clearly notice that as the transmitted power, P, and the saturation power level, $u_{\max}$, increase, the EH for the DC combining scheme increases as well. On the contrary, for the same levels of average transmitted power P, the increase in the sensitivity power level, $u_{\min}$, affects negatively the EH. Finally, the same behavior is observed for the RF combing scheme, though the EH is less compared to the DC combining scheme, as already noted in Fig. 4.4.

For the comparison with the theoretical model, the circuits for $N = 1$, $K = 1, 2$ were implemented by the lab of antennas and microwaves of Frederick university, who provided us with the experimental results presented in Appendix B.5.

4.7 Conclusion

In this chapter, we study a non-coherent detection scheme for integrated SWIPT receivers. We consider two SIMO topologies with N receive antennas and K rectifiers, examining a DC and RF combining scheme, respectively. The proposed system models, by using a ML-based soft decoding, exploit simultaneously the rectified DC power signal, jointly enhancing the performance of ID and EH. In addition, with the use of a piece-wise linear EH model, we manage to capture the sensitivity and saturation behavior of the rectifiers. In particular it is shown, that for the same number of receive antennas, N, and rectifiers, K, the DC combining scheme surpasses the RF combining scheme, in terms of SER, while this results in increased decoding complexity, $(2K + 1)^N$, compared to the RF scheme, $2K + 1$. Regarding the average EH, DC combing scheme is superior at high power regime while this differentiates at low values of P. Finally, we conduct an asymptotic analysis, providing lower and upper bounds, for the ID and EH, respectively. Simulation and theoretical results are consistent, corroborating our study.

Chapter 5

Spatial modulation-based techniques for backscatter communication systems

In this chapter, we assess the added value of BackCom in 5G IoT technology, by studying spatial modulation-based techniques, applied over a traditional multiple antenna BackCom system. Our target is to exploit the advantages of a bistatic backscatter architecture with the use of sophisticated physical layer tools, provide a general mathematical framework and propose a system model that can be adopted from the majority of next generation IoT applications. Differentiating from the state-of-the-art solutions, we design and study a solution with multiple antennas at the BT, in contrast to conventional solutions with multiple antennas at the source or RN. Our solution is compared to the sophisticated sequential decoder, proposed and presented in Chapter 3.

5.1 Introduction

5G IoT discloses enormous opportunities for connecting small size, low cost, typically battery-powered, and often densely populated devices to perform massive machine-type communications. Billion smart entities (e.g. sensors, actuators) are expected to be deployed worldwide, while traditional battery operated devices will become outdated. Therefore, in order to deal with their energy requirements, new solutions such as devices with extended battery lifetime and devices that are wire-

lessly powered will be evolved [173]. At the same time, all these IoT devices should target to small energy requirements in order to transmit their messages [174]. As such BackCom is gaining popularity as a suitable solution to fulfill these needs.

BackCom systems can be clasified into three major types based on their architecture: monostatic, bistatic and ambient BackCom systems [103]. All the schemes share the same fundamentals. Particularly, a part of the received signal from the RF source, is backscattered to the RN, while the BT can send its data by tuning its antenna impedance to different states. This scheme is known as load modulation and in literature is largely confined to binary, due to hardware constraints. Though higher order modulator designs have been successfully prototyped [175], therefore more than a two-state modulation may be adopted [176]. The rest of the received signal from the RF source, is used by the BT for harvesting energy, thus making it possible to operate exclusively its own integrated circuit or partially support it, in terms of energy required.

On the other hand, by taking into consideration the architecture type, there are some differences. Specifically, in a bistatic communication system, the RF source and the receiver are separated, in contrast to the monostatic architecture where these two are integrated e.g. RFID reader. In the bistatic architecture, the issue of round-trip path loss and near-far problem, may be mitigated, as already referred in Section **??**, due to differentiated distance between the RF source, the BT and the RN. Finally, for the third type of ambient backscatter communication systems [177], the transmitter is separated from the backscatter receiver, but there is no dedicated RF source. Any available and opportunistic ambient source, like TV towers and cellular base stations, may be used as an RF source transmitter.

Regarding the detection method of the modulated signals from the BT to the RN, there are plenty of mechanisms proposed in the literature. The differences depend on the architecture applied, the modulation scheme adopted in the BT and the number of antennas used. More specifically, noncoherent detection is mainly adopted in ambient backscatter communications [178], where the knowledge of CSI at the RN is a challenging task. However, coherent detection may be adopted especially in the bistatic architecture, since the RF sources are most of the time devoted transmitters, that may set no restrictions to communication range and at the same time increase the bit rate [38]. As such, ML detectors can be applied at the RN so as to detect efficiently the received modulated signal [179].

Another characteristic that makes BackCom even more attractive for 5G IoT solutions, is the ability to enhance the BT with multiple antennas. Numerous studies in literature proving the added value of multiple antennas in a BackCom system, are presented in Section 1.2.6. As such, we herein consider multiple antenna techniques that have been proposed and studied in traditional MIMO systems, resulting in enhanced performance and increased spectral efficiency. More specifically, a generalized spatial modulation (GSM) technique, was presented in [180]. In GSM the transmitted information exploits the traditional modulation scheme and the antenna index as an additional source of information. Spatial modulation (SM) technique was first introduced by Mesleh *et al*. [181], [182] and is the simplified case of GSM, for one transmitting antenna at a time instant. The GSM scheme increases the overall spectral efficiency compared to SM, resulting in reduced number of transmit antennas for the same spectral efficiency.

As an evolution to GSM, another spatial modulation-based technique, expanded in time domain, was introduced in [183]. In particular, Alamouti scheme [184] was applied in two out of the multiple transmitting antennas. Alamouti is a simple transmit diversity scheme (see Appendix A.7), without any feedback from the receiver to the transmitter, with small computation complexity and no bandwidth expansion. Taking into consideration, that this coding scheme involves the transmission of multiple copies of the data, diversity gains are achievable for the given number of transmit and receive antennas.

Motivated by the above, in this work, we address two critical features of 5G IoT; wireless powered devices of low power consumption and high data rates. As such, we investigate a BackCom system with a multiple antenna BT. In contrast to the aforementioned works, we consider a bistatic architecture where spatial-modulation based techniques are employed at the BT and coherent detection is considered at the RN. To the best of our knowledge, this problem has not been addressed before in the literature. Recent attempts have been devoted in studying the advantages of spatial modulation-based techniques in BackCom systems, but in different context. More specifically, in [185], the authors study SM technique, over an ambient BackCom system with noncoherent detection. Furthermore, in [186], the GSM technique is applied at the source and not at the BT as we propose, while a cooperative detector based on the framework of sparse Bayesian learning is adopted, over an ambient backscatter architecture.

Our target is to exploit the advantages of a bistatic backscatter architecture with the use of sophisticated physical layer tools, provide a general mathematical framework and propose a system model that can be adopted from the majority of next generation IoT applications. Specifically, the main contributions of our study are as follows:

- With the use of multiple antennas at the BT, we apply sophisticated spatial modulation-based techniques. This enables us to increase the overall system efficiency, which is a key point for a 5G IoT solution. More specifically, with the use of GSM technique, we succeed enhanced performance in terms of SER, while at the same time reduce the number of transmit antennas needed in the BT. Furthermore, we examine the GSMA technique, where the transmitted information symbols are expanded to the time domain. With the use of Alamouti scheme, we succeed transmit diversity and ensure significant improvements in SER performance.

- We derive analytical expressions regarding the pairwise error probability for all the examined techniques, providing tight upper bounds. Furthermore, we asymptotically analyze the performance of our proposed system model, which yields insights to the limits' behavior, similar to [187], while at the same time proves the diversity order of GSM, SM and GSMA. Simulation results validate the enhanced performance of the proposed techniques, emphasizing the strengths of each case.

5.2 System Model & Backscatter Transmission Techniques

In this section, we provide all the details regarding the considered system model; the main mathematical notation related to the system model is summarized in Table 5.1.

5.2.1 Topology and System Design

We study a bistatic BackCom system consisted of an RF source equipped with a single antenna, a BT with L antennas, out of which $L_u \in (1, L)$ are the active

Table 5.1: Summary of Notation for Chapter 5

Notation	Description	Notation	Description
L	Total number of antennas in the BT	L_u	Number of active transmitting antennas in the BT $\in (1, L)$
P	Average transmitted power from the RF source	$\mathbf{F}_\ell$	DBC of the antenna set ℓ
x	M-ary data symbol in GSM & SM	x_1, x_2	M-ary data symbol transmitted in first and second time interval in GSMA
h_{ℓ_i}, g_{ℓ_i}	Forwarded and backscattered channels of the DBC	n	Additive white Gaussian noise
ℓ	Set of active and transmitting antennas in the BT	ℓ_i	Index of the i-th antenna in the antenna combination ℓ
m_μ	Spectral efficiency of $\mu \in$ {GSM, SM and GSMA}	θ	Rotation angle used in GSMA
P_s^μ	Probability of error for $\mu \in$ {GSM and GSMA}	q	Total number of of independent terms in DBC
d_μ	Diversity order for $\mu \in$ {GSM and GSMA}	$\Pr(x \to \hat{x})$	Pairwise error probability
v	Total number of codebooks in GSMA	α	Number of codewords in the $v-1$ codebooks

transmitting antennas at each time instant and a RN, also equipped with a single antenna. A schematic diagram of the considered backscatter network is shown in Fig. 5.1. Furthermore, we are assuming that the antennas at the RF source, the BT and the RN are spaced sufficiently far apart so that fading at each antenna is statistically independent. The RF source which is deployed for the backscatter system, broadcasts a CW signal. The BT will then backscatter a portion of the received signal to the RN, by using appropriate load modulation. More specifically, the BT, actually transmits its own tag information when reflecting the signal, by switching its load impedance between different states. A portion of the CW signal is used by the BT to harvest energy and operate its own integrated circuit.

Dyadic backscatter channel (DBC) is considered in this thesis, as analytically described in [52]. We herein assume that due to deep scattering and obstacles, the direct link between the RF source and the RN is not feasible [188], [189], [190]. Furthermore, in our study we mainly assume the sub-6 GHz band. We consider Rayleigh fading channel, due to its analytical and tractable results. Thus the forwarded and backscattered paths, are represented with independent and identically distributed (i.i.d.) complex Gaussian channel elements, while each element in DBC is drawn from $CN(0, 1)$.

It is worth noting, that all the channels are constant within a channel coherence time, though they may vary independently in different coherence intervals. In our study, we assume that for a specific time instant the load reflection coefficients for all the antennas in the BT, are the same. This results in a simultaneous transmission of a specific data symbol, from all the active transmitting antennas in the BT. Furthermore, for all the considered schemes studied, we assume that the detection at the RN is coherent and ML is adopted[1]. In addition, in our system model we apply element-

[1]To coherently detect the backscattered signal, we assume knowledge of the CSI at the RN, which

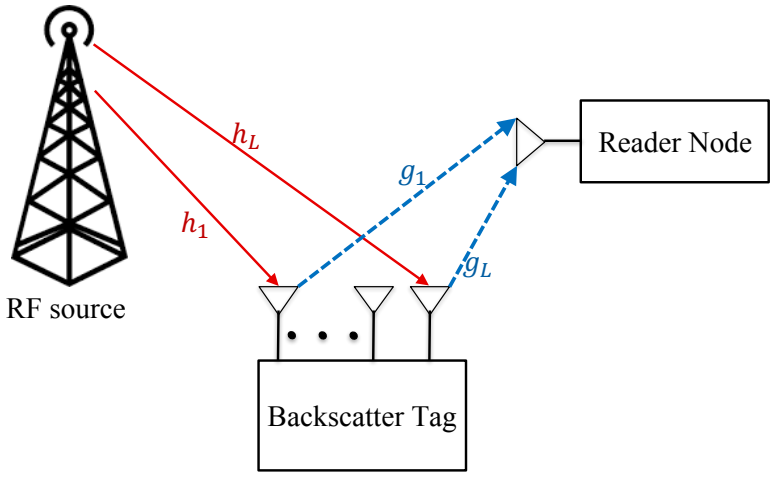

Figure 5.1: Architecture of the bistatic backscatter network, consisting of an RF source, a multiple antenna BT and a RN equipped with one antenna.

based normalization, similar to [52] and [192]. Finally, the thermal noise at the BT could be negligible, since the tag includes only passive components related to the backscattering and involves little high intensity operation [179], [193].

5.2.2 Generalized Spatial Modulation

In the case of GSM scheme, we examine one time slot, within L_u antennas are active and transmitting in the BT. The data symbol $x \in \mathbb{C}$, with $|\mathbb{C}| = M$, represents the symbol from the M-ary modulation scheme adopted in the BT, which is transmitted from all the L_u active antennas, at a time instant. Thus, the received signal at the RN is given by

$$r_{\text{GSM}} = \sqrt{P}\mathbf{F}_\ell \mathbf{x} + n, \tag{5.1}$$

where P is the average transmitted power from the RF source and n is the additive white Gaussian noise $\sim CN(0, \sigma_n^2)$, with $\sigma_n^2 = 1$, for the sake of simplicity. In addition, $\mathbf{x} \in \mathbb{C}^{L_u \times 1}$, is an $L_u \times 1$ vector with $x_i = x, \forall\, x_i \in (1, L_u)$. Finally, $\mathbf{F}_\ell$ is the DBC, regarding

is estimated on a short-term basis. Specifically, a known training signal is initially transmitted, therefore the CSI is estimated using the combined knowledge of the transmitted and the received signal at the RN, with the use of maximum likelihood or other estimation technique [191].

the schematic diagram of Fig. 5.1 and can be described using a row vector as follows

$$\mathbf{F}_{\ell} = \underbrace{\left[h_{\ell_1} g_{\ell_1} \ \cdots \ h_{\ell_4} g_{\ell_4} \ \cdots \ h_{\ell_{L_u}} g_{\ell_{L_u}}\right]}_{L_u \text{ elements}}, \tag{5.2}$$

where $\ell = (\ell_1, \ell_2, \cdots, \ell_{L_u})$ indicates the antenna combination of the L_u active and transmitting antennas out of L antennas in the BT, and ℓ_i indicates the index of the i-th antenna in the antenna combination ℓ. Furthermore, h_{ℓ_i}, represents the forwarded channel of the DBC, from the transmit antenna of the RF source to the i-th antenna in the antenna combination ℓ. In addition, g_{ℓ_i} represents the backscattered channel, from the i-th antenna of the antenna combination ℓ to the RN. One main observation is that for a specific time instant, the total channel gain at the RN is simplified to $F_{\ell} = \sum_{i=1}^{L_u} h_{\ell_i} g_{\ell_i}$, while the data symbol transmitted, to a scalar $x \in \mathbb{C}$.

The spectral efficiency (bits/s/Hz) achieved with the GSM technique is

$$m_{\text{GSM}} = m_c + \log_2 M, \tag{5.3}$$

where $m_c = \lfloor \log_2 \binom{L}{L_u} \rfloor$.

The optimal metric applied on the RN for the ML decision is given by

$$\left[\hat{x}, \hat{\ell}\right] = \arg\min_{\hat{x}, \hat{\ell}} \left\| \left[\right] \right\| r_{\text{GSM}} - \sqrt{P} \sum_{i=1}^{L_u} \hat{h}_{\ell_i} \hat{g}_{\ell_i} \hat{x} \Big|^2, \tag{5.4}$$

where $\hat{h}_{\ell_i}$, $\hat{g}_{\ell_i}$ are the estimated forwarded and backscattered channels of DBC, respectively, from the estimated set of active transmitting antennas $\hat{\ell}$; and $\hat{x}$ is the estimated data symbol from the M-ary constellation scheme adopted in the BT.

SM is studied as a simplified scheme of GSM. From the L existing antennas in the BT, only one antenna remains active during transmission. Thus, the received signal at the RN and the optimal metric applied for the ML decision are given by (5.1) and (5.4), respectively, if we set $L_u = 1$. The spectral efficiency (bits/s/Hz) of the SM scheme is

$$m_{\text{SM}} = \log_2(LM). \tag{5.5}$$

5.2.3 Generalized Spatial Modulation with Alamouti

In case of Alamouti OSTBC scheme, two antennas are active in two time slots. Furthermore, two data symbols x_1 and x_2 are transmitted in these two time slots, where $x_i \in \mathbb{C}$, with $i = 1, 2$ and $|\mathbb{C}| = M$. More specifically, these two data symbols

are drawn from the M-ary constellation adopted and transmitted in an orthogonal manner, described by the codeword

$$\mathbf{X} = (\mathbf{x}_1\ \mathbf{x}_2) = \begin{pmatrix} x_1 & x_2 \\ -x_2^* & x_1^* \end{pmatrix}, \tag{5.6}$$

where columns and rows correspond to the number of transmit antennas and the symbol interval, respectively. In our study we use Alamouti OSTBC in combination with GSM [183], while the general system model follows the previous description. The codewords described in (5.6) are extended to the antenna domain and used in order to compose the codebooks. Each codebook is consisted of codewords, that should not have overlapping columns between them.

Furthermore, a rotation angle θ is considered, in order to ensure maximum diversity and coding gain at the expense of expansion of the signal constellation [183, Eq.(10)]. In case where θ is not considered, the resulting overlapping columns of codeword pairs from different codebooks reduces the transmit diversity order to one. In case of a bistatic BackCom system, with four antennas at the BT, the following four codewords are created

$$\chi_1 = \left\{\mathbf{X}_{11}, \mathbf{X}_{12}\right\} = \left\{\begin{pmatrix} x_1 & x_2 & 0 & 0 \\ -x_2^* & x_1^* & 0 & 0 \end{pmatrix}, \begin{pmatrix} 0 & 0 & x_1 & x_2 \\ 0 & 0 & -x_2^* & x_1^* \end{pmatrix}\right\}, \tag{5.7}$$

and

$$\chi_2 = \left\{\mathbf{X}_{21}, \mathbf{X}_{22}\right\} = \left\{\begin{pmatrix} 0 & x_1 & x_2 & 0 \\ 0 & -x_2^* & x_1^* & 0 \end{pmatrix}, \begin{pmatrix} x_2 & 0 & 0 & x_1 \\ x_1^* & 0 & 0 & -x_2^* \end{pmatrix}\right\} \exp(j\theta). \tag{5.8}$$

By taking into consideration the expand in time domain and specifically in two time intervals, the received signal in the RN is a 2×1 vector, which due to the orthogonality of the Alamouti's OSTBC, may be equivalently obtained by [183, Eq.(16)]

$$\mathbf{r}_{\text{GSMA}} = \sqrt{P}\mathbf{F}_\ell \begin{bmatrix} x_1 \\ x_2 \end{bmatrix} + \mathbf{n}, \tag{5.9}$$

where $\mathbf{F}_\ell$ is a 2×2 equivalent channel matrix of the Alamouti coded GSM scheme, equal to

$$\mathbf{F}_\ell = \begin{bmatrix} h_{\ell_1} g_{\ell_1} \theta & h_{\ell_2} g_{\ell_2} \theta \\ (h_{\ell_2} g_{\ell_2} \theta)^* & -(h_{\ell_1} g_{\ell_1} \theta)^* \end{bmatrix}. \tag{5.10}$$

Similarly with GSM, h_{ℓ_1} and h_{ℓ_2}, represent the forwarded channels of the DBC to the first and second active transmitting antenna of set ℓ, in the BT. Likewise, g_{ℓ_1} and g_{ℓ_2}

represent the backscattered channels, from the first and second active transmitting antenna of the set ℓ, to the RN. Furthermore, $\mathbf{n}$ is a 2×1 vector representing the AWGN $\sim CN(0, \sigma_n^2 \mathbf{I})$.

Thus the spectral efficiency (bits/s/Hz) for the GSMA scheme is

$$m_{\text{GSMA}} = \frac{1}{2} \log_2 c + \log_2 M, \tag{5.11}$$

where c denotes the total number of codewords in GSMA and is given by

$$c = \lfloor \binom{L}{2} \rfloor_{2^p}, \tag{5.12}$$

where p is a positive integer.

During two consecutive symbols intervals, the bits transmitted from the BT are $2m_{\text{GSMA}}$, where the first $\log_2 c$ bits determine the antenna pair combination, while the last $2 \log_2 M$ bits determine the data symbol pair (x_1, x_2). Taking into consideration the spectral efficiency of Alamouti's OSTBC, which is given by $m_{\text{Alamouti}} = \log_2 M$ bits/s/Hz, we observe an increment of $\frac{1}{2} \log_2 c$ bits/s/Hz for GSMA.

Regarding the ℓ-th set of active transmitting antennas combination in the BT, the receiver in the RN uses the decomposition as followed in [194] and determines the associated minimum ML metrics $e_{1,\ell}$ and $e_{2,l}$ for x_1 and x_2, resulting from the orthogonality of $\mathbf{f}_{\ell_1}$ and $\mathbf{f}_{\ell_2}$, as

$$e_{1,\ell} = \arg\min_{x_1 \in \mathbb{C}} \left\| \mathbf{r}_{\text{GSMA}} - \sqrt{P} \mathbf{f}_{\ell_1} x_1 \right\|^2, \tag{5.13}$$

$$e_{2,\ell} = \arg\min_{x_2 \in \mathbb{C}} \left\| \mathbf{r}_{\text{GSMA}} - \sqrt{P} \mathbf{f}_{\ell_2} x_2 \right\|^2, \tag{5.14}$$

where $\mathbf{F}_\ell = [\mathbf{f}_{\ell_1}, \mathbf{f}_{\ell_2}]$. Since $e_{1,\ell}$ and $e_{2,\ell}$ are calculated by the ML decoder for the ℓ-th set of active transmitting antennas, their summation $e_\ell = e_{1,\ell} + e_{2,\ell}$ gives the total ML metric for the ℓ-th set. Finally, the receiver at the RN makes a decision by choosing the minimum antenna combination metric as $\hat{\ell} = \arg\min_{\ell} e_\ell$.

5.3 Performance Analysis

In this section, we analytically derive the pairwise error probability (PEP) for the studied techniques (GSM, SM and GSMA) applied in our bistatic backsatter system model, investigating the union bound for the probability of error, in each case. Finally, in the last part we further investigate the enhanced performance succeeded from GSMA, by analyzing the diversity order.

5.3.1 Pairwise Error Probability for GSM and SM

We further proceed by following the steps proposed in [180], in order to calculate the PEP for GSM technique. More specifically, the GSM modulated signal is backscattered from the L_u active antennas of the BT over the DBC channel. By taking into consideration the euclidean distances, the pairwise probability of error is computed

$$\Pr(x_\ell \to \hat{x}_{\hat{\ell}}) = \Pr\left(\|D(\ell, x)\|^2 > \|D(\hat{\ell}, \hat{x})\|^2\right), \tag{5.15}$$

where x_ℓ indicates the data symbol $x \in M$-ary modulation, that is transmitted from a set of antennas combination ℓ. In addition, $\hat{x}_{\hat{l}}$ indicates the estimated M-ary data symbol $\hat{x}$, which is transmitted from an estimated set of antennas combination $\hat{\ell}$. Furthermore, $\Pr(x_\ell \to \hat{x}_{\hat{\ell}})$ denotes the PEP on deciding $\hat{x}_{\hat{\ell}}$, while x_ℓ is actually transmitted. PEP highly depends on the squared Euclidean distance between the pairs of the transmitted and estimated spatial symbols, denoted as $\|D(\ell, x)\|^2$ and $\|D(\hat{\ell}, \hat{x})\|^2$, respectively. Recalling the expression in (5.1), we further proceed with

$$D(\ell, x) = r_{\text{GSM}} - \sqrt{P} F_\ell x = n. \tag{5.16}$$

Taking into consideration that $\hat{F}_\ell = \sum_{i=1}^{L_u} \hat{h}_{\ell_i} \hat{g}_{\ell_i}$, we can express $D(\hat{\ell}, \hat{x})$ as

$$D(\hat{\ell}, \hat{x}) = r_{GSM} - \sqrt{P} \hat{F}_\ell \hat{x} = n + \sqrt{P} \left(\sum_{i=1}^{L_u} h_{\ell_i} g_{\ell_i} x - \sum_{i=1}^{L_u} \hat{h}_{\ell_i} \hat{g}_{\ell_i} \hat{x} \right). \tag{5.17}$$

With the proper substitutions and calculations, we state the following Proposition.

Proposition 4. *The PEP for GSM is upper bounded by*

$$Pr(x_\ell \to \hat{x}_{\hat{\ell}} | q) \leq \int_0^\infty Q\left(\sqrt{\gamma_n}\right) f_{\gamma_n}(\gamma_n) d\gamma_n, \tag{5.18}$$

where q is a non-negative integer and denotes the number of independent terms that consist the DBC, γ_n, for each pair of estimated symbols $(x_\ell, \hat{x}_{\hat{\ell}})$. In addition $f_{\gamma_n}(\gamma_n)$ is the pdf of γ_n and is given as [54, Eq.(8)]

$$f_{\gamma_n}(\gamma_n) = \frac{2\gamma_n^{(q-1)/2}}{(q-1)! \hat{\gamma}^{(q+1)/2}} K_{q-1}\left(2\sqrt{\frac{\gamma_n}{\hat{\gamma}}}\right), \tag{5.19}$$

where $K_{q-1}(\cdot)$ denotes the modified Bessel function of the second kind and $\hat{\gamma} = P/2$ is the average power at the RN.

Proof. See Appendix B.6. □

Note that the q is numerically evaluated. The set of values is $\{0, 1, 2, \ldots, N_3\}$, where $N_3 = L_u x_R + L_u x_I + L_u \hat{x}_R + L_u \hat{x}_I$, with $x_R \approx \Re\{x\}$, $x_I \approx \Im\{x\}$, $\hat{x}_R \approx \Re\{\hat{x}\}$ and $\hat{x}_I \approx \Im\{\hat{x}\}$. One main observation regarding the possible values of q is that when the decoding is successful, i.e $\hat{x}_{\hat{\ell}} = x_\ell$, then $q = 0$, while when neither the antennas nor the data symbol are correctly estimated, then $q = N_3$.

We herein calculate the probability of error in terms of SER for GSM, by defining an upper bound for the union of the events. The events taken into consideration and summed up for the calculation of the union bound, are all the PEP for all the possible combinations, in terms of the estimated active transmitting antennas and the estimated data symbol from the M-ary modulation scheme. Thus, the union bound for the probability of error in terms of SER, regarding the GSM scheme, is given by

$$\mathrm{P}_s^{\mathrm{GSM}} \leq \sum_{i=2}^{N_1} \Pr(x_1 \to \hat{x}_i | q), \tag{5.20}$$

where $N_1 = M\binom{L}{L_u} - 1$ and $\Pr(x_i \to \hat{x}_i | q)$ is given by (5.18). The PEP and SER for the simplified case of SM technique, follow the same analysis as in GSM, by considering only one transmitting antenna, i.e. $L_u = 1$.

5.3.2 Pairwise Error Probability for GSMA

In the following, before proceeding to the calculation of PEP, we summarize the steps needed to be followed in order to design the GSMA, considering the proper codewords, codebooks and rotation angles.

- Given the total number of transmit antennas in the BT, L, we calculate the number of possible antenna combinations for the transmission of Alamouti's OSTBC. The number of possible antenna combinations is $\binom{L}{L_u}$. However, the number of antenna combinations that can be considered for transmission must be a power of two. Therefore, only $L_c = 2^{m_c}$ combinations, can be used, where $m_c = \lfloor \log_2 \binom{L}{L_u} \rfloor$.

- We proceed by calculating the total number of codewords c, given by (5.12).

- We calculate the number of codewords in each codebook $\chi_i, i = 1, 2, \cdots, v-1$ from $\alpha = \lfloor L/2 \rfloor$ and the total number of codebooks from $v = \lceil c/\alpha \rceil$. Note, that the last codebook χ_v does not need to have α codewords, i.e. its cardinality is $\alpha' = c - \alpha(v-1)$.

- We construct the codebooks, considering the following two facts, i.e.:
  (a) each codebook must contain non-interfering codewords chosen form the pairwise combinations of L transmitting antennas in the BT,
  (b) each codebook must be composed of codewords with antenna combinations that were never used in the construction of a previous codebook.
- We use the appropriate rotation angle θ_i, for each codebook χ_i, based on the signal constellation and the antenna configuration, as optimally calculated per case in [183, Eq.(10)]. More specifically

$$\theta_i = \begin{cases} \frac{(i-1)\pi}{v}, & \text{for BPSK} \\ \frac{(i-1)\pi}{2v}, & \text{for QPSK.} \end{cases} \tag{5.21}$$

The performance analysis of the proposed GSMA scheme, is now focused on calculating $\Pr(\mathbf{X} \to \hat{\mathbf{X}})$, which is the PEP of deciding matrix $\hat{\mathbf{X}}$ when $\mathbf{X}$ is transmitted. Following the proper analysis, the next Proposition is formed.

Proposition 5. *The PEP of GSMA is upper bounded by*

$$Pr(\boldsymbol{X} \to \hat{\boldsymbol{X}}|q) \leq \int_0^\infty \int_0^\infty Q\left(\sqrt{\gamma_1 + \gamma_2}\right) f_{\gamma_1}(\gamma_1)\, d\gamma_1 \times f_{\gamma_2}(\gamma_2)\, d\gamma_2, \tag{5.22}$$

where f_{γ_i} denotes the pdf of the transmitted DBC at time instant $i \in (1, 2)$ and is given by (5.19).

Proof. See Appendix B.7. □

Having identified the PEP for GSMA from (5.22) and taking into consideration the pdf from (5.19), we may proceed to calculate the union bound for the probability of error, in terms of SER. It has to be noticed that due to the symmetry of the codebooks, all the transmission matrices have the uniform error property, i.e. have the same PEP as that of $\mathbf{X}_{11}$ [183, Eq.(24)]. Thus, we obtain the upper bound as follows

$$\mathrm{P}_s^{\mathrm{GSMA}} \leq \sum_{j=2}^{\alpha} \Pr(\mathbf{X}_{11} \to \mathbf{X}_{1j}|q) + \sum_{i=2}^{v-1} \sum_{j=1}^{\alpha} \Pr(\mathbf{X}_{11} \to \mathbf{X}_{ij}|q) + \sum_{j=1}^{\alpha'} \Pr(\mathbf{X}_{11} \to \mathbf{X}_{vj}|q), \tag{5.23}$$

where we recall here that v is the total number of codebooks, α is the total number of codewords in the $v-1$ codebooks, α' is the number of codewords in the last codebook v and $\Pr(\mathbf{X}_{11} \to \mathbf{X}_{ij})$ is given by (5.22).

5.3.3 Diversity Analysis

In this section we investigate the diversity order of our system model for the spatial modulation-based communication techniques studied. The diversity order d of the system is the asymptotic rate at which the probability of error P_s decays, as a function of average transmitted power P and is defined as

$$d_{\mu} = \lim_{P \to \infty} -\frac{\log \mathrm{P}_s^{\mu}}{\log P}, \tag{5.24}$$

where $\mu \in \{\text{GSM and GSMA}\}$. Taking into consideration the expression for the SER given by (5.20) and by (5.23), regarding the GSM and GSMA technique, respectively, the next Proposition is formed.

Proposition 6. *The diversity order regarding the GSM and SM technique is equal to one, i.e.* $d_{\mathrm{GSM}} = 1$, *while for GSMA technique is equal to two, i.e.* $d_{\mathrm{GSMA}} = 2$.

Proof. See Appendix B.8. □

A key conclusion from the above is that by applying a combination of the Alamouti scheme and the spatial techniques in a multiple antenna BT, there is an enhanced and improved probability of error for the detection of transmitted symbols and transmitting antennas in the RN. More specifically, we can conclude that increasing the number of transmit/receive antennas in the BT, while applying the spatial techniques of GSM and SM, one can succeed array gain. Further expanding, with the use of GSMA, we exploit also the time domain and manage to succeed transmit diversity $d_{\mathrm{GSMA}} = 2$.

5.4 Numerical Results

In this section, we provide numerical results in order to verify the enhanced performance achieved by our proposed spatial modulation-based techniques, GSM, SM and GSMA, when applied to the considered system model. We evaluate their performance in terms of SER, targeting the same spectral efficiency and we further study and present their behavior in terms of spectral efficiency, while varying the number of antennas in the BT. More specifically, Monte-Carlo simulations are carried out and all the outcomes presented are calculated with the use of 10^5 iterations.

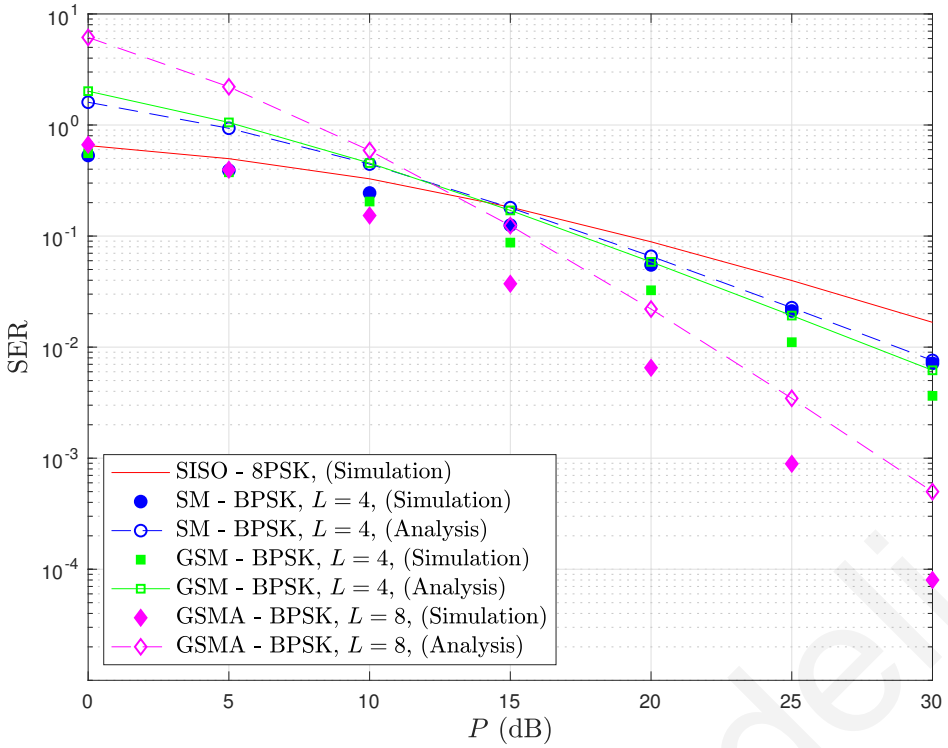

Figure 5.2: Comparison of GSM, SM and GSMA with a spectral efficiency 3 bits/s/Hz.

In Fig. 5.2 and Fig. 5.3, all the three schemes studied, are presented comparatively in terms of SER. With the continuous line, we present the performance of a single input single output (SISO) bistatic backscatter system with only one antenna in the BT, i.e. $L = 1$, as a metric of comparison to our proposed spatial modulation-based techniques. As expected, such a solution constitutes an upper bound for GSMA, GSM and SM. On the other hand, GSMA with the use of combined spatial and time modulation, manages to overcome the other two techniques, in terms of SER. In addition, GSM and SM, although they improve the performance of the studied backscatter system, they manage to achieve similar results in terms of SER.

The targeted spectral efficiency, regarding the evaluated simulation results presented in Fig. 5.2 and Fig. 5.3, is 3 bits/s/Hz and 4 bits/s/Hz, respectively. In order to succeed this, we combined $L = 4, 5, 8$ transmitting antennas with several modulation schemes in the BT, i.e. 16phase-shift keying (PSK), 8PSK, binary PSK (BPSK) and quadrature PSK (QPSK). Another observation from Fig. 5.2 and Fig. 5.3, is that the derived union bounds, consist tight upper bounds compared to the simulations of all the three spatial modulation-based techniques. More specifically, the union bound that is adopted in our paper, is quite sharp and is traditionally used in the literature as an appropriate upper bound for the pairwise error probabilities [145]. It

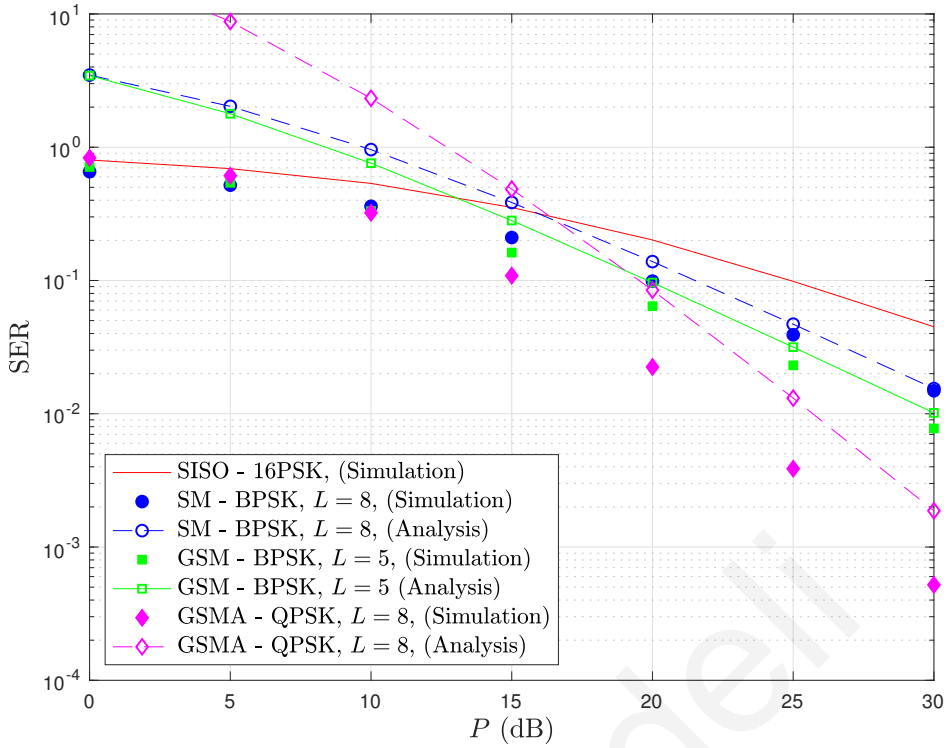

Figure 5.3: Comparison of GSM, SM and GSMA with a spectral efficiency 4 bits/s/Hz.

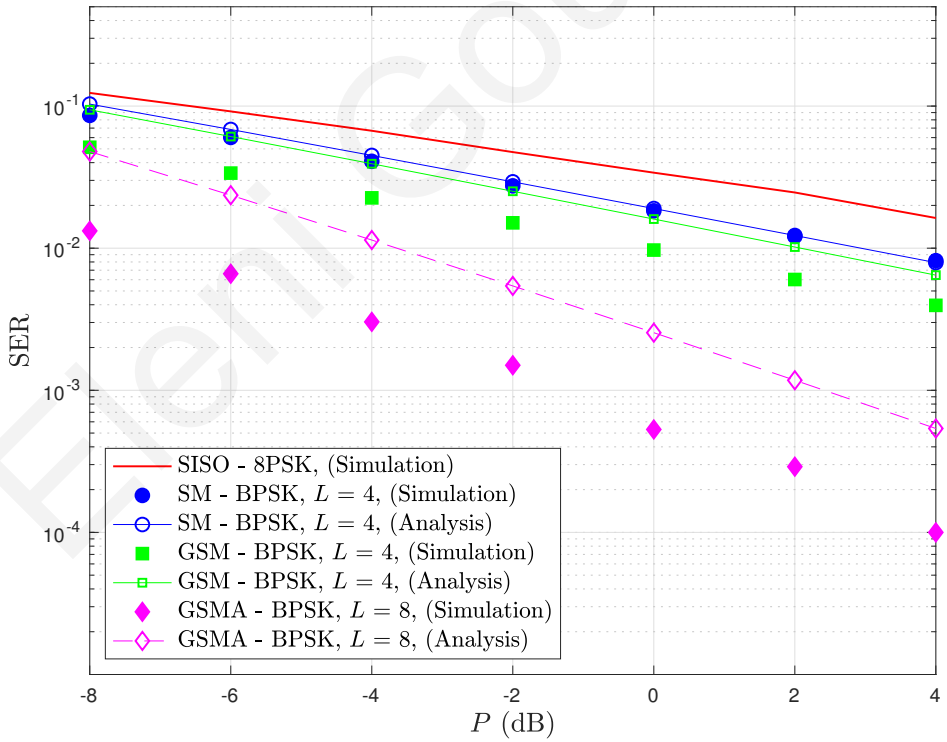

Figure 5.4: Comparison of GSM, SM and GSMA with a spectral efficiency 3 bits/s/Hz and practical numerical setup.

is noteworthy that when increasing the number of antennas in the BT, there are more combinations to estimate at the RN, consequently more pairwise error probability terms appear and the gap between the upper bound and the simulation increases.

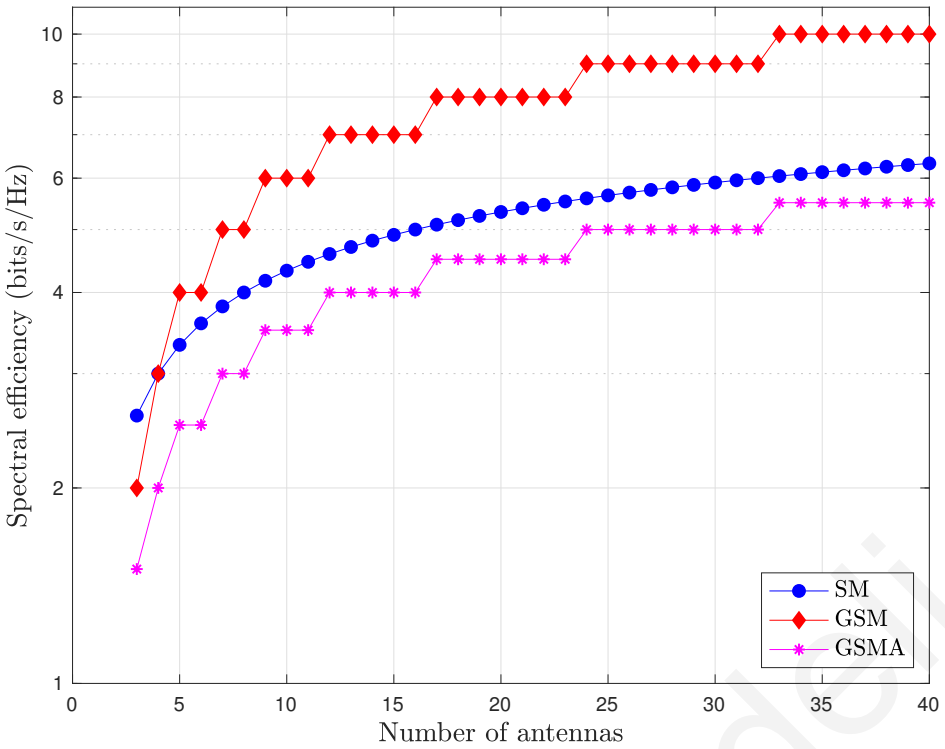

Figure 5.5: Spectral efficiency comparison for GSM, SM and GSMA.

Same behavior is noticed, when we extend our study in two time slots with the use of GSMA technique. On the other hand, when we increase the transmit power we notice that this gap smooths, which is an expected trade off. Finally, with the increase of the targeted spectral efficiency, the performance in terms of SER for all the spatial schemes studied, is slightly deteriorated.

In Fig. 5.4 we apply the mathematical framework for a practical setting, based on an indoor application [105]. More specifically, the RF source communicates with BT with a bandwidth of 2 MHz. The path loss effect is taken into consideration, while the distances between the RF source, the BT and the RN are 5 m and 6 m, respectively. It has to be noticed, that the behavior of our system model follows the same trends, as in Fig. 5.2 and Fig. 5.3. More specifically, GSMA technique prevails over GSM and SM, succeeding transmit diversity and enhanced performance in terms of SER.

In Fig. 5.5, we present how the spectral efficiency of the considered schemes is affected, when varying the number of antennas in the BT. More specifically, the modulation scheme studied is kept common in all three cases, as BPSK. In addition, for the GSM and GSMA technique, the number of transmitting antennas each time instant is $L_u = 2$, out of totally L antennas in the BT. Recalling the spectral efficiencies of each technique, as described in Section 5.2 from (5.3), (5.5), and (5.11), some main

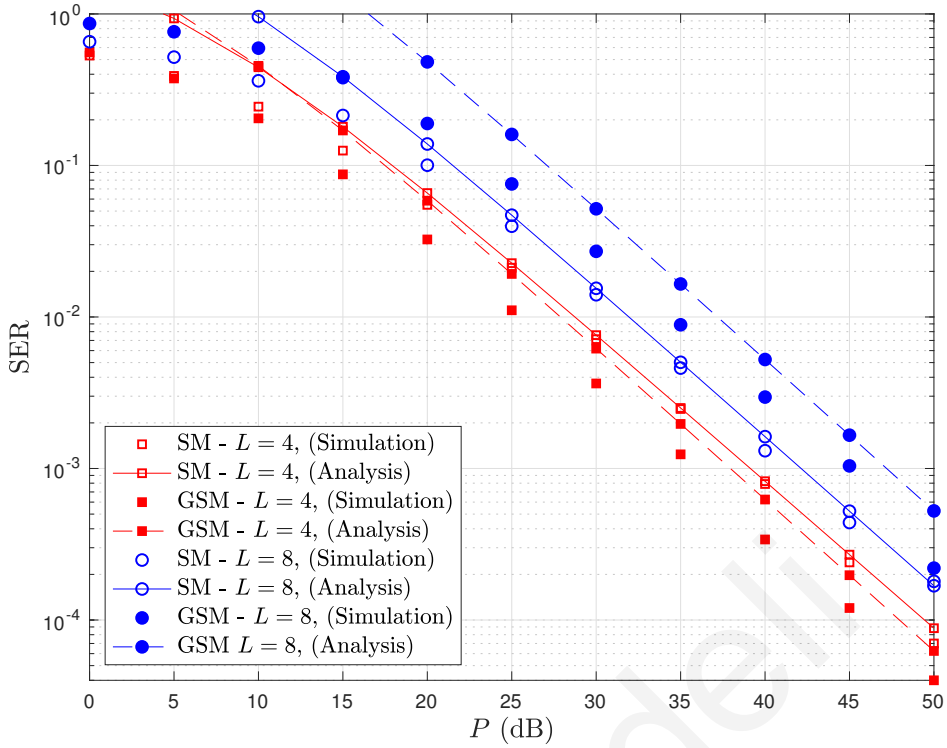

Figure 5.6: Comparison of GSM and SM, for the same number $L = 4, 8$ of antennas.

observations are derived, that are also confirmed from the relative figure. Firstly, we clearly identify that for $L > 4$, the first term of GSM spectral efficiency is always greater than the other two schemes. As such, in order to transmit the same number of bits, there is needed a sufficient larger amount of antennas in the BT regarding SM and GSMA techniques. For example, in order to transmit 4 bits/s/Hz, the antennas needed in the BT are $L = 5$ or 6 for GSM, $L = 8$ for SM and $L = 12, \ldots, 16$ for GSMA. In addition, due to the floor operation in (5.3) and (5.11), the spectral efficiency for GSM and GSMA respectively, remains the same for a range of transmitting antennas.

Figs. 5.6 and 5.7, illustrate the performance of the two backscatter spatial MIMO techniques, specifically referring to GSM and SM. BPSK modulation is applied and the number of antennas at the BT is $L = 4, 8, 16, 32$. Regarding the GSM technique, we assume two active transmitting antennas i.e. $L_u = 2$. As expected, for the same number of antennas the SM scheme provides us with an enhanced performance in terms of SER. This is justified from the fact that the spectral efficiency for GSM is higher, resulting in a higher number of transmitted bits/s/Hz, thus increasing the probability of error when decoding. Furthermore, the comparatively enhanced performance of SM to GSM, is also justified due to the highest probability of error when detecting two active and transmitting antennas instead of only one.

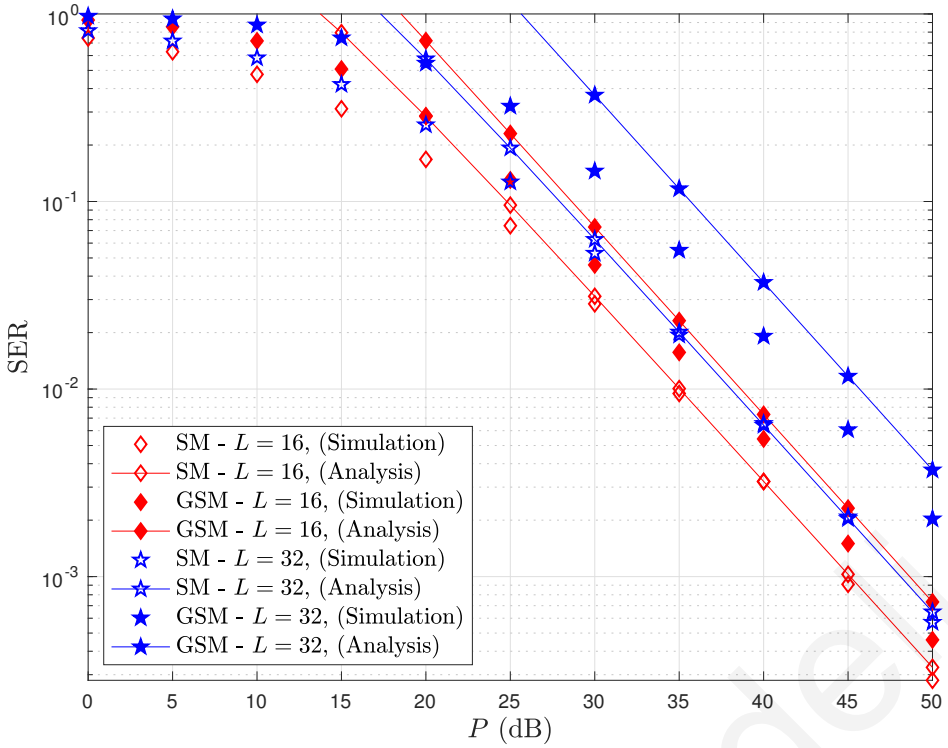

Figure 5.7: Comparison of GSM and SM, for the same number $L = 16, 32$ of antennas.

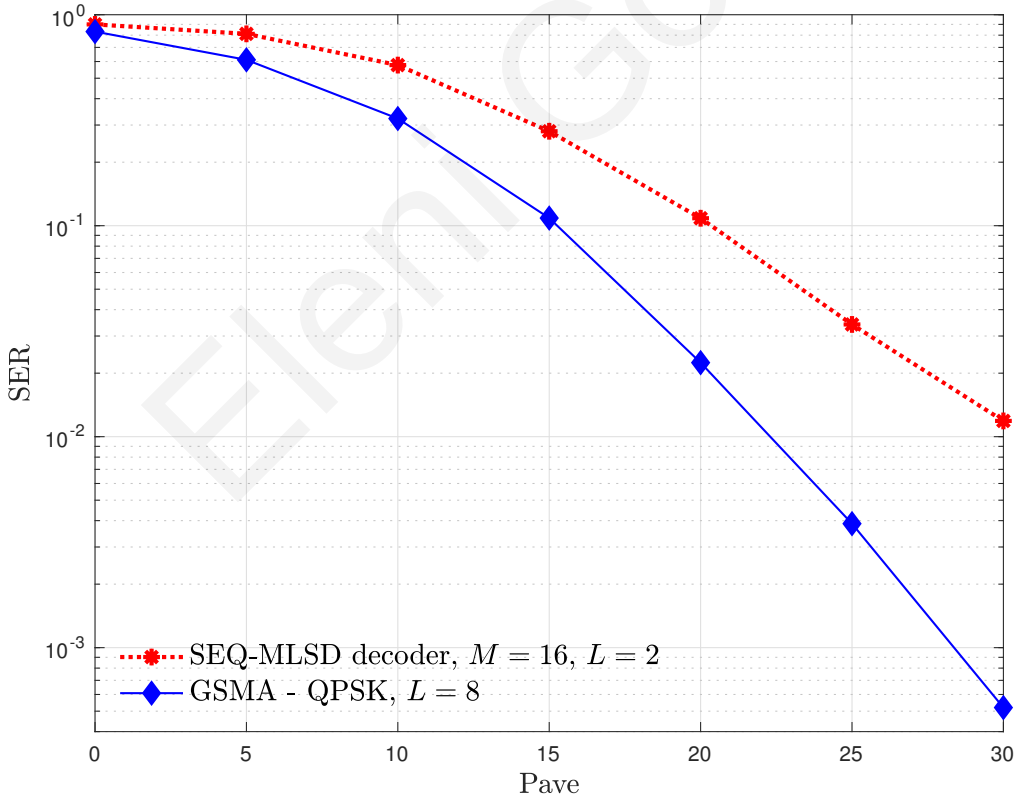

Figure 5.8: Comparison of GSMA and SEQ-MLSD decoder.

For the sake of comparison, in Fig. 5.8 we illustrate the performance, in terms of ID, of our proposed GSMA scheme with the use of Alamouti, to the sequential decoder presented in Chapter 3. Specifically, for GSMA we considered QPSK modulation with $L = 8$ antennas at the BT, resulting to a spectral efficiency of 4bits/s/Hz. On the other hand, in order to succeed the same spectral efficiency for the solution of the sequential decoder, we considered an energy modulation scheme of $M = 16$ pulses, and an observation window of $L = 2$, matching the two time slots considered in the GSMA solution. One can easily notice that GSMA technique, outperforms the solution of SEQ-MLSD decoder, while transmit diversity is achieved.

5.5 Conclusion

In this chapter, we propose the use of BackCom as a novel and high efficient solution for 5G IoT technology. The need of an IoT network is growing rapidly, targeting an interconnection of numerous small size, low cost and wireless self-powered devices. Backscatter communication seems to ideally serve the demands of such a network, since BTs are capable of transmitting their data, while at the same time may operate exclusively their own integrated circuit or partially support it, in terms of energy required, due to their harvesting capabilities. The ability of multiple antennas at the BT, gives us the opportunity to apply sophisticated spatial modulation-based techniques and achieve enhanced performance in terms of SER and spectral efficiency. Initially, we study the GSM technique, where we exploit the antenna index as an extra dimension for additional source of information. SM is also presented in our study as a special and simplified case of GSM, with only one transmitting antenna at a time instant. We further enhance our study in time domain, by proposing GSMA technique; with the use of Alamouti scheme in two transmitting antennas, we manage to improve significantly SER performance and succeed transmit diversity. Simulation and theoretical results are consistent, corroborating our proposal as an enhanced solution, in terms of overall efficiency. An interesting direction for future work is to re-evaluate the performance of our system model with non coherent detection schemes, as well as to extend our study into the millimeter wave frequency band.

Chapter 6

SWIPT with Diplexer-based Multiple-Antenna Rectification

In this chapter we adopt a recently proposed scheme at the receiver side, which achieves SWIPT without split of the resources, with the use of a diplexer. Specifically, we extend it to a diplexer-based SWIPT receiver, with multiple-antenna rectification circuits and prove enhanced performance both in terms of ID and EH. We compare our proposed design to the conventional integrated SWIPT receiver with multiple rectennas, as a benchmark to the state-of-the-art solution.

6.1 Introduction

Despite the continuous advances in SWIPT technology, there are some key challenges for practical implementations. In the literature of RF circuits, it is impossible to perform SWIPT from the same received signal by using one antenna [17]. As such, SWIPT is achieved through a separated receiver in time, power or spatial domain, where the received RF signal is split for ID and EH [18]. Furthermore, authors in [20], propose and study an integrated SWIPT receiver, where the RF to baseband conversion is replaced from a passive rectifier operation, which results in a DC power signal. Afterwards, the DC signal is also split in the power domain, for ID and EH.

The work in [19], proposes a new scheme which achieves SWIPT without split of the resources. Authors show that the same RF received signal can be used for both ID and EH, with the use of an RF diplexer at the receiver's side. Diplexers are passive devices that implement frequency-domain multiplexing. In particular, their

ports are frequency-selective, while reversing their input and output, can be used for separating higher from lower frequency signals, at one receive antenna. As such, with the proposed circuit, there is no need for a power splitter, since the low-pass band-pass diplexer allows the dual and continuous use of the same signal for SWIPT.

One of the main issues in SWIPT is the efficient ID, along with the energy that is being harvested. In the state-of-the-art, multiple antenna system models are traditionally considered as a common solution for enhanced performance either in terms of ID or EH. Specifically, in [50], authors investigate SWIPT with a multi-antenna transmitter sending data and energy to single antenna receivers adopting a time switching circuit. Beamforming for energy transfer and information transmission is considered in [51], achieving the optimal energy efficiency. Finally, regarding the ID, coherent techniques are a challenging task, since the source needs to periodically send training symbols, which results in increased signaling overhead and processing burden [30]. On the contrary, the receiver's complexity is reduced with non-coherent techniques.

Motivated by the above, in this chapter we propose a topology with the use of an RF circuit implementation with multiple diplexers. As such we achieve SWIPT with enhanced performance, both in terms of ID and EH. We further succeed non-coherent decoding, with the use of a ML-based soft decoder. In particular, we examine the performance of the proposed solution, by adopting two different modulation schemes, i.e. binary OOK and PEM, appropriate for energy detection. We further compare the performance of the proposed system model to the conventional integrated receiver, with multiple rectennas. Simulation results fully validate the theoretical analysis and confirm the benefits of the proposed diplexer-based receiver. Finally, we show that PEM enhances the EH, though deteriorates the ID, compared to OOK.

6.2 System Model

As seen in Fig. 6.1, we consider a single input multiple output SWIPT system. The source transmits from a single antenna, a baseband signal $x(t)$ with $\mathbb{E}[x^2(t)] = 1$. At the receiver's side we consider K antennas, each one connected to a diode, followed by a diplexer. The modulation scheme adopted is OOK, while symbols $x \in [0, 1]$, are transmitted with equal probability.

Then, the up-converted RF signal is transmitted over a Rayleigh fading channel,

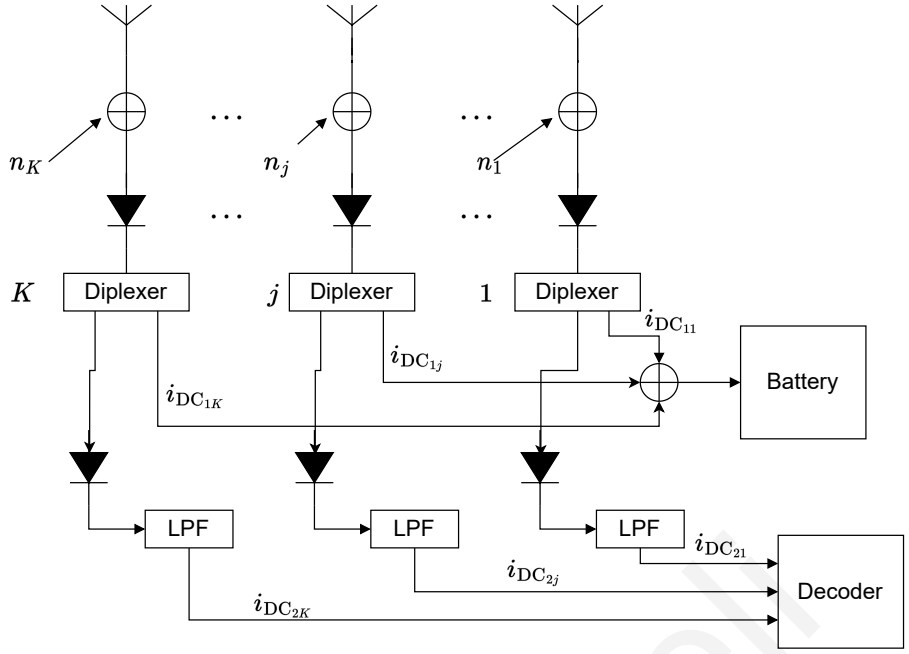

Figure 6.1: Architecture of the diplexer-based SWIPT receiver.

with average transmit power P and we assume that f is the carrier frequency. The signal propagates through a wireless channel gain $h_j > 0$, where $j \in [1, \cdots, K]$ and phase shift $\theta \in [0, 2\pi)$. As such, the transmitted RF band signal is given by $\sqrt{2P}\mathbb{R}\left\{x(t)e^{j2\pi ft}\right\}$. The noise from a receiving antenna j, is modeled as an AWGN i.e. $\sqrt{2}\mathbb{R}\{n_j(t)e^{j2\pi ft}\}$.

Therefore, the received RF signal at an antenna j is

$$y_j(t) = \sqrt{2}\mathbb{R}\left\{h_j\sqrt{P}x(t)e^{j(2\pi ft+\theta)} + n_j(t)e^{j2\pi ft}\right\} = \sqrt{2}\mu_{y_j}(t)\cos\left(2\pi ft + \phi_{y_j}(t)\right), \tag{6.1}$$

where

$$\phi_{y_j}(t) = \arctan\frac{\mu_{I_j}(t)}{\mu_{R_j}(t)}, \tag{6.2}$$

$$\mu_{y_j}(t) = \sqrt{\mu_{R_j}(t)^2 + \mu_{I_j}(t)^2}, \tag{6.3}$$

$$\mu_{R_j}(t) = h_j\sqrt{P}x(t)\cos\left(\phi(t) + \theta\right) + n_{R_j}(t), \tag{6.4}$$

$$\mu_{I_j}(t) = h_j\sqrt{P}x(t)\sin\left(\phi(t) + \theta\right) + n_{I_j}(t), \tag{6.5}$$

where n_{R_j} and n_{I_j} denote the real and imaginary part of complex AWGN at each receive antenna j, respectively.

At each antenna j, the received RF signal $y_j(t)$ is converted to DC signal $i_j(t)$, with the use of a single Schottky diode. With an input voltage proportional to $y_j(t)$, the current harmonics through the first diode can be calculated as

$$i_j(t) = I_s(e^{\gamma y_j(t)} - 1) = \sum_{n=1}^{\infty}\frac{I_s}{n!}\left(\gamma y_j(t)\right)^n = \alpha_1 y_j(t) + \alpha_2 y_j^2(t) + \alpha_3 y_j^3(t) + \cdots, \tag{6.6}$$

where I_s is the saturation current, γ denotes the reciprocal of the thermal voltage of the Schottky diode, and the coefficients α_n's are given by $\alpha_n = I_s\gamma^n/n!$, with $n = 1, 2, \cdots$, due to the expansion of the exponential function. By ignoring the higher-order (larger than two) terms of $y_j(t)$, we obtain the output current from the first diode, as follows

$$\begin{aligned} i_j(t) &\approx \sqrt{2}\alpha_1\mu_{y_j}(t)\cos\left(2\pi ft + \phi_{y_j}(t)\right) + 2\alpha_2\mu_{y_j}^2(t)\cos^2\left(2\pi ft + \phi_{y_j}(t)\right) \\ &= \alpha_2\mu_{y_j}^2(t) + \sqrt{2}\alpha_1\mu_{y_j}(t)\cos\left(2\pi ft + \phi_{y_j}(t)\right) + \alpha_2\mu_{y_j}^2(t)\cos\left(4\pi ft + 2\phi_{y_j}(t)\right). \end{aligned} \quad (6.7)$$

The output current $i_j(t)$ at each receive antenna j, is then channeled as input to a diplexer, which is processed by a LPF and a pass-band filter. As such, the diplexer successfully separates the low frequency components from the higher ones, as those described in (6.7).

Specifically, the LPF in the diplexer, removes the high-frequency harmonics at both f and $2f$ and a DC signal

$$i_{\mathrm{DC}_{1_j}}(t) = \alpha_2\mu_{y_j}^2(t), \quad (6.8)$$

appears as one of the outputs of the diplexer. The DC outputs from all the K diplexers are added with the use of a DC combiner and then channeled to charge the battery and store the energy. Since a_2 is a constant specified by the diode, for convenience we assume in the sequel that $a_2 \approx 1$. Furthermore, substituting (6.4) and (6.5) into (6.3) yields

$$\mu_{y_j}^2 = \left(h_j\sqrt{P}x(t)\cos\left(\phi(t)+\theta\right) + n_{R_j}(t)\right)^2 + \left(h_j\sqrt{P}x(t)\sin\left(\phi(t)+\theta\right) + n_{I_j}(t)\right)^2. \quad (6.9)$$

For convenience we re-express (6.9) as follows

$$\mu_{y_j}^2(t) = |h_j\sqrt{P}xe^{j(\phi(t)+\theta)} + n_j(t)|^2. \quad (6.10)$$

Since planar rotation does not change the statistics of $n_j(t)$, (6.10) can be equivalently written as

$$\mu_{y_j}^2 = |h_j\sqrt{P}x + n_j|^2. \quad (6.11)$$

Following our analysis, the suppressed signals from the LPF of the diplexer are used as the second output of the diplexer from the pass-band filter. Without loss of generality, we keep only the main harmonic at f and remove the higher harmonics at $2f$, i.e. $\sqrt{2}\alpha_1\mu_{y_j}(t)\cos\left(2\pi ft + \phi_{y_j}(t)\right)$. This signal is also used as input to the second diode.

Subsequently, the output current of the second diode is now processed by a LPF, through which all high-frequency harmonic components are removed. As such the DC signal from a received antenna j, that appears as the output of the second diode and input of the ADC, is

$$i_{\mathrm{DC}_{2j}} = \alpha_1^2 \alpha_2 \mu_{y_j}^2, \tag{6.12}$$

where we assume that $\alpha_1^2 \alpha_2 \approx 1$. Herein, we note that both the harmonics of f and $2f$ have been removed, while as in the first diode the noise from the rectifier is considered negligible.

Considering that CSI is not available at the receiver, non-coherent detection is adopted, while soft decoding is succeeded with the use of ML. As seen in Fig. 6.1, the decoder of the proposed diplexer-based SWIPT receiver, samples and decodes, the DC outputs, i.e. $i_{\mathrm{DC}_{2j}}$, from K diodes. The optimum decision rule, is based on the observation vector $\boldsymbol{i}_{\mathrm{DC}_2} = [i_{\mathrm{DC}_{21}}, \cdots, i_{\mathrm{DC}_{2K}}]$. The symbol that yields the maximum conditioned density $f(\boldsymbol{i}_{\mathrm{DC}_2}|x)$ is selected

$$\tilde{x} = \underset{x \in (0,1)}{\operatorname{argmax}} f(\boldsymbol{i}_{\mathrm{DC}_2}|x). \tag{6.13}$$

Assuming that the noise is independent between different receive antennas, the distribution can be factored as

$$f(\boldsymbol{i}_{\mathrm{DC}_2}|x) = \prod_{j=1}^{j=K} f(i_{\mathrm{DC}_{2j}}|x), \tag{6.14}$$

where $f(i_{\mathrm{DC}_{2j}}|x)$ denotes the conditional pdf of $i_{\mathrm{DC}_{2j}}$, considering that x is transmitted. From (6.11) and (6.12), we notice that $i_{\mathrm{DC}_{2j}}$ is exponentially distributed with pdf

$$f(i_{\mathrm{DC}_{2j}}) = \lambda_x e^{-\lambda_x i_{\mathrm{DC}_{2j}}}, \tag{6.15}$$

where λ_x denotes the rate parameter and is calculated from

$$\lambda_x = 1/\mathbb{E}(i_{\mathrm{DC}_{2j}}) = 1/(Px^2 + 1), \tag{6.16}$$

as such we herein define $\lambda_0 = 1$ and $\lambda_1 = 1/(P+1)$.

Therefore, the final decision on the transmitted symbol is based on the following criterion

$$\prod_{j=1}^{j=K} f(i_{\mathrm{DC}_{2j}}|0) \underset{\tilde{x}=1}{\overset{\tilde{x}=0}{\gtrless}} \prod_{j=1}^{j=K} f(i_{\mathrm{DC}_{2j}}|1). \tag{6.17}$$

6.3 Performance Analysis

In this section, we study the performance of the proposed diplexer-based SWIPT receiver, for the ID and EH.

6.3.1 Symbol Error Rate

As seen in Fig. 6.1 the received RF power at each receive antenna $j \in [1, K]$, results in a DC power signal, $i_{\mathrm{DC}_{2j}}$ which is used for ID. The decoder decides on the transmitted symbol $\tilde{x}$, with the use of ML and (6.17). As such, we herein calculate the total probability of error, from the following Lemma.

Lemma 1. *The total probability of error for the SWIPT receiver with multiple diplexers is*

$$P_{\mathrm{D}} = \frac{1}{2\Gamma(K)}\Big(\gamma(K, \lambda_1 t) + \Gamma(K, t)\Big), \tag{6.18}$$

where

$$t = \frac{K}{(\lambda_1 - \lambda_0)} \ln\left(\frac{\lambda_1}{\lambda_0}\right). \tag{6.19}$$

Proof. See Appendix B.9. □

6.3.2 Average Energy Harvested

For the computation of the average energy that is being harvested we consider a conversion efficiency of $\zeta = 0.7$ [195]. As seen in Fig. 6.1, the output from the LPF of each diplexer, provides at each receive antenna j, a DC output, i.e. $i_{\mathrm{DC}_{1j}}$, given from (6.8) and (6.11). All these outputs from the K antennas are summed with the use of a DC combiner and channeled to the battery for EH. As such the average EH is given by

$$Q_{\mathrm{D}} = \zeta \sum_{j=1}^{j=K} \sum_{x \in (0,1)} \mathbb{P}(x)\mathbb{E}[i_{\mathrm{DC}_{1j}}] = \frac{\zeta}{2} \sum_{j=1}^{j=K} \sum_{x \in (0,1)} \int_0^{\infty} i_{\mathrm{DC}_{1j}} f(i_{\mathrm{DC}_{1j}}) d i_{\mathrm{DC}_{1j}} = \frac{1}{2} K \zeta \alpha_2 P. \tag{6.20}$$

We herein note that $i_{\mathrm{DC}_{1j}}$ follows the exponential distribution as $i_{\mathrm{DC}_{2j}}$ and the pdf is given from (6.15). This is due to the assumption that $\alpha_1^2 \alpha_2 \approx 1$. As such from (6.8) and (6.12) $i_{\mathrm{DC}_{1j}} = i_{\mathrm{DC}_{2j}} = \mu_{y_j}^2$. Furthermore, we assume that the noise introduced by each rectifier, i.e. n_j, is a small constant and thus ignored for the EH.

Conventional Integrated SWIPT Receiver [20]

Herein, we compare the proposed system model with the solution of an integrated SWIPT receiver with multiple rectennas, in terms of SER and EH [195]. The received power signal at each receive antenna of the integrated receiver, activates the rectifier and provides a DC power signal as output of the LPF. This signal is the same as the DC output, $i_{\mathrm{DC}_{1j}}$, in our proposed system model. Thereafter, a splitter is used and a portion ρ of the DC power signal is used for ID and $1-\rho$ for EH, with $\rho \in (0,1)$. Similarly, the decoder decides on the transmitted symbol $\tilde{x}$, with the use of ML and soft decoding.

The total probability of error, is derived by using the following Proposition.

Proposition 7. *The probability of error, in terms of SER, for the conventional integrated SWIPT receiver ,with multiple rectennas at the receiver's side, is given by*

$$P_{\mathrm{I}} = \frac{1}{2\Gamma(K)}\Big(\gamma(K, \lambda_1 \rho t) + \Gamma(K, \rho t)\Big). \tag{6.21}$$

Proof. See Appendix B.10. □

The average EH is derived considering that $(1-\rho)$ of the DC output form each receive antenna j, is used for EH. As such, following the same steps as in the proposed system model of the diplexer-based SWIPT receiver, the average EH is

$$Q_{\mathrm{I}} = (1-\rho)Q_{\mathrm{D}} = \frac{1}{2}(1-\rho)K\zeta\alpha_2 P. \tag{6.22}$$

6.3.3 Pulse Energy Modulation

For the sake of comparison, we additionally study a different modulation scheme. It has to be noticed, that the analysis is general for energy detection, while what changes with the different adopted modulation schemes, is the rate parameters. More specifically, the modulation scheme used by the transmitter for comparison, is PEM, with M energy levels. We design our energy pulse based symbol alphabet, based on equi-spaced amplitudes as in [39]. Specifically, we assume that a set of M symbols $x_i \in \{1d, 2d, \ldots, Md\}$, are mapped to each energy level, where d is the distance between the energy pulse based symbols. Therefore, we have

$$\mathbb{E}[x^2(t)] = \frac{1}{M}\sum_{i=1}^{M} x_i^2 = \frac{d^2}{6}(M+1)(2M+1) = 1, \tag{6.23}$$

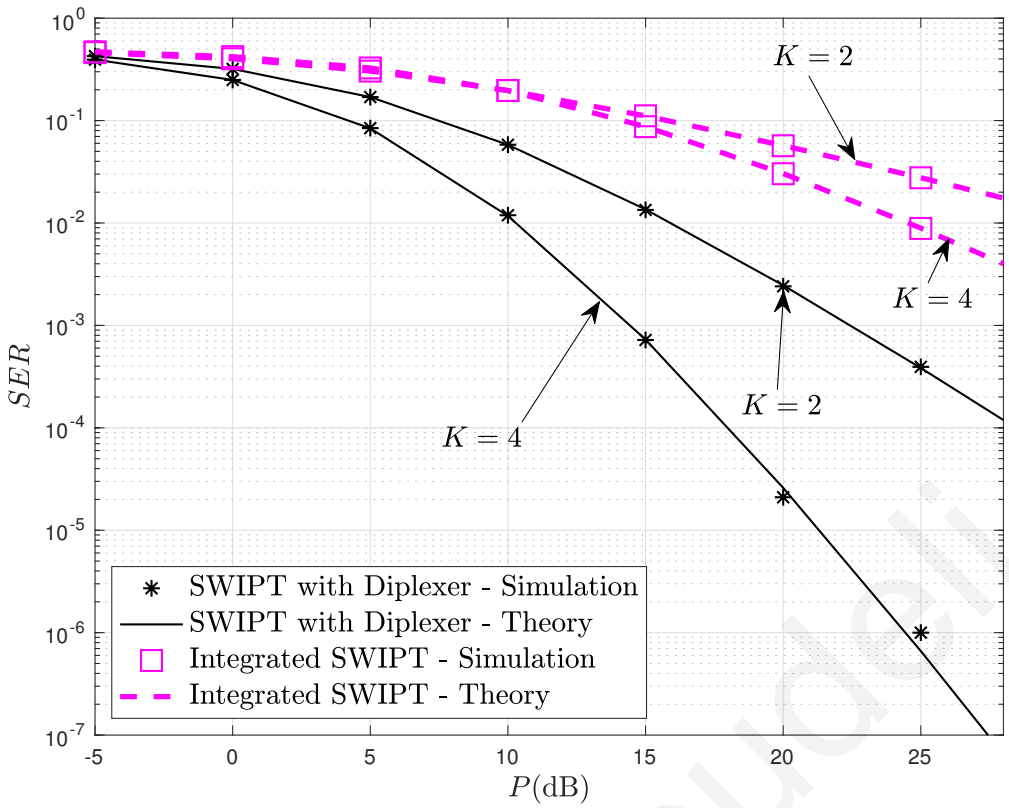

Figure 6.2: SER of the proposed diplexer-based SWIPT receiver compared to conventional integrated SWIPT receiver; for $K = 2, 4$ and $\rho = 0.4$.

which results in

$$d = \sqrt{\frac{6}{(M+1)(2M+1)}}. \tag{6.24}$$

Herein, we need to consider that with PEM, the rate parameters given from (6.16) are now defined as $\lambda_{x_i} = 1/(Px_i^2 + 1) = 1/\left(P(id)^2 + 1\right)$, with $i \in [1, M]$.

6.4 Numerical Results

In this section, we provide numerical results and illustrate the performance of our proposed system model. Monte-Carlo simulations are carried out and all the outcomes presented are calculated for 10^6 iterations.

In Fig. 6.2 we present the performance of the proposed diplexer-based SWIPT receiver, in terms of SER, by considering $K = 2$ and $K = 4$. Furthermore, we compare it with the performance of the conventional integrated receiver with multiple rectennas. As expected with the increase of the average transmitted power P, the performance for both schemes is enhanced. Furthermore, we note that the performance

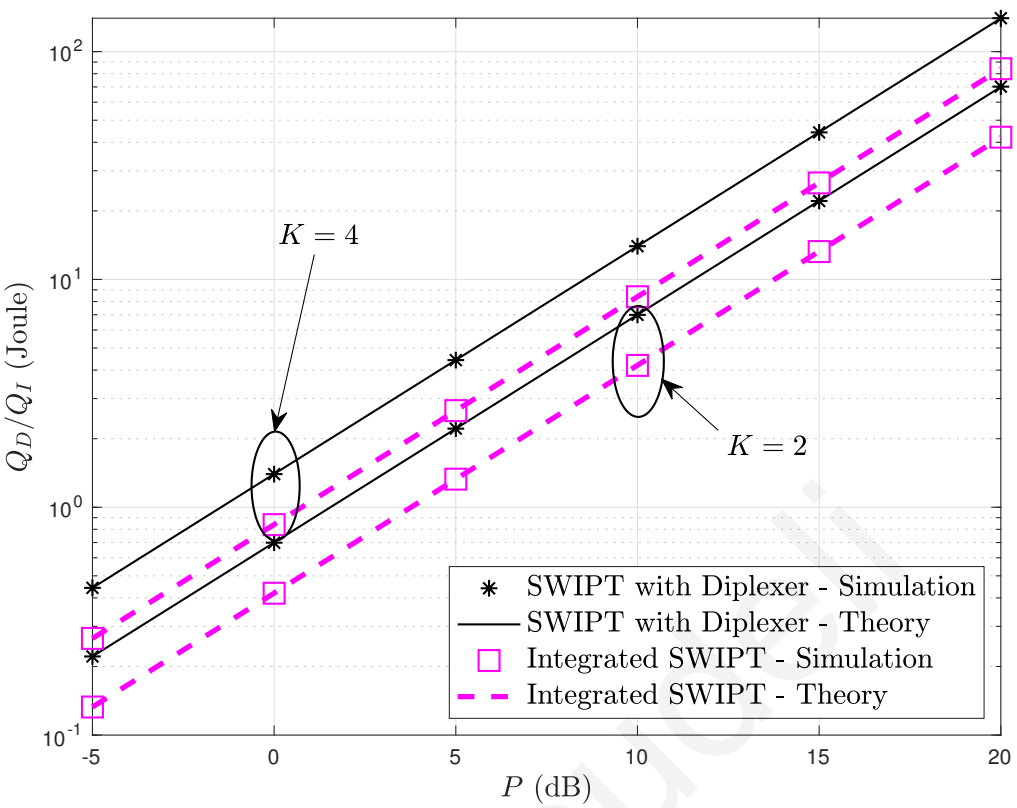

Figure 6.3: EH of the proposed diplexer-based SWIPT receiver compared to conventional integrated SWIPT receiver; $K = 2, 4$ and $\rho = 0.4$.

of the diplexer-based SWIPT receiver is superior, for the same number of receive antennas K. Something that was expected, since in the solution of the integrated receiver, only a portion ρ of the DC power signal is used for ID.

In Fig. 6.3 we illustrate the performance of the proposed SWIPT receiver in terms of EH. We show that the diplexer-based SWIPT receiver enhances the average EH, compared to the integrated SWIPT receiver. This is due to the fact that a portion $(1 - \rho)$ of the DC signal is used for EH, while in the scheme of the diplexer-based solution, the DC output from the first diode is used in the whole.

For the sake of comparison, in Fig. 6.4, we illustrate the performance of the diplexer-based SWIPT receiver, by adopting OOK and PEM, for $M = 2$ and $K = 4$. PEM enhances the average EH, while deteriorates the ID, resulting in error floor.

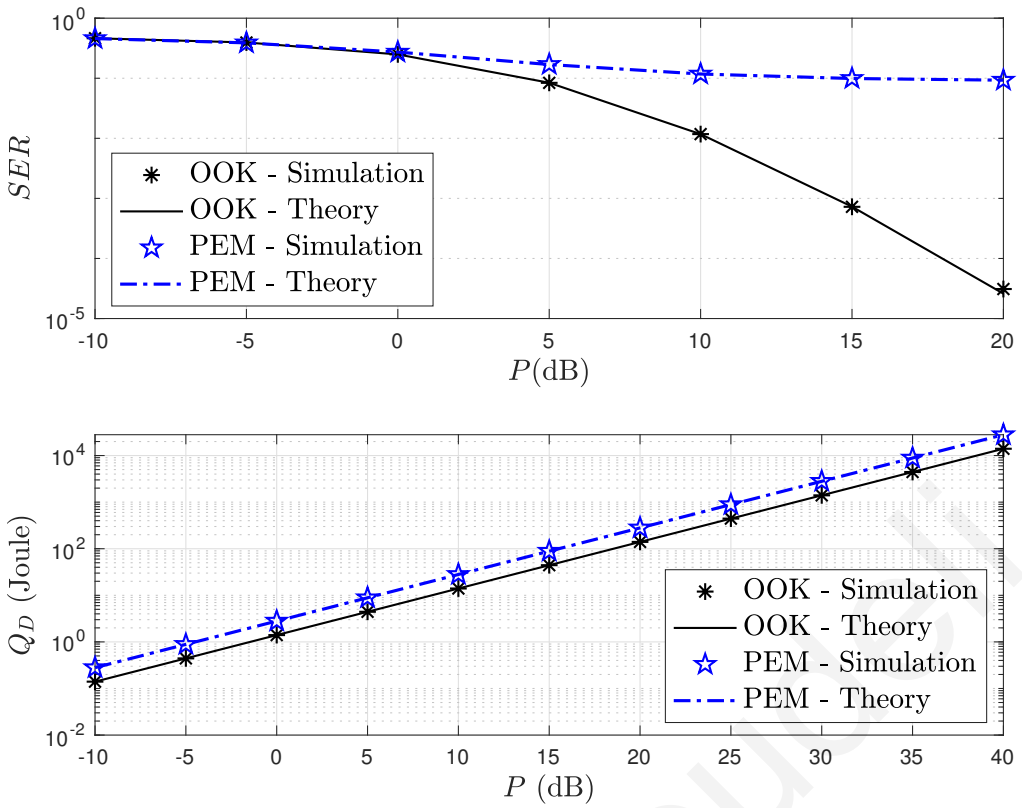

Figure 6.4: SER and Q_D, of the proposed diplexer-based SWIPT receiver for OOK and PEM; $M = 2$ and $K = 4$.

6.5 Conclusion

In this chapter, we study a non-coherent detection scheme for a diplexer-based SWIPT receiver. More specifically, we consider a topology with K receive antennas, each one connected to a diplexer. With the adopted system model, we succeed ID and EH without split of the resources in time, power or spatial domain. Furthermore, with the use of a multiple-antenna receiver, we enhance the performance, both in terms of ID and EH. In addition, we compare the proposed solution to the conventional integrated SWIPT receiver with multiple rectennas, proving the enhanced performance. Finally, energy detection is succeeded, with the use of a ML-based soft decoder, while we compare OOK modulation scheme to PEM. We show that PEM scheme results in enhanced EH, while deteriorates the ID.

Chapter 7

Conclusions and Future Directions

7.1 Concluding Remarks

This dissertation studied several challenges faced in the development of a WIPT system model with enhanced ID and EH. Based on thorough mathematical analysis and numerical evaluations, the proposed architectures, achieve enhanced performance, providing novel solutions for B5G IoT solutions.

First, in Chapter 3, we study a point-to-point integrated SWIPT system model and propose an sophisticated sequential decoder, achieving non-coherent detection. In addition, in Chapter 4 we extend our study of integrated SWIPT receiver by adopting a SIMO topology. We exploit RF and DC combining schemes and we propose a solution that achieves non-coherent energy detection with the use of a ML-based soft decoder. As such, in the first two technical chapters, it is shown that the performance of the conventional single or multiple antenna integrated SWIPT receiver, is enhanced with the use of tools from communication and signal processing theory.

In Chapter 5 we propose a novel BackCom solution with multiple antennas at the BT and prove that with the use of sophisticated physical layer tools the performance of a traditional WPT solution is enhanced. Finally, in Chapter 6, we propose an innovative architecture of SWIPT receiver with diplexer-based multiple-antenna rectification circuits, achieving SWIPT without split of the DC power signal. For all the proposed schemes, enhanced performance in terms of ID and EH is achieved.

Overall, the main concluding remarks are:

- Energy harvesting is the solution to overcome the challenge of limited battery

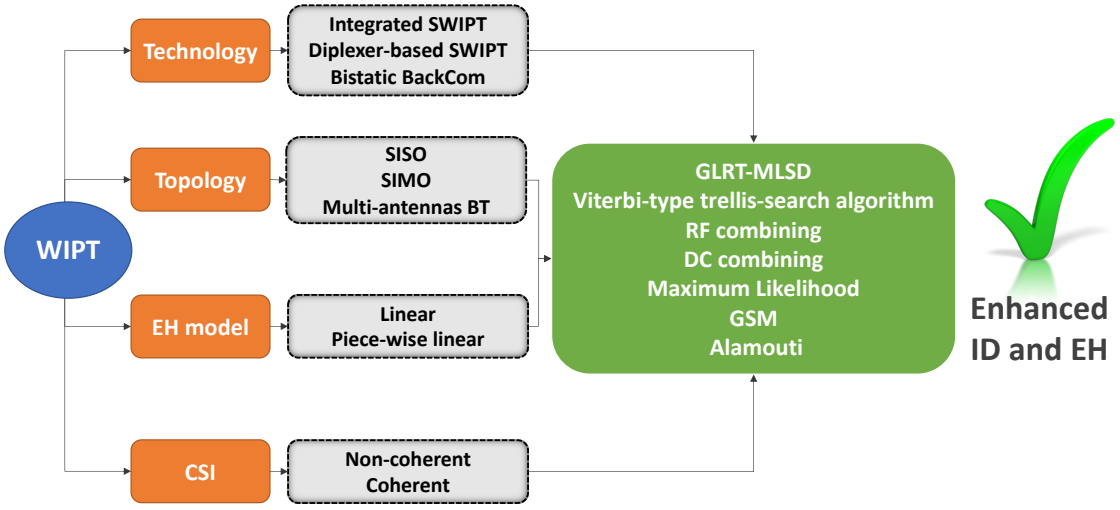

Figure 7.1: Main modules of the PhD dissertation.

lifetime for next generation B5G IoT devices.

- WIPT is one of the promising technologies for handling the explosive growth of IoT, both in terms of information flow and energy sustainability.

- SWIPT and BackCom are key technologies of WIPT and we mainly focus our interest.

- Integrated SWIPT architecture is studied in technical chapters 3 and 4, as an appropriate receiver for B5G IoT solutions. Specifically, the RF to baseband conversion is replaced by a rectenna, which receives and converts the RF signal to DC that is used both for ID and EH. Since, the rectification circuit and LPF are passive devices, the energy consumption for ID is less compared to conventional SWIPT receivers, that first split the RF signal in the power, time or space domain and then convert it to baseband signal used for ID.

- In Chapter 3, we propose a sophisticated sequential single antenna integrated SWIPT receiver. By utilizing tools from communication theory and statistical signal processing, the proposed single-antenna SWIPT architecture achieves enhanced performance compared to conventional power-splitting SWIPT receiver.

- In Chapter 4, we extend our study by investigating a SWIPT architecture with

Device	Requirement
Electronic Watch	1μW
RFID Tag	10μW
Smoke Alarm	1mW
Bluetooth Transceiver	100mW

Figure 7.2: Power requirements for typical B5G IoT devices.

multiple rectennas at the receiver's side. By exploiting RF and DC combining schemes, we enhance ID and EH compared to single antenna receivers. Specifically, the proposed architecture overcomes saturation effects and is appropriate for scenarios with high received energy. A thorough analysis is obtained, offering insights on how the performance is affected from the number of rectifiers and receive antennas, the EH model adopted and the average transmitted power.

- In Chapter 5 we design a novel BackCom system with multiple antennas at the BT. With the use of sophisticated physical layer tools we achieve array gains and ensure diversity. We derive analytical expressions for all the examined techniques and provide tight bounds, along with asymptotical analysis. A comparison to the sequential decoder studied in Chapter 3, is provided.

- In Chapter 6 we study an innovative diplexer-based multiple-rectenna scheme achieving non-coherent detection without splitting the signal in RF or DC domain. The proposed design is compared to conventional integrated SWIPT receiver with multiple rectennas, as a benchmark to the state-of-the-art solutions.

The proposed system models can be adopted from the majority of next generation B5G IoT solutions, covering completely or partially the energy requirements needed (see Fig. 7.2), while at the same time supporting the need of information flow with small data rates.

7.2 Future Work

There are several possible extensions of the work presented in this thesis.

- **Extend current system models:** MIMO systems are attractive to WIPT solutions, in order to enhance the system's overall efficiency. In this PhD dissertation and chapters 3, 4 and 6, the considered adopted topologies are SISO and SIMO, respectively. As such, an interesting direction for future work would be the extension to a MIMO architecture. Specifically, except from the enhanced performance in ID and EH, it could also be examined and taken into consideration the correlation of the received antenna elements. Most previously published works on WIPT networks suppose uncorrelated fading antennas and the impact of arbitrary correlation structure of the antennas on the system performance, has not been thoroughly explored yet. Analyzing the effect of spatial fading correlated antennas on the system performance is of theoretical and practical significance.

  Same approach could be considered for the BackCom topology in chapter 5, considering multiple antennas at the RN. Furthermore, the direct link between the source and the RN was assumed that due to deep scattering and obstacles, was not feasible. The RN in ambient backscatter solutions, suffers from direct link interference from the ambient signals, which adversely affects the detection performance and consequently limits the transmission range. As such, studying the direct link between the source and the RN in our proposed bistatic solution, is an interesting extension for future research.

  Furthermore, the EH SWIPT solutions in chapters 3, 4 and 6, were modeled using a linear or CLC EH model with a constant RF to DC conversion efficiency for a specific range of input RF power. While this assumption may be valid for a certain range, it should be more accurate to capture the rectifier's nonlinearity and the dependence of the harvested DC power on the shape of the input RF signal, by adopting a nonlinear EH model, such as the ones proposed in Appendix A.3.

  Finally, as already described in many parts throughout this PhD dissertation, there are several state-of-the-art experimental setups and prototypes of both WPT and WIPT that validate the theoretical works in the literature [196], [197]. Highlighted key features, such as beamforming, waveform, multiantenna, IRS, channel acquisition, and signal optimization, are developed from different laboratories and universities around the world. An interesting extension of

of this PhD dissertation, is to experimentally validate some of the proposed system models and theoretical results.

- **Machine Learning:** IoT is going to connect billion of devices ranging from high-end devices to sensors, actuators, smartphones, tablets, wearable, home appliances, vehicles, and many more to the Internet [198]. A huge amount of data is generated via such connected devices. In order to extract the relevant hidden knowledge, machine learning is required. Despite advances in communication and optimization theories, many systems subject to nonlinear responses are unknown in terms of their optimal behavior (e.g. capacity) and signal/system design. WPT and WIPT are instances of such systems. Their designs face problems that cannot be mathematically formulated and/or for which no efficient solutions exist. The lack of tractable mathematical models of the rectenna, and more generally of the entire WPT chain (transmitter-receiver, including high power amplifier), as well as algorithms to solve WPT/WIPT signal/system optimizations in general settings is a bottleneck towards efficient WPT/WIPT designs. In this regard, machine learning is instrumental since it can be used to circumvent these modeling and algorithmic challenges.

  Specifically, authors in [199], propose a novel design for a practical rate-splitting multiple access receiver based on model-based deep learning methods, which aims to unite the simple structure of the conventional SIC receiver and the robustness and model agnosticism of deep learning techniques. The proposed receiver is evaluated in terms of symbol error rate, throughput performance and average training overhead. Also, a comparison with the SIC receiver, with perfect and imperfect CSI, is given. Results reveal that the proposed receiver outperforms by a significant margin the SIC receiver with imperfect CSI, due to its ability to generate on demand non-linear symbol detection boundaries in a pure data-driven manner. Furthermore, in [200], authors study a real WPT system which is accomplished in experimental field. The mobile RF wireless transmitter can charge the nearby harvested energy enabled IoT devices, by finding the optimal path to charge them in the optimum time. The reinforcement learning is applied to determine both the order of the IoT devices to be charged and the shortest path for the robot to drive from one IoT device to another. Finally, authors in [201], overview two different design methodologies:

the model and optimize approach relying on analytical system models, modern convex optimization, and communication/information theory, and the learning approach based on data-driven end-to-end learning and physics-based learning. They discuss the pros and cons of each approach, especially when accounting for various nonlinearities in wireless-powered networks, and identify interesting emerging opportunities for the approaches to complement each other.

As such, an interesting approach of this PhD dissertation would be an extension of our proposed system models with the use of machine learning techniques and comparison to the derived performance in terms of ID and EH. Specifically, ML techniques could be used in Chapter 5, at the RN, in order to estimate the CSI and compare it to conventional techniques with the use of training symbols. Furthermore, in Chapter 4, ML could be used at the proposed integrated SWIPT receiver, to estimate and approach a more realistic model for the strong nonlinearities imposed by the rectifiers and the RF-to-DC conversion. In this PhD dissertation a piece-wise linear model is used, taking into consideration the rectifiers' sensitivity and saturation effects along with the average received power.

- **Intelligent Reflecting Surface:** IRS has recently emerged as a promising technique that adapts the propagation environment to enhance the spectrum and energy efficiency. In practice, an IRS consists of multiple individual subwavelength reflecting elements to adjust the amplitude and phase of the incoming signal (i.e., passive beamforming). Different from the relay and backscatter, the IRS assists the primary transmission using passive components with negligible thermal noise but is limited to frequency-dependent reflection. In [126] an IRS-assisted multiple-input single-output (MISO) system and jointly optimized the precoder at the access point and the phase shifts at the IRS to minimize the transmit power. The hardware architecture, design challenges, and application opportunities of practical IRS were covered in [202]. In [203], a prototype IRS with 256 2-bit elements based on positive intrinsic-negative diodes was developed to support real-time video transmission at GHz and mmWave frequency. The authors in [204] propose an IRS-aided SWIPT system where a multi-carrier multi-antenna access point transmits information and power simultaneously,

with the assist of an IRS, to a single-antenna user equipment employing practical receiving schemes. Considering harvester nonlinearity, they characterize the achievable rate-energy region through a joint optimization of waveform, active and passive beamforming based on the CSI at the transmitter. [205], authors discuss how IRS can be incorporated in BackCom system to realize the future green and ubiquitous communication for IoT applications.

As such, IRS can be incorporated in SWIPT and BackCom solutions, while an interesting future direction of this dissertation, would be to elaborate on the potential improvements than can be achieved. In general, IRS could be used likewise as the multi-antenna solutions that we introduced, to overcome short coverage, enhance transmission range, improve energy efficiency achieving higher performance gains and enhance the detection performance at the receiver. The proposed system model in Chapter 5, could replace the multi-antenna BT with the use of an IRS and compare the two solutions in terms of EH. Furthermore, the enormous passive beamforming gains brought by IRS highly depend on the availability of CSI, which is quite challenging to acquire since passive IRS elements and backscatter devices lack signal processing capabilities. Thus, only the DBC can be estimated at the backscatter receiver, which makes the channel estimation schemes available for conventional IRS-assisted systems inapplicable. Therefore, novel schemes need to be developed for channel estimation , which may be combined with ML techniques, as mentioned in the previous point.

Appendix A

A.1 Separated receiver architectures

Time Domain (TS): As shown in Fig. 1.4 i), the SWIPT receiver switches in time between ID and EH [206]. In this case, the signal splitting is performed in the time domain and thus the entire signal received in one time slot is used either for information decoding or power transfer. The TS scheme is simple for hardware implementation at the receiver but it requires accurate time synchronization with the transmitter to avoid possible information loss. Furthermore, the switching in time is governed by a scheduling algorithm that is synchronized with the transmitter and is typically based on the channel quality [207], [208].

Power Domain (DPS): As shown in Fig. 1.4 ii), the SWIPT receiving antenna is connected to a power splitter, which splits the received signal into two streams of different power level. Specifically, one stream with power level, $1-\rho$, is fed to the energy harvester and the rest of the stream with power level, ρ, is fed to the information decoder. Unlike the TS scheme, the DPS allows simultaneous information decoding and energy harvesting. Therefore, it is more suitable for applications with critical information/energy or delay constraints. The PS ratio may be adapted based on the CSI at the tag [148]. However, a power splitter with a dynamically adjustable PS ratio is more difficult to realize, compared to dynamically adjusting the TS of a SWIPT receiver.

Spatial Domain (AS): As shown in Fig. 1.4 iii), the AS scheme dynamically switches each antenna element between decoding/harvesting to achieve SWIPT in the spatial domain. These connections dynamically change based on the channel variations [209]. The input signals are then combined via an RF combiner for the information decoder and via an RF or DC combiner for the energy harvester [88], [210].

AS is easy to implement but it is necessary to use multiple antennas at the tag, which may not be feasible for small wireless powered devices such as sensors. Furthermore, the AS scheme requires the solution of an optimization problem, in order to decide the optimal assignment of the antenna elements for ID and EH. Therefore, optimal AS suffers from high complexity. As a consequence, low-complexity AS mechanisms have been devised which use the principles of generalized selection combining (GSC) [209].

A.2 Receiver using RF diplexer

In this section, we show how the same RF received signal can be used to both harvest energy and decode information. The key this implementation is the use of RF diplexers that implement frequency-domain multiplexing. Diplexers are common and important devices in wireless system front-end circuits. However, they are usually used to allow two radio receivers to operate simultaneously on different, widely separated, frequency bands [211]. In SWIPT, the requirement is different: the low frequency signals should be separated from higher frequency signals, as such the low-pass band-pass diplexers are needed.

Assume that two ports (e.g., L and H) are multiplexed onto a third port (e.g., S). The signals on ports L and H occupy disjoint frequency bands. Consequently, the signals on L and H can coexist on port S without interfering with each other. Note that a diplexer is a different device from a power splitter. The ports of a diplexer are frequency selective; the ports of a splitter are not. There is also a power loss difference - a power splitter takes all the power delivered and equally divides it between the output ports. A diplexer does not.

By reversing the input and output of RF diplexers allow us to separate the low frequency signals from higher frequency signals as depicted in the diplexer-based receiver in Fig.1.6. By substituting the down-convertor by dual diode, the receiver architecture consumes less power by avoiding the use of active components, which is critical for low-power consumption communication networks.

A.3 Non-linear EH models

The following described EH models aim at providing mathematical tools that help in the design and/or analysis of WIPT systems, taking into consideration the non-linearity imposed by the rectifiers.

- **Nonlinear Normalized Sigmoid Model:** The model was proposed and explored in [212] - [216] and it does not account for harvesters' sensitivity. The harvested power is expressed by a sigmoid model as

$$P_{\mathrm{DC}} \triangleq \frac{\frac{c_0}{1+\exp\left(-a_0(P_{\mathrm{RF}}-b_0)\right)}-\frac{c_0}{1+\exp\left(a_0 b_0\right)}}{1-\frac{1}{1+\exp\left(a_0 b_0\right)}}. \tag{A.1}$$

  The P_{DC} is determined by three real numbers a_0, b_0, and c_0, that capture the joint effects of various nonlinear phenomena caused by the rectifying circuit and control the steepness of the linear model between P_{DC} and P_{RF}. A similar, sigmoid model accounting however for P_{sen} was proposed in [217], where the harvested power is modeled as

$$P_{\mathrm{DC}} \triangleq \max\left\{\frac{c_1}{\exp\left(-a_1 P_{\mathrm{sen}}+b_1\right)}\left(\frac{1+\exp\left(-a_1 P_{\mathrm{sen}}+b_1\right)}{1+\exp\left(-a_1 P_{\mathrm{RF}}+b_1\right)}-1\right), 0\right\}. \tag{A.2}$$

- **Second Order Polynomial Model:** This model is based on a second degree polynomial [218]. The harvested power can be expressed as

$$P_{\mathrm{DC}} \triangleq a_2 P_{\mathrm{RF}}^2 + b_2 P_{\mathrm{RF}} + c_2. \tag{A.3}$$

  In order for the model to encompass the sensitivity of the rectifier, it can be modified as

$$P_{\mathrm{DC}} \triangleq a_3 (P_{\mathrm{RF}} - P_{\mathrm{sen}})^2 + b_3 (P_{\mathrm{RF}} - P_{\mathrm{sen}}). \tag{A.4}$$

  The parameters of the model are a_3, b_3 and P_{sen}.

- **Curve Fitting Models:** In [219], after examining dozens of practical energy harvesters, the power conversion efficiency of the energy harvester was given as a function of the input power $h(P_{\mathrm{RF}}) = \frac{p_2 P_{\mathrm{RF}}^2 + p_1 P_{\mathrm{RF}} + p_0}{q_3 P_{\mathrm{RF}}^3 + q_2 P_{\mathrm{RF}}^2 + q_1 P_{\mathrm{RF}} + q_0}$, where $p_0, p_1, p_2, q_0, q_1, q_2, q_3$ are constants determined by curve- fitting. Thus, the input-output relationship will be

$$P_{\mathrm{DC}} \triangleq \frac{p_2 P_{\mathrm{RF}}^3 + p_1 P_{\mathrm{RF}}^2 + p_0 P_{\mathrm{RF}}}{q_3 P_{\mathrm{RF}}^3 + q_2 P_{\mathrm{RF}}^2 + q_1 P_{\mathrm{RF}} + q_0}. \tag{A.5}$$

Unlike the linear model where the output power increases linearly with the input power, the output power of the nonlinear model actually approaches an upper limit of p_2/q_3 when the input power increases, due to the nonlinear distortion or saturation. However, this model is not mathematically tractable for the derivations of the pdf and the cumulative distribution function (CDF). Thus, authors in [220] propose a simpler nonlinear model as

$$P_{\text{DC}} \triangleq \frac{\alpha P_{\text{RF}} + b}{P_{\text{RF}} + c} - \frac{b}{c}, \tag{A.6}$$

where α, b, c are constants determined by standard curve fitting, similar to [219].

- **Piece-Wise Linear Models:** In [221] several piece-wise linear EH models are investigated. In the literature it has been shown [222], that a piece-wise linear EH model divides the RF-to-DC power transfer function into a constant zero DC output that accounts for the rectifier's sensitivity, a linear region, and potentially a constant saturation region, as follows

$$P_{\text{DC}} \triangleq \begin{cases} 0, & \text{if } P_{\text{RF}} < P_{\text{sen}}, \\ \zeta(P_{\text{RF}} - P_{\text{sen}}), & \text{if } P_{\text{sen}} \leq P_{\text{RF}} < P_{\text{sat}}, \\ \zeta(P_{\text{sat}} - P_{\text{sen}}), & \text{if } P_{\text{sat}} \leq P_{\text{RF}}. \end{cases} \tag{A.7}$$

This can be generalized to a piece-wise linear model with as many linear regions as needed to fit a certain simulated/measured circuit response [160]. Modeling is done through points between harvester's sensitivity and saturation characteristics. Given a set of $J+1$ data pairs of input power and corresponding harvested power, denoted as $\{q_j\}_{j=0}^{J}$ and $\{v_j\}_{j=0}^{J}$, respectively, slopes $l_j \triangleq \frac{v_j - v_{j-1}}{q_j - q_{j-1}}$, $j \in [J]$ are defined, where $[J] \triangleq \{1, 2, ..., J\}$. Modeling sensitivity and saturation characteristics is done through points $q_0 = P_{\text{sen}}$ and $q_J = P_{\text{sat}}$. Having those slopes, the harvested power is given by

$$P_{\text{DC}} \triangleq \begin{cases} 0, & \text{if } P_{\text{RF}} \in [0, q_0], \\ l_j(P_{\text{RF}} - q_{j-1}) + v_{j-1}, & \text{if } P_{\text{RF}} \in (q_{j-1}, q_j],\ \forall j\ in [J] \\ v_j, & \text{if } P_{\text{RF}}\ \in [q_J, \infty). \end{cases} \tag{A.8}$$

The energy harvested is defined using $2(J+1)$ real numbers, easily available from harvesters' specifications; thus, determining energy harvested is straightforward, without any tuning.

A.4 Diode's Main Circuit Parameters

Diode's Turn-on (Threshold) Voltage: The turn-on or threshold voltage of a diode is the built-in voltage barrier in the diode junction. Only when the voltage drop across the diode junction is larger than the diode's turn-on voltage, the diode conducts current. Among the most common diodes is the Schottky [224]. In this thesis, we refer to this threshold as a sensitivity level.

Diode's Saturation Current: The diode's saturation current is a very small amount of leakage current that flows through the diode in the reverse direction. Basically, it is the limiting current such that further increase of voltage produces no further increase in current [225]. In this thesis, we refer to this threshold as a saturation level.

Diode's Reverse Breakdown Voltage: When the reverse-bias voltage across the diode junction exceeds the diode's reverse breakdown voltage, a significant amount of reverse current will pass through the diode. This mode of operation is known as breakdown region of the diode.

Diode's Internal Resistance: A diode is characterized by an internal resistance which is in series with the diode's junction. Part of the power flowing through the diode dissipates in this resistance.

Diode's Junction Capacitance: A diode includes a junction capacitance which is in parallel to the diode's junction. The diode's junction capacitance limits its maximum operating frequency.

A.5 Viterbi Algortithm

A maximum-likelihood detector searches over all possible input sequences using an efficient recursive algorithm known as the Viterbi algorithm. A trellis is used to represent all possible input sequences, as shown in Fig. A.1. Each path through the trellis represents a different binary input sequence. A trellis that extends for n sampling times contains unique paths for all 2^n possible input sequences.

Each branch in the trellis has associated with it an input symbol x_i, an ideal value y_i, and a branch metric equal to $(r_i – y_i)^2$. The sum of the branch metrics along a path, referred to as the path metric, represents the squared Euclidean distance between the received samples and the ideal samples associated with that path. The

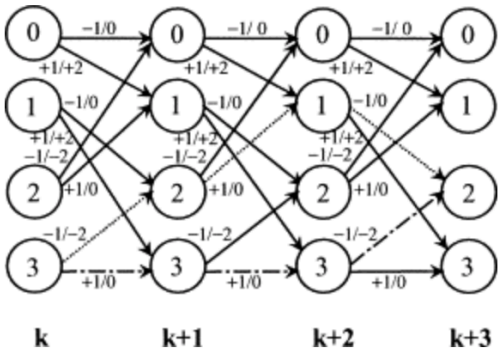

Figure A.1: A four-state trellis diagram.

branch metrics can be simplified by noting that r_i^2 is common to all the branch metrics. Consequently, minimizing the squared Euclidean distance is equivalent to minimizing:

$$\sum_{i=1}^{n}(r_i - y_i)^2 - r_i^2 = \sum_{i=1}^{n} 2r_i y_i + y_i^2. \tag{A.9}$$

The Viterbi algorithm systematically eliminates those paths that cannot be part of the most likely path because they diverge and remerge with another path that has a smaller path metric. Since all other paths have been eliminated, a ML detector only needs to keep track of the minimum metric path leading to each state at the current sampling time. The metric of the minimum metric path is commonly referred to as the state metric. When the current sample is received, path metrics for the two paths leaving each state at the previous sampling time are calculated by adding branch metrics to state metrics. Then, the two path metrics entering each state at the current sampling time are compared and the path with the minimum metric is selected as the survivor path. After all n samples have been received, the path with the overall minimum path metric is selected as the most likely path and the input sequence associated with that path is the maximum-likelihood sequence estimate $\tilde{x}$.

A.6 Maximum Likelihood

In statistics, maximum likelihood estimation is a method of estimating the parameters of a probability distribution by maximizing a likelihood function, so that under the assumed statistical model the observed data is most probable. The point in the parameter space that maximizes the likelihood function is called the maximum

likelihood estimate. The ML detector is a special case of the maximum a posteriori probability detector, which is the optimum decision rule based on the observation vector $\mathbf{y}$. The a posteriori probabilities are defined as

$$p(\mathbf{s}|\mathbf{y}), \forall \mathbf{s} \in \mathbf{S}, \tag{A.10}$$

where $\mathbf{S}$ is the modulation alphabet. The maximum a posteriori probability detector is based on the selection of the signal that yields the maximum a posteriori portability. From Bayes rule we have that

$$p(\mathbf{s}|\mathbf{z}) = \frac{f(\mathbf{y}|\mathbf{s})p(\mathbf{s})}{f(\mathbf{y})}, \tag{A.11}$$

where $f(\mathbf{y}|\mathbf{s})$ is the probability density that a specific $\mathbf{s}$ will lead to the observation $\mathbf{y}$. If we assume that the a priory probability $p(\mathbf{s})$, that a specific $\mathbf{s}$ was sent, is constant for any $\mathbf{s}$, i.e. $\mathbf{s}$ is uniformly distributed, the computation of the a posteriori probabilities depends only on the conditional densities $f(\mathbf{y}|\mathbf{s})$, since the probability density $f(\mathbf{s})$ is fixed for a given $\mathbf{s}$. The ML criterion is based on the selection of the signal that yields the maximum conditioned density $f(\mathbf{y}|\mathbf{s})$. Consequently, for uniform $\mathbf{s}$, we have that

$$\hat{\mathbf{s}}_{\mathrm{ML}} = \underset{\mathbf{s}\in\mathbf{S}}{\mathrm{argmax}} p(\mathbf{s}|\mathbf{y}) = \underset{\mathbf{s}\in\mathbf{S}}{\mathrm{argmax}} f(\mathbf{y}|\mathbf{s}), \tag{A.12}$$

and the ML and maximum a posteriori probability detectors are equal.

A.7 Alamouti scheme

The most basic form of the Alamouti scheme is designed to transmit symbols using two transmit antennas to a single receive antenna, as illustrated in Fig. A.2.

Table A.1: Alamouti space-timecoding.

Transmit time	**Antenna** 1	**Antenna** 2
t	s_1	s_2
$t + T_s$	$-s_2^*$	s_1^*

Alamouti space-time coding is defined in Table A.1. This table shows how a sequence of two symbols, s_1 and s_2, is encoded using Alamouti coding. At some instant of time, t, symbol s_1 is transmitted from transmit antenna 1 and symbol s_2 is transmitted from the second transmit antenna. During the next symbol interval

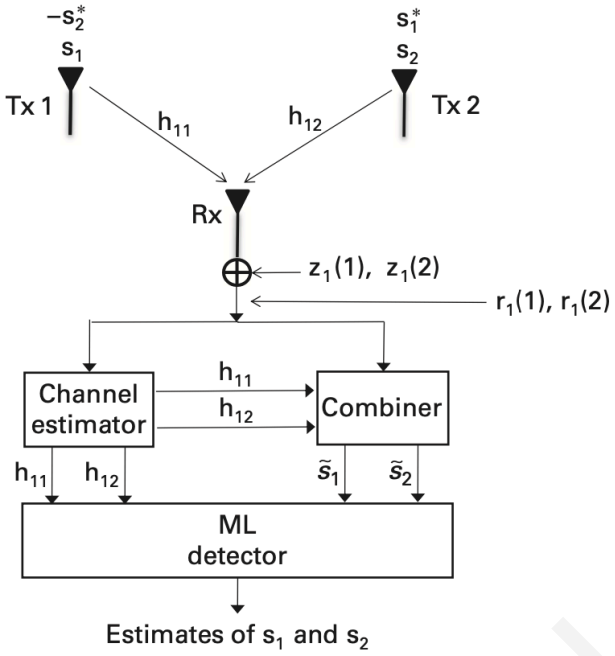

Figure A.2: A 2×1 Alamouti communication system.

period at time $t + T_s$, the symbols $-s_2^*$ and s_1^* are transmitted from antennas 1 and 2, respectively. This demonstrates how Alamouti coding involves coding in both the spatial and time dimensions; hence, it is an example of a space-time code.

Appendix B

B.1 Calculation of probability of error

The probability of error deciding symbol x_{i+1} when symbol x_i is transmitted, is directly related with the probability that the received signal $y_{x_{i+1}}$ is higher than y_{x_i}, which results in

$$f_Y(y_{x_i}) \leq f_Y(y_{x_{i+1}}), \tag{B.1}$$

where $f_Y(y_{x_i})$ denotes the pdf of the received signal y. From (3.5), the channel power gain follows an exponential distribution and the rectifier noise follows a normal distribution. Therefore, y follows an exponentially modified Gaussian (EMG) distribution, with pdf [223]

$$f_Y(y_{x_i}) = \frac{\lambda_i}{2} \exp\left(\frac{\lambda_i}{2}\left(2\mu + \lambda_i\sigma^2 - 2y_{x_i}\right)\right) \times \operatorname{erfc}\left(\frac{\mu + \lambda_i\sigma^2 - y_{x_i}}{\sqrt{2}\sigma}\right), \tag{B.2}$$

where μ and σ^2 are the mean and the variance of the Gaussian component, respectively. In our case $\mu = 0$ and $\sigma^2 = 1/2$, since we are interested only in the real part of the complex Gaussian noise n_2. Furthermore, we assume that the symbols x_i are equally probable transmitted and λ_i is the rate of the exponential component, which in our case is $\lambda_i = \frac{1}{(2E_{\text{ave}}x_i^2)}$.

In order to define $P(e_{i\to i+1})$, when $i < M$, we need to calculate the probability of (B.1). Consequently,

$$P(e_{i\to i+1}) = \int_{c_1}^{\infty} f_Y(y_{x_i}) dy_{x_i}, \tag{B.3}$$

where c_1 is derived when equality holds for (B.1). In other words, c_1 returns the value of y, where the pdfs of the received signals for the transmitted symbols x_i and x_{i+1} intersect. Respectively, for $i > 1$, $P(e_{i\to i-1})$ can be calculated as

$$P(e_{i\to i-1}) = \int_{0}^{c_2} f_Y(y_{x_i}) dy_{x_i}, \tag{B.4}$$

subject to $f_Y(y_{x_i}) \leq f_Y(y_{x_{i-1}})$ and given that c_2 is derived when equality holds.

B.2 Proof of Theorem 1

From (6.15) and taking into consideration the cumulative density function, we herein calculate the probabilities regarding the DC output from an antenna i. Specifically, the probability of DC output being in the sensitivity area is calculated by taking into consideration that the received RF power signal is less than the sensitivity level, $u_{\min}$, therefore the rectifier is not activated resulting in $k_i = 0$. As such

$$\mathbb{P}(u_i^{\mathrm{DC}} < u_{\min}) = F_{u_i^{\mathrm{DC}}}(u_{\min}) = 1 - e^{-\lambda_x^{\mathrm{DC}} u_{\min}}. \tag{B.5}$$

Furthermore, the probability of the DC output belonging to the linear area, is interwoven with the probability that the received RF power signal is higher than the sensitivity level, $u_{\min}$ and less than the saturation level, $u_{\max}$. As such, based on the level of the received power signal $k_{l_i} \in [1, K]$ rectifiers are activated. Therefore

$$\begin{aligned}\mathbb{P}\Big(u_{\min} + (k_{l_i} - 1)u_{\max} \leq u_i^{\mathrm{DC}} < k_{l_i} u_{\max}\Big) &= F_{u_i^{\mathrm{DC}}}(u_{\max}) - F_{u_i^{\mathrm{DC}}}(u_{\min}) \\ &= e^{-\lambda_x^{\mathrm{DC}} k_{l_i} u_{\max}}\Big(e^{-\lambda_x^{\mathrm{DC}}(u_{\min} - u_{\max})} - 1\Big).\end{aligned} \tag{B.6}$$

In addition, the probability that the received RF power signal is at such levels that results in activating $k_{s_i} \in [1, K-1]$ rectifiers in the saturation area, is calculated as

$$\begin{aligned}\mathbb{P}\Big(k_{s_i} u_{\max} \leq u_i^{\mathrm{DC}} < k_{s_i} u_{\max} + u_{\min}\Big) &= F_{u_i^{\mathrm{DC}}}(u_{\max} + u_{\min}) - F_{u_i^{\mathrm{DC}}}(u_{\max}) \\ &= e^{-\lambda_x^{\mathrm{DC}} k_{s_i} u_{\max}}\Big(1 - e^{-\lambda_x^{\mathrm{DC}} u_{\min}}\Big).\end{aligned} \tag{B.7}$$

Finally, the probability of activating all the rectifiers in the saturation area follows

$$\mathbb{P}(K u_{\max} \leq u_i^{\mathrm{DC}}) = \overline{F}_{u_i^{\mathrm{DC}}}(K u_{\max}) = e^{-\lambda_x^{\mathrm{DC}} K u_{\max}}. \tag{B.8}$$

Therefore the probability regarding the DC outputs from N receive antennas, given that x was transmitted and assuming that N_{sen} out of N antennas are in the sensitivity area, N_{L} out of N antennas in the linear area, N_{sat1} and N_{sat2} out of N antennas in the saturation area, follows

$$\begin{aligned}P_N(x) = &\Big(\mathbb{P}(u_i^{\mathrm{DC}} < u_{\min})\Big)^{N_{\mathrm{sen}}}\Big(\mathbb{P}(K u_{\max} \leq u_i^{\mathrm{DC}})\Big)^{N_{\mathrm{sat2}}} \\ &\times \prod_{l_i=1}^{N_{\mathrm{L}}} \mathbb{P}\Big(u_{\min} + (k_{l_i} - 1)u_{\max} \leq u_i^{\mathrm{DC}} < k_{l_i} u_{\max}\Big) \\ &\times \prod_{s_i=1}^{N_{\mathrm{sat1}}} \mathbb{P}\Big(k_{s_i} u_{\max} \leq u_i^{\mathrm{DC}} < k_{s_i} u_{\max} + u_{\min}\Big).\end{aligned} \tag{B.9}$$

With the use of probabilities from (B.5), (B.6), (B.7), (B.8) and the appropriate calculations, we derive (4.21) in Theorem 1.

B.3 Proof of Theorem 2

From (4.24) and (4.25), it is clearly noticed that z is the sum of N_{L} independent and identically distributed random variables. Furthermore, these variables are exponentially distributed with the same rate parameter, i.e. λ_x^{DC}. As such, by considering [226, Ch.1.8.7], we conclude that z follows the Erlang distribution, which results in

$$\mathbb{P}(Z < z_k) = \int_{z_{\min}}^{z_k} \frac{\left(\lambda_x^{\mathrm{DC}}\right)^{N_{\mathrm{L}}}(z - z_{\min})^{N_{\mathrm{L}}-1}}{\Gamma(N_{\mathrm{L}})} e^{-\lambda_x^{\mathrm{DC}} z} dz \overset{(a)}{=} \frac{e^{-\lambda_x^{\mathrm{DC}} z_{\min}}}{\Gamma(N_{\mathrm{L}})} \gamma\Big(N_{\mathrm{L}}, \lambda_x^{\mathrm{DC}}(z_k - z_{\min})\Big), \tag{B.10}$$

and

$$\mathbb{P}(Z > z_k) = \int_{z_k}^{z_{\max}} \frac{(\lambda_x^{\mathrm{DC}})^{N_{\mathrm{L}}}(z_{\max} - z)^{N_{\mathrm{L}}-1}}{\Gamma(N_{\mathrm{L}})} e^{-\lambda_x^{\mathrm{DC}} z} dz \overset{(b)}{=} \frac{e^{-\lambda_x^{\mathrm{DC}} z_{\max}}}{\Gamma(N_{\mathrm{L}})} \gamma\Big(N_{\mathrm{L}}, \lambda_x^{\mathrm{DC}}(z_{\max} - z_k)\Big), \tag{B.11}$$

where (a) and (b) follow from integrating by substituting variables $z - z_{\min}$ and $z_{\max} - z$ with variable w, respectively. Furthermore

$$z_{\min} = N_{\mathrm{L}} u_{\min} + \sum_{l_i=1}^{N_{\mathrm{L}}} (k_{l_i} - 1) u_{\max}, \tag{B.12}$$

$$z_{\max} = \sum_{l_i=1}^{N_{\mathrm{L}}} k_{l_i} u_{\max}, \tag{B.13}$$

$$z_k = k_{l_1} u_{\max} + \sum_{l_i=2}^{N_{\mathrm{L}}} \Big(u_{\min} + (k_{l_i} - 1) u_{\max}\Big), \tag{B.14}$$

while z_k follows from the individual limits of each independent random variable u_{l_i} in the sum of z. Taking into consideration that $1 \leq N_L \leq N$ and $k_{l_i} \in [1, K]$ we define

$$u_{\min} \leq z_{\min} \leq N u_{\min} + N(K-1) u_{\max}, \tag{B.15}$$

$$u_{\min} + u_{\max} \leq z_{\max} \leq NK u_{\max}, \tag{B.16}$$

$$u_{\min} + u_{\max} \leq z_k \leq NK u_{\max} - (N-1)(u_{\max} - u_{\min}). \tag{B.17}$$

Consequently, depending on the values of t from (4.25), we proceed accordingly with the calculation of probability of error for z, i.e. $P_{e,z}(x)$. Specifically, we recognize the following two cases.

- if $z_{\min} < t \leq z_k$: The probability of error is

$$P_{e,z}(0) \overset{(c)}{=} \mathbb{P}(t < z \leq z_k | x = 0) \overset{(d)}{+} \mathbb{P}(z_k < z \leq z_{\max} | x = 0), \tag{B.18}$$

and

$$P_{e,z}(1) \overset{(c)}{=} \mathbb{P}(z_{\min} < z \leq t | x = 1), \tag{B.19}$$

where (c) follows from (B.10) and (d) from (B.11).

- if $z_k < t \leq z_{\max}$: The probability of error is

$$P_{e,z}(0) \overset{(e)}{=} \mathbb{P}(t < z \leq z_{\max} | x = 0), \tag{B.20}$$

and

$$P_{e,z}(1) \overset{(f)}{=} \mathbb{P}(z_{\min} < z \leq z_k | x = 1) \overset{(e)}{+} \mathbb{P}(z_k < z \leq t | x = 1), \tag{B.21}$$

where (e) follows from (B.11) and (f) from (B.10).

Therefore, by taking into consideration the transmitted symbol x, the ML criterion and all possible combinations and ordering of $N_{\text{sen}}, N_{\text{L}}, N_{\text{sat1}}, N_{\text{sat2}}$, the total probability of error is calculated as follows

$$\begin{aligned} P_e^{\text{DC}} &= \mathbb{P}(x = 0) \sum_{m=1}^{M} C_m P_{e,z}(0) \prod_{s_i=1}^{N_{\text{sat1}}} \mathbb{P}\left(k_{s_i} u_{\max} \leq u_i^{\text{DC}} < k_{s_i} u_{\max} + u_{\min}\right) \\ &\times \left(\mathbb{P}(u_i^{\text{DC}} < u_{\min})\right)^{N_{\text{sen}}} \left(\mathbb{P}(K u_{\max} \leq u_i^{\text{DC}})\right)^{N_{\text{sat2}}} \\ &+ \mathbb{P}(x = 1) \sum_{m=1}^{M} C_m P_{e,z}(1) \prod_{s_i=1}^{N_{\text{sat1}}} \mathbb{P}\left(k_{s_i} u_{\max} \leq u_i^{\text{DC}} < k_{s_i} u_{\max} + u_{\min}\right) \\ &\times \left(\mathbb{P}(u_i^{\text{DC}} < u_{\min})\right)^{N_{\text{sen}}} \left(\mathbb{P}(K u_{\max} \leq u_i^{\text{DC}})\right)^{N_{\text{sat2}}}. \end{aligned} \tag{B.22}$$

Then, the final expression in Theorem 2 can be easily obtained, by taking into consideration $P_{e,z}(x)$ from (B.18), (B.19), (B.20) and (B.21), with the appropriate substitutions from (B.5), (B.7), (B.8) and (B.10) or (B.11).

B.4 Proof of Theorem 3

By taking into consideration (4.31), the probability of error is given by

$$\begin{aligned} P_e^{\text{RF}} &= \mathbb{P}(u^{\text{RF}} > z_{\text{RF}} | x = 0) + \mathbb{P}(u^{\text{RF}} < z_{\text{RF}} | x = 1) \\ &\overset{(g)}{=} \mathbb{P}(u^{\text{RF}} < u_{\min} | x = 1) \overset{(h)}{+} \sum_{k=1}^{K} \mathbb{P}((k-1) u_{\max} + u_{\min} \leq u^{\text{RF}} < z_{\text{RF}} | x = 1) \end{aligned}$$

$$+\sum_{k=1}^{K}\mathbb{P}(z_{\mathrm{RF}}\leq u_{\mathrm{RF}}<ku_{\max}|x=0)\overset{(i)}{+}\sum_{k=1}^{K-1}\mathbb{P}(ku_{\max}\leq u^{\mathrm{RF}}<ku_{\max}+u_{\min}|x=\tilde{x}')$$
$$+\mathbb{P}(u^{\mathrm{RF}}>Ku_{\max}|x=0), \tag{B.23}$$

where (g) follows considering that the DC output signal is in the sensitivity area, (h) in the linear, and (i) in the saturation area. With the use of (B.5), (B.6), (B.7), (B.8) and the appropriate calculations, Theorem 3 is derived.

B.5 Experimental Results

For the comparison with the theoretical model presented in Chapter 4, the circuits for N = 1, K = 1, 2 were experimentally tested using voltage doubler topologies. The implementation was achieved by the lab of antennas and microwaves of Frederick university, who herein provided us with the following experimental results. The research group's objective is to advance research and education in the areas of microwave/RF circuits, antennas and applied electromagnetics. They focus on applying fundamental principles to practical problems related to communications, Biomedicine and sensing. The experimental results provided, were co-funded from EXCELLENCE/1216/0376 (SWITCH) project.

Specifically, for $K = 2$, a $3dB$ Wilkinson power divider was used and for the single and dual branch rectifiers, a low loss substrate, Rogers RT/duroid 5880. Lumped components available in Colilcraft's ADS library were used to match the rectifiers in the ISM band. The circuits can be seen in Fig. B.1. For testing purpose, the $R\&S®SMF100A$ microwave signal generator was connected directly to the input of the circuit and was used to generate the input signals. The input OOK signal with AWGN was created from the generator and the rectified DC voltage was measured on the optimized ohmic load using a DMM. The efficiency was measured on the optimized load for $N = K = 1$ and for $N = 1$ and $K = 2$ when a voltage combiner, Fig. B.2 topology was used for the termination load.

The measured results in Fig. B.1, indicate that the efficiency depends on the input power non-linearly. As expected there is a peak value before the saturation voltage and subsequently, the efficiency drops rapidly. The nonlinear dependence of the efficiency with respect to the input power is the main cause of the discrepancies between the theoretical model which uses a fixed efficiency, $\alpha = 0.7$, and the

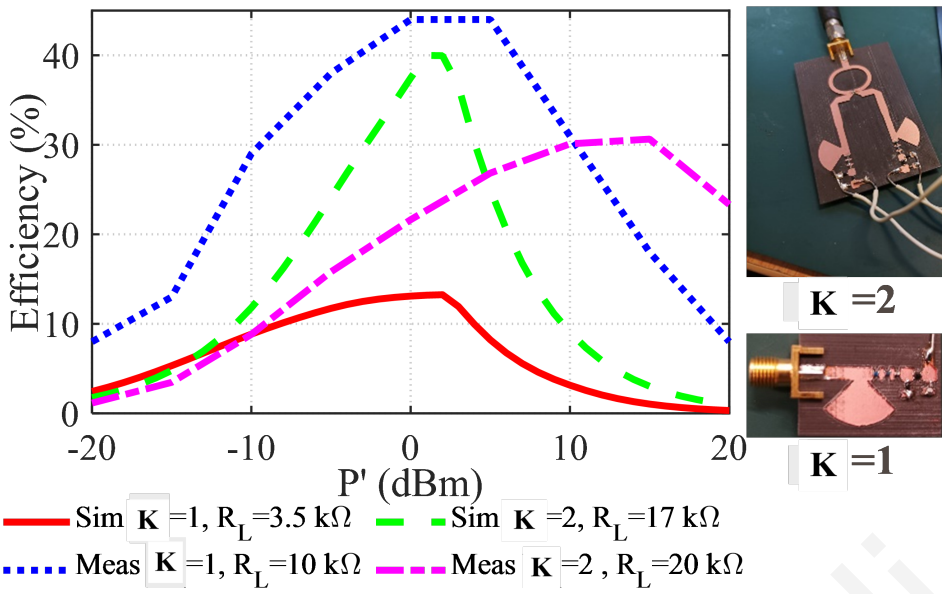

Figure B.1: Comparison of efficiencies.

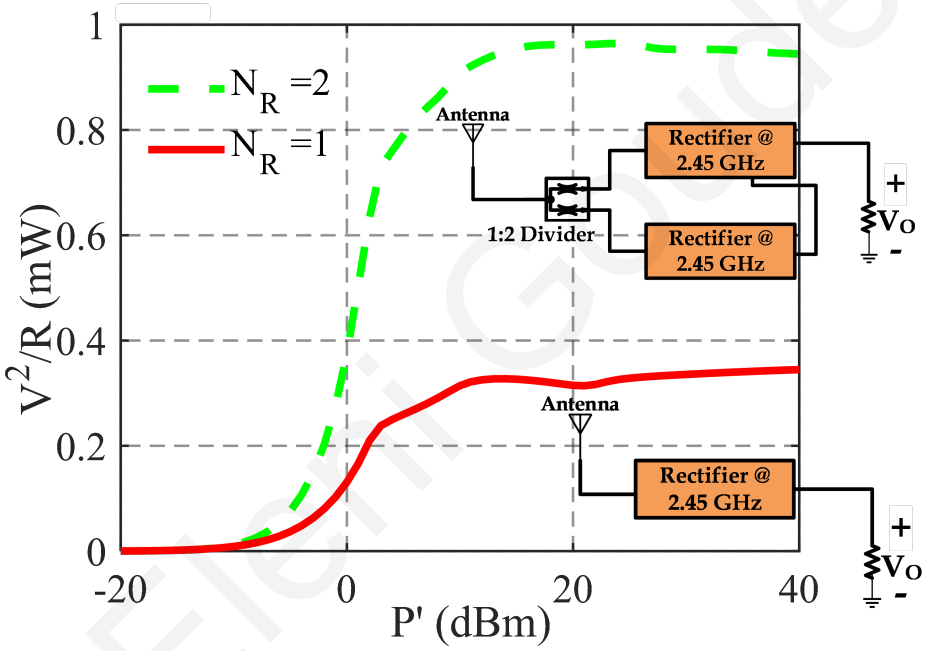

Figure B.2: Output power of circuit for $N = 1, K = 1, 2$.

measurements where the non-linearity of the efficiency prevails. Fig. B.2 presents the simulated rectified DC power on selected termination loads which has consistent behavior with the numerical results presented in Fig. 4.4. Eventually, after the saturation of the rectified voltage, the DC power for $N = 1, K = 2$ is approximately double the power for the $N = 1, K = 1$ case.

B.6 Proof of Proposition 4

Substituting (5.16) and (5.17) into (5.15), and assuming for a given DBC

$$\Pr(x_\ell \to \hat{x}_{\hat{\ell}}|F_\ell) = \Pr\left(\|n\|^2 > \left\| n + \sqrt{P}\left(\sum_{i=1}^{L_u} h_{\ell_i} g_{\ell_i} x - \sum_{i=1}^{L_u} \hat{h}_{\ell_i}\hat{g}_{\ell_i}\hat{x}\right)\right\|^2\right)$$
$$= \Pr\left(\frac{\sqrt{P}}{2}\left|\sum_{i=1}^{L_u} h_{\ell_i} g_{\ell_i} x - \sum_{i=1}^{L_u} \hat{h}_{\ell_i}\hat{g}_{\ell_i}\hat{x}\right|^2 < B\right), \tag{B.24}$$

where

$$B = -\Re\left\{n\left(\sum_{i=1}^{L_u} h_{\ell_i} g_{\ell_i} x - \sum_{i=1}^{L_u} \hat{h}_{\ell_i}\hat{g}_{\ell_i}\hat{x}\right)\right\} - \Im\left\{n\left(\sum_{i=1}^{L_u} h_{\ell_i} g_{\ell_i} x - \sum_{i=1}^{L_u} \hat{h}_{\ell_i}\hat{g}_{\ell_i}\hat{x}\right)\right\}, \tag{B.25}$$

so

$$\sigma_B^2 = \Re\left\{\sigma_n^2\left(\left|\sum_{i=1}^{L_u} h_{\ell_i} g_{\ell_i} x - \sum_{i=1}^{L_u} \hat{h}_{\ell_i}\hat{g}_{\ell_i}\hat{x}\right|^2\right)\right\} + \Im\left\{\sigma_n^2\left(\left|\sum_{i=1}^{L_u} h_{\ell_i} g_{\ell_i} x - \sum_{i=1}^{L_u} \hat{h}_{\ell_i}\hat{g}_{\ell_i}\hat{x}\right|^2\right)\right\}, \tag{B.26}$$

where $\Re\{n\}$ and $\Im\{n\}$, represent the real and imaginary parts of the AWGN n, respectively with $\Re\{n\}, \Im\{n\} \sim N(0, \frac{1}{2})$. Thus (B.24) becomes

$$\Pr(x_\ell \to \hat{x}_{\hat{\ell}}|F_\ell)$$
$$= Q\left(\frac{\sqrt{P}\|\sum_{i=1}^{L_u} h_{\ell_i} g_{\ell_i} x - \sum_{i=1}^{L_u} \hat{h}_{\ell_i}\hat{g}_{\ell_i}\hat{x}\|^2}{2\sqrt{\frac{1}{2}\|\sum_{i=1}^{L_u} h_{\ell_i} g_{\ell_i} x - \sum_{i=1}^{L_u} \hat{h}_{\ell_i}\hat{g}_{\ell_i}\hat{x}\|^2}}\right)$$
$$= Q\left(\sqrt{\frac{P\|\sum_{i=1}^{L_u} h_{\ell_i} g_{\ell_i} x - \sum_{i=1}^{L_u} \hat{h}_{\ell_i}\hat{g}_{\ell_i}\hat{x}\|^2}{2}}\right)$$
$$= Q\left(\sqrt{\hat{\gamma}\|[\|]\sum_{i=1}^{L_u} h_{\ell_i} g_{\ell_i} x - \sum_{i=1}^{L_u} \hat{h}_{\ell_i}\hat{g}_{\ell_i}\hat{x}}^2\right) = Q\left(\sqrt{\gamma_n}\right), \tag{B.27}$$

where $\hat{\gamma} = \frac{P}{2}$. In order to further proceed with the derivation of (5.18), we calculate the expected value of (B.27), by integrating it for all the possible values of F_ℓ, resulting in

$$\Pr(x_\ell \to \hat{x}_{\hat{\ell}}|q) = \mathbb{E}[\Pr(x_\ell \to \hat{x}_{\hat{\ell}}|F_\ell)] \leq \int_0^\infty Q\left(\sqrt{\gamma_n}\right) f(\gamma_n) d\gamma_n, \tag{B.28}$$

where $f(\gamma_n)$ is the pdf of γ_n given by (5.19), as a function of q, which is a non-negative integer. The inequality in (B.28) results from the following assumption. Depending on the estimated pair symbol $(x_\ell \to \hat{x}_{\hat{\ell}})$, γ_n may result as a sum of either correlated or independent channels. For mathematical tractability and specifically for the case

of the correlated channels, we consider an upper bound with good results as proved in [52], assuming that all the terms consisting of γ_n are independent. Taking into consideration that $x \in \mathbb{C}$, the real and imaginary parts of the terms consisting the norm of γ_n are rounded to the nearest integer. In addition, it has to be noted that due to the scaling property of a normal distribution, imaginary terms of γ_q, i.e. $-jh_{\ell_i}g_{\ell_i}$, may be treated as $h_{\ell_i}g_{\ell_i}$, while negative terms i.e. $-h_{\ell_i}g_{\ell_i}$ may be treated as $h_{\ell_i}g_{\ell_i}$.

Hence the expression of Proposition 4 is derived.

B.7 Proof of Proposition 5

In our study of GSMA technique, the number of active antennas is $L_u = 2$ and we apply Alamouti OSTBC. The PEP for a given $\mathbf{F}_\ell$, is given with the use of [183, Eq.(21)] as

$$\Pr(\mathbf{X} \to \hat{\mathbf{X}}|\mathbf{F}_\ell) = Q\left(\sqrt{\frac{P}{2}\left\|\mathbf{F}_\ell(\mathbf{X}-\hat{\mathbf{X}})\right\|^2}\right). \tag{B.29}$$

Following the analysis in [227, Ch.7], we define a new matrix $\mathbf{A} = (\mathbf{X}-\hat{\mathbf{X}})(\mathbf{X}-\hat{\mathbf{X}})^H$. Because $\mathbf{A}$ is Hermitian, we can apply an eigenvalue decomposition and rewrite it, as $\mathbf{A} = \mathbf{U}\Lambda\mathbf{U}^H$, where $\mathbf{U}$ is a unitary matrix and Λ is a diagonal matrix with diagonal elements equal to the eigenvalues of the matrix $\mathbf{A}$. With the proper substitutions and calculations, we have

$$\left\|\mathbf{F}_\ell(\mathbf{X}-\hat{\mathbf{X}})\right\|^2 = \mathbf{F}_\ell\mathbf{U}\Lambda\mathbf{U}^H\mathbf{F}_\ell^H = \sum_{i=1}^{L_u}\lambda_i\left\|\beta_i\right\|^2, \tag{B.30}$$

where λ_i's are the eigenvalues of the matrix $\mathbf{A}$, calculated from $\|\mathbf{A}-\lambda\mathbf{I}\|^2 = 0$. In addition, β_i are the beta terms, which are functions of the DBC matrix and from (a) in (B.36), are given as $\beta_i = \sum_{j=1}^{L_u} u_{ji}h_{\ell_j}g_{\ell_j}$, with $i \in (1, L_u)$. Without loss of generality, we assume that the codewords are chosen as

$$\mathbf{X} = \begin{pmatrix}\mathbf{x}_1 & \mathbf{x}_2 & \mathbf{0}_{2\times(L-2)}\end{pmatrix}, \tag{B.31}$$

and

$$\hat{\mathbf{X}} = \begin{pmatrix}\hat{\mathbf{x}}_1 & \mathbf{0} & \hat{\mathbf{x}}_2 & \mathbf{0}_{2\times(L-3)}\end{pmatrix}\exp(j\theta), \tag{B.32}$$

where $j = \sqrt{-1}$ is the imaginary number and with $\mathbf{0}_{i\times j}$ we denote a small zero of i lines and j columns.

Then the matrix $\mathbf{A}$ is given as

$$\mathbf{A} = \begin{pmatrix} x_1 - \hat{x_1}\exp(j\theta) & x_2 & -\hat{x_2}\exp(j\theta) & \mathbf{0}_{1\times(L-3)} \\ -x_2^* + \hat{x_2}^*\exp(j\theta) & x_1^* & -\hat{x_1}^*\exp(j\theta) & \mathbf{0}_{1\times(L-3)} \end{pmatrix}$$

$$\times \begin{pmatrix} x_1^* - \hat{x}_1^* \exp(-j\theta) & -x_2 + \hat{x}_2 \exp(-j\theta) \\ x_2^* & x_1 \\ -\hat{x}_2^* \exp(-j\theta) & -\hat{x}_1 \exp(-j\theta) \\ \mathbf{0}_{(L-3)\times 1} & \mathbf{0}_{(L-3)\times 1} \end{pmatrix} \tag{B.33}$$

$$= \begin{pmatrix} k - \frac{x_1 \hat{x}_1^*}{\exp(j\theta)} - x_1^* \hat{x}_1 \exp(j\theta) & \frac{x_1 \hat{x}_2}{\exp(j\theta)} + x_2 \hat{x}_1 \exp(j\theta) \\ \frac{\hat{x}_1^* x_2^*}{\exp(j\theta)} + x_1^* \hat{x}_2^* \exp(j\theta) & k - \frac{x_2^* \hat{x}_2}{\exp(j\theta)} - x_2 \hat{x}_2^* \exp(j\theta) \end{pmatrix}, \tag{B.34}$$

where $k = \sum_{i=1}^{2} \left(\|x_i\|^2 + \|\hat{x}_i\|^2 \right)$. Calculating, the eigenvalues λ_1 and λ_2, based on the estimated $\hat{x}_1, \hat{x}_2$ and the angle θ, we can proceed by solving the following system

$$\mathbf{A} \begin{bmatrix} u_{11} \\ u_{21} \end{bmatrix} = \lambda_1 \begin{bmatrix} u_{11} \\ u_{21} \end{bmatrix},$$

$$\mathbf{A} \begin{bmatrix} u_{12} \\ u_{22} \end{bmatrix} = \lambda_2 \begin{bmatrix} u_{12} \\ u_{22} \end{bmatrix}, \tag{B.35}$$

which results in calculating the elements $u_{ji} \in \mathbb{C}$ of the unitary matrix $\mathbf{U}$. With the use of existing numerical tools such as $eig(\cdot)$ function in Matlab [146], we can calculate reliably and efficiently the eigenvalues λ_i's of the matrix $\mathbf{A}$ and the u_{ji} terms of the unitary matrix $\mathbf{U}$. Therefore, (B.29) becomes

$$\Pr(\mathbf{X} \to \hat{\mathbf{X}} \mid \mathbf{F}_\ell)$$

$$\overset{(a)}{=} Q\left(\sqrt{\frac{P}{2} \sum_{i=1}^{L_u} \lambda_i \left\| \sum_{j=1}^{L_u} u_{ji} h_{\ell_j} g_{\ell_j} \right\|^2} \right)$$

$$= Q\left(\sqrt{\frac{P}{2}} \left(\lambda_1 \|u_{11} h_{\ell_1} g_{\ell_1} + u_{21} h_{\ell_2} g_{\ell_2}\|^2 + \lambda_2 \|u_{12} h_{\ell_1} g_{\ell_1} + u_{22} h_{\ell_2} g_{\ell_2}\|^2 \right)^{\frac{1}{2}} \right)$$

$$= Q\left(\sqrt{\frac{P}{2}} \left(\lambda_1 \|u_{11}\|^2 \|h_{\ell_1} g_{\ell_1} + a_3 h_{\ell_2} g_{\ell_2}\|^2 + \lambda_2 \|u_{22}\|^2 \|a_4 h_{\ell_1} g_{\ell_1} + h_{\ell_2} g_{\ell_2}\|^2 \right)^{\frac{1}{2}} \right)$$

$$= Q(\sqrt{\gamma_1 + \gamma_2}), \tag{B.36}$$

where $a_3 = \frac{u_{21}}{u_{11}}$, $a_4 = \frac{u_{12}}{u_{22}}$, $\hat{\gamma_1} = \frac{P}{2} \lambda_1 \|u_{11}\|^2$ and $\hat{\gamma_2} = \frac{P}{2} \lambda_2 \|u_{22}\|^2$.

In order to proceed further with the derivation of PEP in GSMA, given by (5.22), we calculate the expected value of (B.36), for all possible values of $\mathbf{F}_\ell$, as follows

$$\Pr(\mathbf{X} \to \hat{\mathbf{X}}|q) = \mathbb{E}[\Pr(\mathbf{X} \to \hat{\mathbf{X}} \mid \mathbf{F}_\ell)] \leq \int_0^\infty \int_0^\infty Q(\sqrt{\gamma_1 + \gamma_2}) f_{\gamma_1}(\gamma_1) f_{\gamma_2}(\gamma_2) d\gamma_1 d\gamma_2, \tag{B.37}$$

where with $f_{\gamma_1}(\gamma_1)$ and $f_{\gamma_2}(\gamma_2)$, we denote the pdf of the DBC in the first and the second time instant respectively, while applying the Alamouti code, given by (5.19). The inequality in (B.37) results from the assumption taken into consideration in Proposition 1, i.e. for mathematical tractability, all the terms of the DBC consisting of γ_1 and γ_2 are considered as independent.

Hence the expression of Proposition 5 is derived.

B.8 Proof of Proposition 6

Taking into consideration the following improved exponential approximation for the Q-function [228]

$$Q(x) \approx \frac{1}{12} \exp\left(-\frac{x^2}{2}\right) + \frac{1}{4} \exp\left(-\frac{2}{3}x^2\right), \; x > 0 \tag{B.38}$$

as well as the approximations of the Bessel function [229], we obtain the following approximation regarding the pdf from (5.19), for high SNR i.e. $P \to \infty$, as

$$f_{\gamma_n}(\gamma_n) = \begin{cases} -\frac{1}{\hat{\gamma}} \ln\left(\frac{\gamma_n}{\hat{\gamma}}\right), & \text{if } q = 1, \\ \frac{1}{(q-1)\hat{\gamma}}, & \text{if } q > 1, \end{cases} \tag{B.39}$$

where we recall here that q is the total number of independent terms that consist of DBC γ_n, and $\hat{\gamma}$ is the average power at the RN. With the proper substitutions and calculations, the probability of error for GSM (5.20), in terms of SER, results in

- for $q = 1$

$$\mathrm{P}_s^{\mathrm{GSM}} \leq -\frac{N_1}{2P} \int_0^\infty \left(\frac{1}{3} \exp\left(-\frac{\gamma_n}{2}\right) + \exp\left(-\frac{2\gamma_n}{3}\right)\right) \times \ln \frac{2\gamma_n}{P} d\gamma_n = \frac{a + b \ln P^{-1}}{P}, \tag{B.40}$$

where a, b are numerical values resulting from the calculation of the integral. With the proper calculations the diversity order follows as

$$d_{\mathrm{GSM}} = \lim_{P \to \infty} -\frac{\log \mathrm{P}_s^{\mathrm{GSM}}}{\log P} = \lim_{P \to \infty} \left(- \frac{\log\left(a + b \ln P^{-1}\right)}{\log P} + \frac{\log P}{\log P} \right) = 1. \tag{B.41}$$

- for $q > 1$

$$\mathrm{P}_s^{\mathrm{GSM}} \leq \frac{N_1}{2(q-1)P} \times \int_0^{\infty} \left(\frac{1}{3} \exp\left(-\frac{\gamma_n}{2}\right) + \exp\left(-\frac{2\gamma_n}{3}\right) \right) d\gamma_n = a_1 P^{-1}, \tag{B.42}$$

where a_1 is a numerical value resulting from the calculation of the integral. With the proper substitutions and calculations the diversity order follows as

$$d_{\mathrm{GSM}} = \lim_{P\to\infty} -\frac{\log \mathrm{P}_s^{\mathrm{GSM}}}{\log P} = \lim_{P\to\infty} \left(-\frac{\log a_1}{\log P} + \frac{\log P}{\log P} \right) = 1. \tag{B.43}$$

For the simplified case of SM technique, the result of diversity order is identical to GSM and equal to one. Specifically for the case of GSMA technique, the same methodology as in GSM is followed. With the proper substitutions and calculations, the probability of error for GSMA (5.23), in terms of SER, results in

- $q = 1$, both for γ_1 and γ_2

$$\mathrm{P}_s^{\mathrm{GSMA}} \leq \frac{(a_1 + b_1 \ln P^{-1})(a_2 + b_2 \ln P^{-1})}{P^2}, \tag{B.44}$$

- $q = 1$, for γ_1 and $q > 1$, for γ_2 and vice versa

$$\mathrm{P}_s^{\mathrm{GSMA}} \leq \frac{(a_1 + b_1 \ln P^{-1}) a_3}{P^2}, \tag{B.45}$$

- $q > 1$,both for γ_1 and γ_2

$$\mathrm{P}_s^{\mathrm{GSMA}} \leq \frac{a_4}{P^2} \tag{B.46}$$

where $a_1, a_2, a_3, a_4, b_1, b_2$ are numerical values resulting from the calculation of the integrals, in each case. With the proper substitutions and calculations the diversity order results in

$$d_{\mathrm{GSMA}} = \lim_{P\to\infty} -\frac{\log \mathrm{P}_s^{\mathrm{GSMA}}}{\log P} = 2. \tag{B.47}$$

Hence the expression of Proposition 6 is derived.

B.9 Proof of Lemma 1

By substituting (6.15) and (6.16) into (6.17), we have

$$i_{\mathrm{DC}_{21}} + i_{\mathrm{DC}_{22}} + \cdots + i_{\mathrm{DC}_{2K}} \underset{\tilde{x}=0}{\overset{\tilde{x}=1}{\gtrless}} \frac{K}{(\lambda_1 - \lambda_0)} \ln\left(\frac{\lambda_1}{\lambda_0}\right), \tag{B.48}$$

where we set the right part of inequality equal to t and the left part $u = \sum_{j=1}^{j=K} i_{\mathrm{DC}_{2j}}$. Taking into consideration that $i_{\mathrm{DC}_{2j}}$ follows the exponential distribution from (6.15), then by considering [226, Ch.1.8.7], we conclude that u follows the Erlang distribution, which results in

$$f(u) = \frac{u^{K-1} e^{-\lambda_x u} \lambda_x^K}{\Gamma(K)}. \tag{B.49}$$

Following our analysis, the total probability of error is calculated as

$$P_{\mathrm{D}} = \mathbb{P}(u < t | x = 1) + \mathbb{P}(u > t | x = 0) = \frac{1}{2}\left(\int_0^t f(u|x=1)du + \int_t^\infty f(u|x=0)du \right). \tag{B.50}$$

By substituting (B.49) and the appropriate calculations with the use of (6.16), (6.18) is derived.

B.10 Proof of Proposition 7

For the integrated receiver, a portion $\rho \in (0, 1)$ of the DC power signal is channeled to the decoder for ID. Following the same analysis as for the proposed diplexer-based SWIPT system model, it is shown that this power signal is the same as the DC output of the diplexer, i.e. $i_{\mathrm{DC}_{1j}}$. As such, it is exponentially distributed, with rate parameter equal to

$$\lambda_x' = 1/\mathbb{E}(\rho i_{\mathrm{DC}_{1j}}) = \frac{1}{\rho(Px^2 + 1)} = \frac{\lambda_x}{\rho}, \tag{B.51}$$

and the pdf is expressed as

$$f(\rho i_{\mathrm{DC}_{1j}}) = \frac{\lambda_x}{\rho} e^{-\frac{\lambda_x}{\rho} i_{\mathrm{DC}_{1j}}}. \tag{B.52}$$

Substituting (B.52) in (6.17), and the appropriate calculations with the use of (B.51), the ML criterion for the decision of the transmitted symbol follows

$$i_{\mathrm{DC}_{11}} + i_{\mathrm{DC}_{12}} + \cdots + i_{\mathrm{DC}_{1K}} \underset{\tilde{x}=0}{\overset{\tilde{x}=1}{\gtrless}} \frac{\rho K}{(\lambda_1 - \lambda_0)} \ln\left(\frac{\lambda_1}{\lambda_0}\right), \tag{B.53}$$

where the right part of (B.53) is equal to $t' = \rho t$. We note also that the left part is equal to $u = \sum_{j=1}^{j=K} i_{\mathrm{DC}_{1j}}$ as defined in Appendix B.9, with pdf given from (B.49).

Therefore the total probability of error is given by

$$P_{\mathrm{I}} = \mathbb{P}(u < t' | x = 1) + \mathbb{P}(u > t' | x = 0) = \frac{1}{2}\left(\int_0^{t'} f(u|x=1)du + \int_{t'}^\infty f(u|x=0)du \right), \tag{B.54}$$

where by substituting $t' = \rho t$, (6.21) is derived.

Bibliography

[1] Cisco, "White Paper: Cisco annual internet report (2018-2023)," upd. March 9, 2020. [Online]. Available: https://www.cisco.com/c/en/us/solutions/collateral/executive-perspectives/annual-internet-report/white-paper-c11-741490.html

[2] GSMA, "Internet of things In the 5G era," November 2019. [Online]. Available: https://www.gsma.com/iot/wp-content/uploads/2019/11/201911-GSMA-IoT-Report-IoT-in-the-5G-Era.pdf

[3] Y. Yuan, Z. Yuan, and L. Tian, "5G non-orthogonal multiple access study in 3GPP," *IEEE Commun. Magaz.*, vol.58, no. 7, pp. 90-96, July 2020.

[4] S. K. Agrawal, and K. Sharma, "5G millimeter wave (mmWave) communications," *Intern. Conf. on Comp. for Sustain. Global Develop. (INDIACom)*, New Delhi, India, October 2016.

[5] Q.V. Pham, F. Fang, V. N. Ha, Md. J. Piran, M. Le, L. B. Le, W. J. Hwang, Z. Ding, "A Survey of Multi-Access Edge Computing in 5G and Beyond: Fundamentals, Technology Integration, and State-of-the-Art," *IEEE Access*, vol. 8, pp. 116974-117017, June 2020.

[6] Y. Wang, P. Luo, X. Zeng, D. Peng, Z. Li and B. Zhang, "A neural network assistance AMPPT solar energy harvesting system with 89.39% efficiency and 0.01–0.5% tracking errors," *IEEE Trans. Circuits Syst. I Reg. Papers*, vol. 67, no. 9, pp. 2960-2971, 2020.

[7] S. H. Cheong, M. Kang, Y. Kim, M. Park, J. Park and D. K. Noh, "Solar-CTP: An enhanced CTP for solar-powered wireless sensor networks," *IEEE Access*, vol. 8, pp. 127142-127155, 2020.

[8] J. D. Hughes, C. Occhiuzzi, J. Batchelor, and G. Marrocco, "Folded Comb-line Array for Healthcare 5G-RFID-based IoT applications," *IEEE Int. Conf. on RFID (RFID)*, Atlanta, USA, July 2021.

[9] Y. Shi, Y. Fan, Y. Li, L. Yang and M. Wang, "An efficient broadband slotted rectenna for wireless power transfer at LTE band," *IEEE Trans. Antennas Propag.*, vol. 67, no. 2, pp. 814-822, February 2019.

[10] N. Shinohara, "Wireless power transfer in Japan: Regulations and activities," *Proc. 14th Eur. Conf. Antennas Propag. (EuCAP)*, pp. 1-4, Copenhagen, Denmark, March 2020.

[11] L. R. Varshney, "Transporting information and energy simultaneously," *in Proc. IEEE Int. Symp. Inf. Theory*, pp. 1612-1616, Toronto, Canada, July 2008.

[12] R. Zhang and C. K. Ho, "MIMO broadcasting for simultaneous wireless information and power transfer," *IEEE Trans. Wireless Commun.*, vol. 12, no. 5, pp. 1989-2001, May 2013.

[13] P. Grover and A. Sahai, "Shannon meets Tesla: Wireless information and power transfer," *in Proc. IEEE Int. Symp. Inf. Theory*, vol.8, pp. 2363-2367, Austin, TX, USA, June 2010.

[14] H. Ju and R. Zhang, "Throughput maximization in wireless powered communication networks," *IEEE Glob. Comm.Conf. (GLOBECOM)*, Atlanta, GA, USA, June 2014.

[15] K. Han and K. Huang, "Wirelessly powered backscatter communication networks: Modeling coverage and capacity," *IEEE Trans. Wireless Commun.*, vol. 16, no.4, pp. 2548-2561, April 2017.

[16] C. Boyer and S. Roy, "Backscatter communication and RFID: Coding energy and MIMO analysis," *IEEE Trans. Commun.*, vol. 62, no. 3, pp. 770-785, March 2014.

[17] T. D. Ponnimbaduge Perera, D. N. K. Jayakody, S. K. Sharma, S. Chatzinotas, and J. Li, "Simultaneous wireless information and power transfer (SWIPT): Recent advances and future challenges," *IEEE Comm.. Surv. Tut.*, vol. 20, no. 1, pp. 264-302, 2018.

[18] I. Krikidis, S. Timotheou, S. Nikolaou, G. Zheng, D. W. K. Ng, and R. Schober, "Simultaneous wireless information and power transfer in modern communication systems," *IEEE Commun. Mag.*, vol. 52, no. 11, pp. 104–110, November 2014.

[19] B. Smida, and P. Pahlavan, "Unified wireless power and information transfer using a diplexed rectifier," *IEEE Glob. Commun. Conf. (GLOBE- COM)*, Madrid, Spain, December 2021.

[20] X. Zhou, R. Zhang, and C. K. Ho, "Wireless information and power transfer: Architecture design and rate-energy tradeoff," *IEEE Trans. Commun.*, vol. 61, no. 11, pp. 4757-4767, November 2013.

[21] N. V. Huynh, D. T. Hoang, X. Lu, D. Niyato, P. Wang, D. I. Kim, "Ambient backscatter communications: A contemporary survey," *IEEE Commun. Surveys Tut.*, vol. 20, no. 4, pp. 2889–2922, May 2018.

[22] Y. Alsaba, S. K. A. Rahim, and C. Y. Leow, "Beamforming in wireless energy harvesting communications systems: A survey," *IEEE Commun. Surveys Tuts.*, vol. 20, no. 2, pp. 1329-1360, May 2018.

[23] K.V.S. Rao, P.V. Nikitin and S.F. Lam, "Antenna design for UHF RFID tags: a review and a practical application," *in IEEE Trans. Antenna Propag.*, vol.53, no. 12, pp. 3870–3876, December 2005.

[24] S. H. Choi and D. I. Kim, "Backscatter radio communication for wireless powered communication networks," *in Proc. 21st Asia–Pac. Conf.Commun. (APCC)*, Kyoto, Japan, October 2015.

[25] X. Lu et al., "Ambient backscatter assisted wireless powered communications," *IEEE Wireless Commun.*, vol. 25, no. 2, pp. 170–177, April 2018.

[26] Z. Niu, W. Ma, W. Wang, and T. Jiang,"Spatial modulation-based ambient backscatter: Bringing energy self-sustainability to massive internet of everything in 6G," in *China Comm.*, vol.17, no. 12, pp. 52-65, December 2020.

[27] C. Xu, L. Yang, and P. Zhang, "Practical backscatter communication systems for battery-free internet of things: A tutorial and survey of recent research," *IEEE Signal Processing Magazine*, vol. 35, no.5, pp. 16–27, September 2018.

[28] R. Zhang and C.K. Ho, "MIMO broadcasting for simultaneous wireless information and power transfer," *IEEE Trans. Wireless Commun.*, vol.12, no. 5, pp. 1989-2001, May 2013.

[29] L. Liu, R. Zhang, and K.C. Chua, "Wireless information transfer with opportunistic energy harvesting," *IEEE Trans. Wireless Commun.*, vol.12, no. 1, pp. 288-300, January 2013.

[30] P. Liu, S. Gazor, Il-M. Kim, and D.I. Kim, "Noncoherent relaying in energy harvesting communication systems," *IEEE Trans. Wir. Commun.*, vol. 14, no. 12, pp. 6940-6954, December 2015.

[31] Y. Zeng, B. Clerckx, and R. Zhang, "Communications and Signals Design for Wireless Power Transmission," *IEEE Trans. Commun.*, vol. 65, no. 5, pp. 2264-2290, May 2017.

[32] D.J. Love, R.W. Heath Jr, V.K.N. Lau, D. Gesbert, B.D. Rao, and M. Andrews, "An overview of limited feedback in wireless communication systems," *IEEE J. Selected Areas Commun.*, vol. 26, no. 8, pp. 1341-1365, October 2008.

[33] J. Xu and R. Zhang, "Energy beamforming with one-bit feedback," *IEEE Trans. Signal Process.*, vol.62, no. 20, pp. 5370-5381, October 2014.

[34] J. Xu and R. Zhang, "A general design framework for MIMO wireless energy transfer with limited feedback," *IEEE Trans. Sign. Process*, vol.64, no. 10, pp. 2475-2488, May 2016.

[35] S. Lee and R. Zhang, "Distributed wireless power transfer with energy feedback," *IEEE Trans. Signal Process.*, vol.65, no. 7, pp. 1685–1699, April 2017.

[36] Y. Zeng and R. Zhang, "Optimized training design for wireless energy transfer," *IEEE Trans. Commun.*, vol.63, no. 2, pp. 536-550, February 2015.

[37] Y. Zeng and R. Zhang, "Optimized training for net energy maximization in multi-antenna wireless energy transfer over frequency-selective channel," *IEEE Trans. Commun.*, vol.63, no. 6, pp. 2360-2373, April 2015.

[38] W. S. Lee, C. H. Kang, Y. K. Moon, and H. K. Song, "Determination scheme for detection thresholds using multiple antennas in Wi-Fi backscatter systems," *IEEE Access*, vol. 5, pp. 22159–22165, October 2017.

[39] R. Zhang, L. Yang, and L. Hanzo, "Energy pattern aided simultaneous wireless information and power transfer," *IEEE J. Select. Areas Commun.*, vol. 33, no. 8, pp. 1492–1504, August 2015.

[40] W. Liu, X. Zhou, S. Durrani and P. Popovski, "SWIPT with practical modulation and RF energy harvesting sensitivity,"*IEEE Intern. Conf. on Com.*, Kuala Lumpur, Malaysia, May 2016.

[41] W. Liu, X. Zhou, S. Durrani and P. Popovski, "A novel receiver design with joint coherent and non-coherent processing," *IEEE Trans. on Commun.*, vol. 65, no. 8, pp. 3479–3493, April 2017.

[42] P.Alevizos, A.Bletsas, and G.N.Karystinos, "Noncoherent short-packet detection and decoding for scatter radio sensor networking," *IEEE Trans. Commun.*, vol. 65, no. 5, pp. 2128-2140, May 2017.

[43] D.-T. Phan-Huy, Y. Kokar, K. Rachedi, P. Pajusco, A. Mokh, T. Magounaki, R. Masood, C. Buey, P. Ratajczak, N. Malhouroux-Gaffet, J.-M. Conrat, J.- C. Prevotet, A. Ourir, J. de Rosny, M. Crussiere, M. Herard, A. Gati, T. Sarrebourse, M. Di Renzo, "Single-carrier spatial modulation for the Internet of Things: Design and performance evaluation by using real compact and reconfigurable antennas," *IEEE Access*, vol. 7, pp. 18978-18993, January 2019.

[44] Y. Wu, Q. Yang, and K. S. Kwak, "Energy efficiency maximization for energy harvesting millimeter wave systems at high SNR," *IEEE Wirel. Commun. Lett.*, vol. 6, no. 5, pp. 698-701, October 2017.

[45] S. Shen, Y. Zhang, C. Chiu, and R. Murch, "A triple-band high-gain multibeam ambient RF energy harvesting system utilizing hybrid combining," *IEEE Trans. Ind. Electron.*, vol. 67, no. 11, pp. 9215-9226, November 2020.

[46] L. Zheng, and D.N.C. Tse, "Diversity and multiplexing: a fundamental tradeoff in multiple-antenna channels," *IEEE Trans. Inf. Theory*, vol. 49, no. 5, pp. 1073-1096, May 2003.

[47] I. E. Telatar, "Capacity of multi-antenna gaussian channels," *Europ. Trans. Telecommu.*, USA, Lucent Techn. Bell Labor., vol. 10, pp. 585-595, 1999.

[48] G. Foschini, G. Golden, R. Valenzuela, and P. Wolniansky, "Simplified processing for high spectal efficiency wireless communication employing multi-element arrays," *IEEE J. Select. Areas Commun.*, vol. 17, no. 11, pp. 1841-1852, November 1999.

[49] N. Garg, J. Zhang, and T. Ratnarajahe, "Rate-energy balanced precoding design for SWIPT based two-way relay systems," *IEEE J. Select. Top. in Sign. Proc.*, vol. 15, no. 5, pp. 1228-1241, August 2021.

[50] H. Lee, K. J. Lee, H. Kim, and I. Lee, "Multi-antenna SWIPT systems with joint time switching," *IEEE Int. Conf. Comm.*, Kansas, USA, 2018.

[51] S. Wang, L. Ma, and W. Wu, "Joint TS beamforming and hybrid TS-PS receiving design for SWIPT systems," *IEEE Access*, vol. 9, pp. 50686-50699, 2021.

[52] J. Griffin and G. Durgin, "Gains for RF tags using multiple antennas," *IEEE Trans. Antennas Propag.*, vol. 56, no. 2, pp. 563–570, February 2008.

[53] C. He, H. Luan, X. Li, C. Ma, L. Han, and Z. J. Wang, "A simple, high-performance space-time code for MIMO backscatter communications," *IEEE Intern. of Th. Journ.*, vol. 7, no. 4, pp. 3586-3591, April 2020.

[54] C. Hen, X. Chen, Z.J. Wang and W. Su, "On the performance of MIMO RFID backscattering channels," *EURASIP J. Wirel. Commun. Net.*, pp. 1—15, November 2012.

[55] M. G. Livadaru, and J. L. Volakis, "Fabrication and measurements of a low-cost, dual-polarized advanced planar array with wide scanning coverage," *IEEE Inter. Sympos. on Anten. and Prop. and USNV/URSI Nation. Radio Scien. Meet.*, San Diego, CA, USA, October 2017.

[56] M. B. Akbar, M. M. Morys, C. R. Valenta, and G. D. Durgin, "Range improvement of backscatter radio systems at 5.8 GHz using tags with multiple antennas," *Proc. of the 2012 IEEE Intern. Symp. on Ant. and Prop.*, Chicago, IL, USA, July 2012.

[57] C. He, H. Luan, X. Li, C. Ma, L. Han and Z. Jane Wang, "A simple high-performance space–time code for MIMO backscatter communications," *IEEE Internet Things J.*, vol. 7, no. 4, pp. 3586-3591, April 2020.

[58] F. Shaikh and S. Zeadally, "Energy harvesting in wireless sensor networks: A comprehensive review," *Renew. Sustain. Energy Rev.*, vol. 55, pp. 1041-1054, 2016.

[59] I.-J. Yoon, "Wireless power transfer in the radiating near-field region," *in Proc. USNC URSI Radio Sci. Meeting (Joint AP S Symp.)*, p. 344, Vancouver, BC, Canada, 2015.

[60] R. E. Hamam, A. Karalis, J. D. Joannopoulos, and M. Soljacic, "Efficient weakly-radiative wireless energy transfer: An EIT-like approach," *Ann. Phys.*, vol. 324, pp. 1783–1795, 2009.

[61] J. G. Hayes, M. G. Egan, J. M. D. Murphy, S. E. Schulz, and J. T. Hall, "Wide-load-range resonant converter supplying the SAE J-1773 electric vehicle inductive charging interface," *IEEE Trans. Ind. Appl.*, vol. 35, no.4, pp. 884-895, August 1999.

[62] A. P. Sample, D. T. Meyer, and J. R. Smith, "Analysis, experimental results, and range adaptation of magnetically coupled resonators for wireless power transfer," *IEEE Trans. Ind. Electron.*, vol. 58, no. 2, pp. 544–554, February 2011.

[63] W. Brown, J. Mims and N. Heenan, "An experimental microwave-powered helicopter," *Proc. IRE Int. Conv. Rec.*, New York, NY, USA, March 1966.

[64] R. M. Dickinson, "Performance of a high-power 2.388-GHz receiving array in wireless power transmission over 1.54 km," *IEEE MTT-S Int. Microw. Symp. Dig.*, Cherry Hill, NJ, USA, June 1976.

[65] S. Kim et al., "Ambient RF energy-harvesting technologies for self-sustainable standalone wireless sensor platforms", *Proc. IEEE, vol. 102*, vol. 102, no. 11, pp. 1649-1666, November 2014.

[66] M. Pinuela, P. D. Mitcheson and S. Lucyszyn, "Ambient RF energy harvesting in urban and semi-urban environments," *IEEE Trans. Microw. Theory Techn.*, vol. 61, no. 7, pp. 2715-2726, July 2013.

[67] D. Mishra et al., "Smart RF energy harvesting communications: Challenges and opportunities," *IEEE Commun. Mag.*, vol. 53, no. 4, pp. 70-78, April 2015.

[68] A. Costanzo and D. Masotti, "Energizing 5G: Near- and far-field wireless energy and data transfer as an enabling technology for the 5G IoT," *IEEE Microw. Mag.*, vol. 18, no. 3, pp. 125-136, May 2017.

[69] X. Gu, S. Hemour and K. Wu,"Far-field wireless power harvesting: Nonlinear modeling, rectenna design, and emerging applications," *Proc. of the IEEE* , vol.110, no.1, pp. 56-73, January 2022.

[70] H. S. Vu, N. Nguyen, N. Ha-Van, C. Seo and M. T. Le, "Multiband ambient RF energy harvesting for autonomous IoT devices," *IEEE Microw. Wireless Compon. Lett.*, vol. 30, no. 12, pp. 1189-1192, December 2020.

[71] V. Surducan, E. Surducan and R. Gutt, "Harvesting and conversion of the environmental electromagnetic pollution into electrical energy by novel rectenna array coupled with resonant micro-converter," *Energy*, vol. 211, November 2020, doi: https://doi.org/10.1016/j.energy.2020.118645.

[72] M. Wagih, A. S. Weddell and S. Beeby, "Rectennas for radio-frequency energy harvesting and wireless power transfer: A review of antenna design [antenna applications corner]," *IEEE Antennas Propag. Mag.*, vol. 62, no. 5, pp. 95-107, October 2020.

[73] J. Cho and W. Jung, "RectBoost: Start-up boosting for rectenna using an adaptive matching network," *Proc. IEEE Int. Symp. Circuits Syst. (ISCAS)*, Daegu, Korea, May 2021.

[74] P. Lu, C. Song and K. M. Huang, "Ultra-wideband rectenna using complementary resonant structure for microwave power transmission and energy harvesting," *IEEE Trans. Microw. Theory Techn.*, vol. 69, no. 7, pp. 3452-3462, July 2021.

[75] L. Guo, X. Gu, P. Chu, S. Hemour and K. Wu, "Collaboratively harvesting ambient radiofrequency and thermal energy", *IEEE Trans. Ind. Electron.*, vol. 67, no. 5, pp. 3736-3746, May 2020.

[76] A. Z. Ashoor and O. M. Ramahi, "Polarization-independent cross-dipole energy harvesting surface", *IEEE Trans. Microw. Theory Techn.*, vol. 67, no. 3, pp. 1130-1137, March 2019.

[77] C. Valenta and G. Durgin, "Harvesting Wireless Power: Survey of energy - harvester conversion efficiency in far-field, wireless power transfer systems," *IEEE Microw. Mag.*, vol. 15, no. 4, pp. 108-120, June 2014.

[78] M. T. Penella-Lopez and M. Gasulla-Forner, "Radiofrequency energy harvesting," in *in Powering Autonomous Sensors*, New York: Springer, 2011, ch. 6, pp. 125-147.

[79] Y. Zhang, S. Shen, C. Y. Chiu and R. Murch, "Hybrid RF-solar energy harvesting systems utilizing transparent multiport micromeshed antennas," *IEEE Trans. Microw. Theory Techn.*, vol. 67, no. 11, pp. 4534-4546, November 2019.

[80] A. Bakytbekov, Z. Iman and A. Shamim, "3D printed bifunctional triple-band heatsink antenna for RF and thermal energy harvesting," *Proc. IEEE Int. Symp. Antennas Propag. North Amer. Radio Sci. Meeting*, Montreal, QC, Canada, July 2020.

[81] S. Chamanian, B. Ciftci, H. Ulusan, A. Muhtaroglu and H. Kulah, "Power-efficient hybrid energy harvesting system for harnessing ambient vibrations," *IEEE Trans. Circuits Syst. I Reg. Papers*, vol. 66, no. 7, pp. 2784-2793, July 2019.

[82] X. Gu, L. Guo, S. Hemour and K. Wu, "Optimum temperatures for enhanced power conversion efficiency (PCE) of zero-bias diode-based rectifiers," *IEEE Trans. Microw. Theory Techn.*, vol. 68, no. 9, pp. 4040-4053, September 2020.

[83] B. Clerckx, "Wireless information and power transfer: Nonlinearity waveform design and rate-energy tradeoff," *IEEE Trans. Signal Process.*, vol. 66, no. 4, pp. 847-862, February 2018.

[84] B. Clerckx, R. Zhang, R. Schober, D. W. K. Ng, D. I. Kim, and H. V. Poor, "Fundamentals of wireless information and power transfer: From RF energy harvester models to signal and system designs," *IEEE J. Selec. Areas Commun.*, vol. 37, no. 1, pp. 4–33, January 2019.

[85] O. L. A. Lpez, H. Alves, R. D. Souza, and S. Montejo-Snchez, "Statistical analysis of multiple antenna strategies for wireless energy transfer," *IEEE Trans. Commun.*, vol. 67, no. 10, pp. 7245–7262, October 2019.

[86] A. Collado and A. Georgiadis, "Improving wireless power transmission efficiency using chaotic waveforms," *in Proc. IEEE MTT-S Int. Dig.*, Montreal, QC, Canada, June 2012.

[87] D. I. Kim, J. H. Moon, and J. J. Park, "New SWIPT using PAPR: How it works," *IEEE Wireless Commun. Lett.*, vol. 5, no. 6, pp. 672–675, December 2016.

[88] U. Olgun, C. C. Chen and J. L. Volakis, "Investigation of rectenna array configurations for enhanced RF power harvesting," *IEEE Antennas Wireless Propag. Lett.*, vol. 10, pp. 262-265, April 2011.

[89] C. Psomas, and I. Krikidis, "A wireless powered feedback protocol for opportunistic beamforming using rectenna arrays," *IEEE Trans. Gr. Comm. and Netw.*, vol. 2, no. 1, pp. 100—113, March 2018.

[90] S. Shen, and Bruno Clerckx, "Beamforming optimization for MIMO wireless power transfer with nonlinear energy harvesting: RF combining versus DC combining," *IEEE Trans. Wirel. Commun.*, vol. 20, no. 1, pp. 199-213, January 2021.

[91] D.J. Lee, et al., "Hybrid power combining rectenna array for wide incident angle coverage in RF energy transfer," *IEEE Trans. Microw. Theory Techn.*, vol. 65, no. 9, pp. 3409–3418, September 2017.

[92] J. H. Moon, J. J. Park, K.Y. Lee, and D. I. Kim, "Heterogeneously reconfigurable energy harvester: An algorithm for optimal reconfiguration," *in IEEE Int. of Thin. Jour.*, vol. 8, no. 3, pp. 1437–1452, February 2021.

[93] B. Clerckx, R. Zhang, R. Schober, D. W. K. Ng, D. I. Kim, and H. V. Poor, "Fundamentals of wireless information and power transfer: From RF energy harvester models to signal and system designs," *IEEE J. Sel. Areas Commun.*, vol. 37, no.1, pp. 4-33, January 2019.

[94] A. Costanzo and D. Masotti, "Smart solutions in smart spaces: Getting the most from far-field wireless power transfer," *IEEE Microw. Mag.*, vol. 17, no.5, pp. 30–45, May 2016.

[95] Y. Zeng, B. Clerckx, and R. Zhang, "Communications and signals design for wireless power transmission," *IEEE Trans. Commun.*, vol.65, no.5, pp. 2264-2290, May 2017.

[96] B. Clerckx, A. Costanzo, A. Georgiadis, and N. B. Carvalho, "Towards the 1G of Mobile Power Network: RF, signal and system designs to make smart objects autonomous," *IEEE Microw. Mag.*, vol. 19, no. 6, pp.69-82, October 2018.

[97] N. Shinohara, "Wireless power transfer via radiowaves," *Hoboken*, NJ, USA, Wiley, 2014.

[98] N. B. Carvalho et al., "Wireless power transmission: R&D activities within Europe," *IEEE Trans. Microw. Theory Techn.*, vol. 62, no. 4, pp. 1031–1045, April 2014.

[99] S. Guo, F. Wang, Y. Yang and B. Xiao, "Energy-efficient cooperative for simultaneous wireless information and power transfer in clustered wireless sensor networks," *IEEE Trans. on Comm.*, vol. 63, no.11, pp. 4405-4417, November 2015.

[100] S. Gong, S. Ma, C. Xing, and G. Yang, "Optimal beamforming and time allocation for partially wireless powered sensor networks with downlink SWIPT," *IEEE Trans. on Sign. Proc.*, vol. 67, no. 12, pp. 3197-3212, June 2019.

[101] K. W. Choi, S. Hwang, A. A. Aziz, H. H. Jang, J. S. Kim, D. S. Kang, and D. I. Kim, "Simultaneous wireless information and power transfer (SWIPT) for internet of things: Novel receiver design and experimental validation," *IEEE Int. of Th. Journal*, vol. 7, no. 4, pp. 2996-3012, April 2020.

[102] H. H. Jang, K. W. Choi, and D. I. Kim, "Novel frequency-splitting SWIPT for overcoming amplifier nonlinearity," *IEEE Wir. Comm. Lett.*, vol. 9, no. 6, pp. 826-829, February 2020.

[103] N. Van Huynh, D.T. Hoang, X. Lu, D. Niyato, P. Wang and D.I. Kim, "Ambient backscatter communications: A contemporary survey," *IEEE Commun. Surv. and Tutor.*, vol.20, no. 4, pp. 2889-2922, May 2018.

[104] H. Stockman, "Communication by means of reflected power," *Proc. IRE*, vol. 36, no.10, pp. 1196-1204, October 1948.

[105] H. Ding, J. Han, A. X. Liu, W. Xi, J. Zhao, P. Yang, and Z. Jiang, "Counting human objects using backscatter radio frequency signals," *IEEE Trans. on Mob. Comp.*, vol. 18, no. 5, pp. 1054–1067, May 2019.

[106] E. Moradi, S. Amendola, T. Bjorninen, L. Sydanheimo, J. M. Carmena, J. M. Rabaey, and L. Ukkonen, "Backscattering neural tags for wireless brain-machine interface systems," *IEEE Trans. on Ant. and Prop.*, vol. 63, no.2, pp. 719–726, December 2014.

[107] S. Daskalakis, G. Goussetis, S. D. Assimonis, M. M. Tentzeris, and A. Georgiadis, "A uW backscatter-Morse-leaf sensor for low-power agricultural wireless sensor networks," *IEEE Sensors Journal*, vol. 18, no. 19, pp. 7889–7898, October 2018.

[108] F. Pereira, H. Sampaio, R. Chaves, R. Correia, M. Lus, S. Sargento, M. Jordo, L. Almeida, C. Senna, A. S. R. Oliveira, and N. B. Carvalho, "When backscatter communication meets vehicular networks: boosting crosswalk awareness," *IEEE Access*, vol. 8, pp. 34507–34521, February 2020.

[109] B. Ji, B. Xing, K. Song, C. Li, H. Wen, and L. Yang, "The efficient BackFi transmission design in ambient backscatter communication systems for IoT," *IEEE Access*, vol. 7, pp. 31397-31408, February 2019.

[110] G. Vannucci, A. Bletsas and D. Leigh, "A software-defined radio system for backscatter sensor networks," *IEEE Trans. Wireless Commun.*, vol. 7, no. 6, pp. 2170–2179, June 2008.

[111] A. Bletsas, S. Siachalou and J. N. Sahalos, "Anti-collision tags for backscatter sensor networks," *Proc. 38th Eur. Microw. Conf. (EuMC)*, pp. 179–182, Amsterdam, Netherlands, October 2008.

[112] J. Kimionis, A. Bletsas and J. N. Sahalos, "Bistatic backscatter radio for power-limited sensor networks," *Proc. IEEE Glob. Commun. Conf. (GLOBECOM)*, pp. 353–358, Atlanta, USA, December 2013.

[113] Z. Liu, S. Zhao, Y. Yang, K. Ma, and X. Guan,"Toward hybrid backscatter-aided wireless-powered internet of things networks: Cooperation and coexistence scenarios," *IEEE Int. of Th. Journ.*, vol.9, no. 8, pp.6264-6276, April 2022.

[114] N. Deepan and B. Rebekka,"Backscatter-assisted wireless powered communication networks with multiple antennas," *IEEE Intern. Conf. on Wir. Comm. Sign. Proc. and Netw. (WiSPNET)*, Chennai, India, September 2020.

[115] J. Kim and B. Clerckx, "Range expansion for wireless power transfer using joint beamforming and waveform architecture: An experimental study in indoor environment," *IEEE Wireless Commun. Lett.*, vol. 10, no. 6, pp. 1237-1241, June 2021.

[116] H. Luan, X. Xie, L. Han, C. He, and Z. J. Wang, "A better than Alamouti OSTBC for MIMO backscatter communications," *IEEE Trans. on Wir. Comm.*, vol. 21, no. 2, pp. 1117-1131, February 2022.

[117] M. A. Hossain, R. Md Noor, K. A. Yau, I. Ahmedy and S. S. Anjum, "A survey on simultaneous wireless information and power transfer with cooperative relay and future challenges," *IEEE Access*, vol. 7, pp. 19166-19198, January 2019.

[118] V. Khodamoradi, A. Sali, O. Messadi, A. Khalili, and B. B. M. Ali, "Energy-efficient massive MIMO SWIPT-enabled systems," *IEEE Trans. on Veh. Techn.*, vol. 71, no. 5, pp. 5111-5127, May 2022.

[119] R. Fara, N. Bel-Haj-Maati, D.-T. Phan-Huy, N. Malhouroux, and M. Di Renzo, "First experimental evaluation of ambient backscatter communications with massive MIMO reader," *IEEE 31st An. Intern. Symp. on Pers., Ind. and Mob. Rad. Comm.*, London, UK, 2020.

[120] E. C. van der Meulen, "Three-terminal communication channels," *Adv. Appl. Probab.*, vol. 3, pp. 120-154, 1971.

[121] P. D. Diamantoulakis, "Resource allocation in wireless networks with energy constraints," Ph.D. dissertation, Dept. Elect. and Comp. Eng. Arist. Univ. of Thess. (AUTH), December 2017.

[122] Z. Ding, I. Krikidis, B. Sharif and H. V. Poor, "Wireless information and power transfer in cooperative networks with spatially random relays," *IEEE Trans. Wireless Commun.*, vol. 13, no. 8, pp. 4440-4453, August 2014.

[123] L. Lei, D. Yuan, C. K. Ho and S. Sun, "Power and channel allocation for non-orthogonal multiple access in 5G Systems: Tractability and computation," *IEEE Trans. on Wir. Comm.*, vol. 15, no. 12, pp. 8580- -8594, December 2016.

[124] F. Mukhlif, K. A. B. Noordin, A. M. Mansoor and Z. M. Kasirun, "Green transmission for C-RAN based on SWIPT in 5G: A review," *Wireless Netw.*, vol. 25, pp. 1-29, March 2018.

[125] M. A. Hossain, R. M. Noor, K.-L. A. Yau, I. Ahmedy, and S. S. Anjum, "A survey on simultaneous wireless information and power transfer with cooperative relay and future challenges," *IEEE Access*, vol.7, pp. 19166-19198, January 2019.

[126] Q. Wu, and R. Zhang, "Intelligent reflecting surface enhanced wireless network: Joint active and passive beamforming design," *Proc. IEEE Global Commun. Conf. (GLOBECOM)*, Abu Dhabi, United Arab Emirates, December 2018.

[127] D. Li, "Backscatter communication powered by selective relaying," *IEEE Trans. on Veh. Techn.*, vol.69, no.11, pp.14037-14042, November 2020.

[128] S. Y. Park, and D. I. Kim, "Intelligent reflecting surface-aided phase-shift backscatter communication," *14th Intern. Conf. on Ubiq. Inf. Man. and Comm. (IMCOM)*, Taichung, Taiwan, 2020.

[129] N. Ashraf, S. A. Sheikh, S. A. Khan, I. Shayea, and M. Jalal,"Simultaneous Wireless Information and Power Transfer With Cooperative Relaying for Next-Generation Wireless Networks: A Review," *IEEE Access*, vol.9, pp.71482-71504, May 2021.

[130] Y. Liu, Z. Ding, M. Eikashlan and H. V. Poor,"Cooperative nonorthogonal multiple access in 5G systems with SWIPT," *23rd European Signal Processing Conference (EUSIPCO)*, Nice, France, 2015.

[131] Z. Yang, Z. Ding, P. Fan and N. Al-Dhahir, "The impact of power allocation on cooperative non-orthogonal multiple access networks with SWIPT," *IEEE Trans. Wireless Commun.*, vol. 16, no. 7, pp. 4332-4343, July 2017.

[132] S. K. Zaidi, S. F. Hasan and X. Gui, "SWIPT-aided uplink in hybrid non-orthogonal multiple access," *Proc. IEEE Wireless Commun. Netw. Conf. (WCNC)*, Barcelona, Spain, April 2018.

[133] W. Chen, H. Ding, S. Wang, D. Costa, F. Gong, and P. Nardelli, "Backscatter cooperation in NOMA communications systems," *IEEE Trans. on Wir. Comm.*, vol.20, no. 6, pp.3458-3474, June 2021.

[134] L. Wang, M. Elkashlan, R. W. Heath, M. Di Renzo and K. K. Wong, "Millimeter wave power transfer and information transmission," *IEEE Gl. Comm. Conf. (GLOBECOM)*, San Diego, CA, USA, 2015.

[135] T. A. Khan, A. Alkhateeb and R. W. Heath, "Millimeter wave energy harvesting," *IEEE Transactions on Wireless Communications*, vol. 15, no. 9, pp. 6048-6062, September 2016.

[136] G. Kwon, H. Park, and M. Z. Win, "Joint beamforming and power splitting for wideband millimeter wave SWIPT systems," *IEEE J. of Sel. Top. in Sig. Proc.*, vol. 15, no. 5, pp. 1211-1227, August 2021.

[137] A. Lazaro, M. Lazaro, R. Villarino, and P. de Paco,"Car-to-car communication based on modulated active backscatter and automotive radar," *51st Europ. Micr. Conf. (EuMC)*, London, UK, 2022.

[138] L. Jiang, C. Qin, X. Zhang and H. Tian, "Secure beamforming design for SWIPT in cooperative D2D communications," *China Communications*, vol. 14, no. 1, pp. 20-33, January 2017.

[139] F. Yuan, S. Jin, K. K. Wong, Q. T. Zhang and H. Zhu, "Optimal harvest-use-store design for delay-constrained energy harvesting wireless communications," *J. of Comm. and Net.*, vol. 18, no. 6, pp. 902-912, December 2016.

[140] J. Huang; C.-C. Xing, and M. Guizani, "Power allocation for D2D communications with SWIPT," *IEEE Trans. on Wir. Comm.*, vol. 19, pp. 2308–2320, Apr. 2020.

[141] X. Lu, H. Jiang, D. Niyato, D. I. Kim, and Z. Han,"Wireless-powered device-to-device communications with ambient backscattering: Performance modeling and analysis," *IEEE Trans. on Wir. Comm.*, vol.17, no. 3, pp.1528-1544, March 2018.

[142] D Niyato, "Editorial: Third Quarter 2022," *IEEE Comm. Surv. and Tut.*, vol. 24, no. 3, pp. i-v, August 2022.

[143] T. Song and P. Kam, "Efficient direct detection of M-PAM sequences with implicit CSI acquisition for the FSO system," *in Proc. IEEE Global Commun. Conf. Workshops*, Austin, TX, December 2014.

[144] D. Papailiopoulos, G. A. Elkheir, and G. N. Karystinos, "Maximum- likelihood noncoherent PAM detection," *IEEE Trans. Commun.*, vol.61, no. 3, pp. 1152-1159, March 2013.

[145] J. G. Proakis and M. Salehi, *Digital Communications*, McGraw-Hill, 5th ed., 1995.

[146] *Matlab and Optimization Toolbox User Guide*, Release 2013, The MathWorks, Inc., Natick, Massachusetts, United States.

[147] C.-H. Chang, R. Y. Chang, and F.-T. Chien, "Energy-assisted information detection for SWIPT: Performance analysis and case studies," *IEEE Trans. Signal Inf. Process. Net.*, vol. 2, no. 2, pp. 149-159, June 2016.

[148] L. Liu, R. Zhang, and K. Chua, "Wireless information and power transfer: A dynamic power splitting approach," *IEEE Trans. Commun.*, vol. 61, no. 9, pp. 3990-4001, September 2013.

[149] K. W. Choi, L. Ginting, A. A. Aziz, D. Setiawan, J. H. Park, S. I. Hwang, D. S. Kang, M.Y. Chung, and D. I. Kim, "Toward realization of long-range wireless-powered sensor networks," *IEEE Wireless Commun.*, vol. 26, no. 4, pp. 184–192, August 2019.

[150] K. W. Choi, S. I. Hwang, A. A. Aziz, H. H. Jang, J. S. Kim, D. S. Kang, and D. I. Kim, "Simultaneous wireless information and power transfer (SWIPT) for internet of things: Novel receiver design and experimental validation," *Inter. of Thing. Journ.*, vol. 7, no.4, pp. 2996-3012, April 2020.

[151] M. Rajabi, N. Pan, S. Claessens, S. Pollin, and D. Schreurs, "Modulation techniques for simultaneous wireless information and power transfer with an integrated rectifier-receiver," *IEEE Trans. Micr. Theor. Techn.*, vol. 66, no. 5, pp. 2373–2385, May 2018.

[152] J. Krikidis and C. Psomas, "Tone-index multisine modulation for SWIPT," *IEEE Sign. Proc. Let.*, vol. 26, no. 8, pp. 1252–1256, August 2019.

[153] S. Claessens, N. Pan, M. Rajabi, D. Schreurs, and S. Pollin,"Enhanced biased ask modulation performance for SWIPT with awgn channel and dual-purpose hardware," *IEEE Trans. on Micr. Theor. and Techn.*, vol. 66, no. 7, pp. 3478–3486, July 2018.

[154] L. Zheng, and D.N.C. Tse, "Diversity and multiplexing: a fundamental tradeoff in multiple-antenna channels," *IEEE Trans. Inf. Theory*, vol. 49, no. 5, pp. 1073-1096, 2003.

[155] I. E. Telatar, "On the capacity of multi-antenna Gaussian channels," *IEEE Cat. No.01CH37252*, June, Washington, DC, USA.

[156] G. Foschini, G. Golden, R. Valenzuela, and P. Wolniansky, "Simplified processing for high spectral efficiency wireless communication employing multi-element arrays," *IEEE J. Select. Areas Commun.*, vol. 17, no. 11, pp. 1841-1852, November 1999.

[157] A. Georgiadis, G. V. Andia, and A. Collado, "Rectenna design and optimization using reciprocity theory and harmonic balance analysis for electromagnetic energy harvesting," *IEEE Ant. and Wirel. Prop. Lett.*, vol. 9, pp. 444-446, May 2010.

[158] H. Sun, Y. Guo, M. He, and Z. Zhong,"Design of a high-efficiency 2.45- GHz rectenna for low-input-power energy harvesting," *IEEE Ant. and Wirel. Prop. Lett.*, vol. 11, pp. 929–932, August 2012.

[159] C. R. Valenta and G. D. Durgin, "Harvesting wireless power: Survey of energy-harvester conversion efficiency in far-field, wireless power transfer systems," *IEEE Micr. Mag.*, vol. 15, no. 4, pp. 108–120, June 2014.

[160] P. N. Alevizos, and A. Bletsas, "Sensitive and nonlinear far-field RF energy harvesting in wireless communications," *IEEE Trans. Wireless Commun.*, vol. 17, no. 6, pp. 3670-3685, June 2018.

[161] L. Jing, E. De Carvalho, P. Popovski, and A. O. Martinez, "Design and performance analysis of noncoherent detection systems with massive receiver arrays," *IEEE Trans. Sign. Process.*, vol. 64, no. 19, pp. 5000-5010, October 2016.

[162] P. Liu, S. Gazor, Il-M. Kim, and D.I. Kim, "Noncoherent relaying in energy harvesting communication systems," *IEEE Trans. Commun.*, vol. 14, no. 12, pp. 6940-6954, July 2015.

[163] D. C. Daly, and A. P. Chandrakasan, "An energy-efficient OOK transceiver for wireless sensor networks," in *IEEE Journ. of Solid-State Circ.*, vol. 42, no. 5, pp. 1003-1011, May 2007.

[164] J. Tao, N. Wang, E. Jiaqiang Ng, Y. Zhu, and C.-H. Heng, "A 5-pJ/Bit OOK transmitter using MEMS-Based RF oscillator for IoT application in 180-nm CMOS," *IEEE Micr. and Wir. Compon. Let.*, vol. 31, no. 10, pp. 1158-1161, October 2021.

[165] M. Molefi, E. D. Markus, and A. Abu-Mahfouz, "Wireless power transfer for IoT devices - A review", *IEEE Int. Mult. Inf. Techn. and Eng. Conf. (IMITEC)*, Vanderbijlpark, S. Africa 2019.

[166] A. Costanzo, D. Masotti, G. Paolini, and D. Schreurs, "Evolution of SWIPT for the IoT World: Near- and far-field solutions for simultaneous wireless information and power transfer," *IEEE Micr. Mag.*, vol. 22, no. 12, pp. 48-59, December 2021.

[167] S. Shen, and B. Clerckx, "Joint waveform and beamforming optimization for MIMO wireless power transfer," *IEEE Trans. Commun.*, vol. 69, no. 8, pp. 5441-5455, August 2021.

[168] E. Kwiatkowski, C. T. Rodenbeck, T. Barton, and Z. Popovic, "Power-combined rectenna array for X-band wireless power transfer," *IEEE MTT-S Intern. Micr. Symp. (IMS)*, L.A. USA, 2020.

[169] J. H. Moon, J. J. Park, K.Y. Lee, and D. I. Kim, "Heterogeneously reconfigurable energy harvester: An algorithm for optimal reconfiguration," in *IEEE Int. of Thin. Jour.*, vol. 8, no. 3, pp. 1437-1452, February 2021.

[170] W. Feller, *Introduction to probability theory and its applications*, Wiley, 3rd ed., 1968.

[171] X. Xu, A. Özçelikkale, T. McKelvey and M. Viberg, "Simultaneous information and power transfer under a non-linear RF energy harvesting model," *IEEE Intern. Conf. Comm. Work.*, Paris, France, May 2017.

[172] S. Bashir, S. Ali, S. Ahmed, and V. Kakkar, "Analog-to-digital converters: A comparative study and performance analysis," *Intern. Conf. on Comp., Commun. and Autom. (ICCCA)*, Greater Noida, India, January 2017.

[173] K. Han and K. Huang, "Wirelessly powered backscatter communication networks: Modeling, coverage, and capacity," *IEEE Trans. Wireless Commun.*, vol. 16, no. 4, pp. 2548 - 2561, April 2017.

[174] M. Palattella, M. Dohler, A. Grieco, G. Rizzo, J. Torsner, T. Engel and L. Ladid, "Internet of things in the 5G era: Enablers, architecture and business models," *IEEE J. Selected Areas Commun.* , Vol. 34, no. 3, pp. 510–27, Mar. 2016.

[175] S. Thomas, and M. Reynolds, "A 96 mbit/sec, 15.5 pj/bit 16-qam modulator for UHF backscatter communication," *IEEE Int. Conf. RFID*, pp. 185-190, Orlando, USA, 2012.

[176] C. Boyer, and S. Roy, "Communication and RFID: Coding, energy, and MIMO analysis," *IEEE Trans. Commun.*, vol. 62, no. 3, pp. 770-785, December 2013.

[177] G. Wang, F. Gao, R. Fan and C. Tellambura, "Ambient backscatter communication systems: Detection and performance Analysis," *IEEE Trans. Commun.*, vol. 64, no.11, pp. 4836-4846, November 2016.

[178] P. Alevizos, A. Bletsas, and G. N. Karystinos, "Noncoherent short packet detection and decoding for scatter radio sensor networking," *IEEE Trans. Commun.*, vol. 65, no.5, pp. 2128–2140, May 2017.

[179] J. Qian, F. Gao, G. Wang, S. Jin, and H. Zhu, "Noncoherent detections for ambient backscatter system," *IEEE Trans. Wireless Commun.*, vol. 16, no. 3, pp. 1412-1422, March 2017.

[180] A. Younis, N. Serafimovski, R. Meslehand, H.Haas, "Generalised spatial modulation," *in Conf. Rec. Asilomar Conf. Signals, Syst., Comput.*, Pacific Grove, CA, November 2010.

[181] J. Jeganathan, A. Ghrayeb and L. Szczecinski, "Spatial modulation: Optimal detection and performance analysis," *IEEE Commun. Letters*, vol. 12, no. 8, August 2008.

[182] R. Mesleh, H. Haas, S. Sinanovic, C. W. Ahn and S. Yun, "Spatial modulation," *IEEE Trans. Veh. Technol.*, vol. 57, no. 4, pp. 2228-2241, July 2008.

[183] E. Basar, U. Aygolu, E. Panayirci and H. V. Poor, "Space-time block coded spatial modulation," *IEEE Trans. Commun.*, vol. 59, no. 3, pp. 823-832, March 2011.

[184] S. Alamouti, "A simple transmit diversity technique for wireless communications," *IEEE J. Sel. Areas Commun.*, vol. 16, no.8, pp. 1451-1458, October 1998.

[185] Z. Niu, W. Wang and T. Jiang, "Spatial modulation for ambient backscatter communications: modeling and analysis," *IEEE Glob. Commun. Conf. (GLOBECOM)*, Waikoloa, HI, USA, December 2019.

[186] Z. Ma, F. Gao, J. Jiang and Y.Liang, "Cooperative detection for ambient backscatter assisted generalized spatial modulation," *IEEE Glob. Commun. Conf. (GLOBECOM)*, Waikoloa, HI, USA, December 2019.

[187] Y. Zhang, F. Gao, L. Fan, X. Lei, and G. K. Karagiannidis, "Secure communications for multi-tag backscatter systems," *IEEE Wirel. Comm. Lett.*, vol.8, no. 4, pp.1146-1149, August 2019.

[188] B. Zhu, J. Cheng, M. Alouini, and L. Wu, "Relay placement for FSO multihop DF systems with link obstacles and infeasible regions," *IEEE Trans. on Wirel. Comm.*, vol.14, no. 9, pp.5240-5250, September 2015.

[189] M. Alkhawatrah, Y. Gong, G. Chen, S. Lambotharan, and J. A. Chambers, "Buffer-aided relay selection for cooperative NOMA in the internet of things," *IEEE Intern. of Thin. Journ.*, vol.6, no. 3, pp.5722-5731, June 2019.

[190] Q. Li, M. Wen, M. D. Renzo, H. V. Poor, S. Mumtaz, and F. Chen, "Dual-Hop spatial modulation with a relay transmitting its own information," *IEEE Trans. on Wirel. Commun. (Early Access)*, vol. 19, no. 7, pp. 4449-4463, July 2020.

[191] N. Fasarakis-Hilliard, P. N. Alevizos and A. Bletsas "Coherent Detection and Channel Coding for Bistatic Scatter Radio Sensor Networking," *IEEE Trans. Commun.*, vol. 63, no. 5, pp. 1798-1810, May 2015.

[192] D.Tse and P. Viswanath, *Fundamentals of Wireless Communications*, Cambridge University press, August 2004.

[193] F. Fuschini, C. Piersanti, F. Paolazzi, and G. Falciasecca, "Analytical approach to the backscattering from UHF RFID transponder," *IEEE Antenna Wireless Propag. Lett.*, vol. 7, pp. 33–35, February 2008.

[194] X. Guo and X.G. Xia, "On full diversity space-time block codes with partial interference cancellation group decoding," *IEEE Trans. Inf. Theory*, vol. 55, no. 10, pp. 4366-4385, October 2009.

[195] E. Goudeli, C. Psomas, I. Krikidis, H. Kiani, D. Chatzichristodoulou, and S. Nikolaou, "Detection schemes for integrated SWIPT receivers with non-linear energy harvesting," *IEEE Veh. Tech. Conf.*, Helsinki, Finland, 2022.

[196] B. Clerckx, J. Kim, K. W. Choi, and D. Kim,"Foundations of wireless information and power transfer: Theory, prototypes, and experiments," *Proc.of the IEEE*, vol. 110, no. 1, pp. 8-30, January 2022.

[197] J. Kim and B. Clerckx, "Wireless information and power transfer for IoT: Pulse position modulation, integrated receiver, and experimental validation," in *IEEE Int. of Th. J.*, vol. 9, no. 14, pp. 12378-12394, July 2022.

[198] M. Wozniak, A. Zielonka, A. Sikora, M. J. Piran, and A. Alamri, "6g-enabled IoT home environment control using fuzzy rules," *IEEE Int. of Thing. J.*, vol.8, no. 7, pp.5442-5452, April 2021.

[199] R. C. Loli, O. Dizdar, B. Clerckx, and C. Ling, "Model-based deep learning receiver design for rate-splitting multiple access," in *arXiv:2205.00849*, May 2022.

[200] Y. Xing, R. Young, G. Nguyen, M. Lefebvre, T. Zhao, and H. Pan, "Optimize mobile wireless power transfer by finite state machine reinforcement learning," in *IEEE 12th Ann. Comp. and Comm. Work. and Conf. (CCWC)*, Las Vegas, USA, January 2022.

[201] B. Clerckx, K. Huang, L. R. Varshney, S. Ulukus, and M.-S. Alouini, "Wireless power transfer for future networks: Signal processing, machine learning, computing, and sensing," in *IEEE J. of Sel. Top. in Sign. Proc.*, vol. 15, no. 5, pp. 1060-1094, August 2021.

[202] Q. Wu and R. Zhang, "Towards smart and reconfigurable environment: Intelligent reflecting surface aided wireless network," *IEEE Comm. Mag.*, vol. 58, no. 1, pp. 106-112, January 2020.

[203] L. Dai et al., "Reconfigurable intelligent surface-based wireless communications: Antenna design, prototyping, and experimental results," *IEEE Acc.*, vol. 8, pp. 45913-45923, March 2020.

[204] Y. Zhao, B. Clerckx, and Z. Feng, "IRS-Aided SWIPT: Joint waveform, active and passive beamforming design under nonlinear harvester model," *IEEE Trans. on Comm.*, vol. 70, no. 2, pp. 1345-1359, February 2022.

[205] S. Basharat, S. A. Hassan, A. Mahmood, Z. Ding, and M. Gidlund, "Reconfigurable Intelligent surface-assisted backscatter communication: A new frontier for enabling 6G IoT networks," *IEEE Wirel. Comm.*, pp. 1—8, June 2022.

[206] R. Zhang and C. K. Ho, "MIMO broadcasting for simultaneous wireless information and power transfer," *IEEE Trans. Wireless Commun.*, vol. 12, no. 5, pp. 1989-2001, May 2013.

[207] L. Liu, R. Zhang, and K. Chua, "Wireless Information Transfer with opportunistic energy harvesting," *IEEE Trans. Wireless Commun.*, vol. 12, no.1, pp. 288-300, January 2013.

[208] R. Morsi, D. S. Michalopoulos, and R. Schober, "Multiuser scheduling schemes for simultaneous wireless information and power transfer over fading channels," *IEEE Trans. Wireless Commun.*, vol. 14, no. 4, pp. 1967-1982, April 2015.

[209] I. Krikidis, S. Sasaki, S. Timotheou, and Z. Ding, "A low complexity antenna switching for joint wireless information and energy transfer in MIMO relay channels," *IEEE Trans. Commun.*, vol. 62, no. 5, pp. 1577-1587, May 2014.

[210] I. Krikidis, "Opportunistic beamforming with wireless powered 1-bit feedback through rectenna array," *IEEE Signal Process. Lett.*, vol. 22, no. 11, pp. 2054-2058, November 2015.

[211] M. Steer, *Microwave and RF Design.*, SciTech Publishing, 2010.

[212] E. Boshkovska, D. W. K. Ng, N. Zlatanov, and R. Schober, "Practical non-linear energy harvesting model and resource allocation for SWIPT systems," *IEEE Commun. Lett.*, vol. 19, no. 12, pp. 2082-2085, Dec. 2015.

[213] E. Boshkovska, N. Zlatanov, L. Dai, D. W. K. Ng, and R. Schober, "Secure SWIPT networks based on a non-linear energy harvesting model," *Proc. IEEE Wir. Commun. and Netw. Conf. (WCNC)*, San Francisco, CA, 2017.

[214] E. Boshkovska, X. Chen, L. Dai, D. W. K. Ng, and R. Schober, "Max-min fair beamforming for SWIPT systems with non-linear EH model," *IEEE 86th Veh. Techn. Conf. (VTC-Fall)*, Toronto, Canada, September 2017.

[215] E. Boshkovska, D. W. K. Ng, L. Dai, and R. Schober, "Power-efficient and secure WPCNs with hardware impairments and non-linear EH circuit," *IEEE Trans. on Comm.*, vol.66, no. 6, pp. 2642-2657, June 2018.

[216] E. Boshkovska, D. W. K. Ng, N. Zlatanov, A. Koelpin, and R. Schober, "Robust resource allocation for MIMO wireless powered communication networks based on a non-linear EH model," *IEEE Trans. Commun.*, vol. 65, no. 5, pp. 1984-1999, May 2017.

[217] S. Wang, M. Xia, K. Huang, and Y. C. Wu, "Wirelessly powered two-way communication with nonlinear energy harvesting model: Rate regions under fixed and mobile relay," *IEEE Trans. Wireless Commun.*, vol. 16, no. 12, pp. 8190-8204, December 2017.

[218] X. Xu, A. Ozc, Elikkale, T. McKelvey, and M. Viberg, "Simultaneous information and power transfer under a non-linear RF energy harvesting model," *Proc. IEEE Int. Conf. on Commun. (ICC)*, pp. 179-184, Paris, France, 2017.

[219] Y. Chen, K.S. Thomas, R.A.A. Abd, "New formula for conversion efficiency of RF EH and its wireless applications," *IEEE Trans. on Veh. Technol.*, vol. 65, no. 11, pp. 9410-9414, November 2016.

[220] Y. Chen, N. Zhao and M. Alouini, "Wireless energy harvesting using signals from multiple fading channels," *IEEE Trans. Commun.*, vol. 65, no. 11, pp. 5027-5039, November 2017.

[221] P. N. Alevizos, G. Vougioukas, and A. Bletsas, "Nonlinear energy harvesting models in wireless information and power transfer," *arXiv:1802.09994*, February 2018.

[222] Wireless Telecom Group Inc., "Principles of Power Measurement: a Primer of RF and Microwave Power Measurement," Tech. Rep., 2011.

[223] Eli Grushka, "Characterization of exponentially modified Gaussian peaks in chromatography," *Anal. Chem.*, vol. 44, pp. 1733–1738, Sep. 1972.

[224] Agilent Technologies, Inc., *Surface Mount Zero Bias Schottky Detector Diodes*, March 2004.

[225] S. Nikoletseas, Y. Yang, and A. Georgiadis, Eds., "Wireless power transfer algorithms, technologies and applications in ad hoc communication networks," *Springer International Publishing*, 2016.

[226] O C. Ibe, *Markov processes for stochastic modeling*, Elsevier, 2nd ed., 2013.

[227] J. R. Hampton, *Introduction to MIMO Communications*, Cambridge University Press, 2014.

[228] M. Chiani, D. Dardari, M. K. Simon, "New exponential bounds and approximations for the computation of error probability in fading channels," *IEEE Trans. Wireless Commun.*, vol. 2, no. 4, pp. 840-845, July. 2003.

[229] M. Abramowitz, IA Stegun, *Handbook of Mathematical Functions*, National Bureau of Standards, Washington, DC, 1972.